2-1-2012

Oblique shock interactions With perturbed density interfaces

Michael J. Anderson

Michael J. Anderson

Candidate

Mechanical Engineering

Department

This dissertation is approved, and it is acceptable in quality and form for publication:

Approved by the Dissertation Committee:

Peter Vorobieff , Chairperson

Charles Randall Truman

Andrea Mammoli

Charles E. Needham

Pavel M. Lushnikov

Oblique Shock Interactions With Perturbed Density Interfaces

by

Michael J. Anderson

B.S., Aeronautical and Astronautical Engineering,
University of Illinois, 2003
M.S., Aerospace and Mechanical Engineering,
University of Southern California, 2006

DISSERTATION

Submitted in Partial Fulfillment of the

Requirements for the Degree of

Doctor of Philosophy
Engineering

The University of New Mexico

Albuquerque, New Mexico

October, 2011

Dedication

For Lynn, without whom none of this would have been possible.

Acknowledgments

I would like to thank, first and foremost, my advisor, Dr. Peter Vorobieff. He has spent the better part of the last two years bestowing a small part of his knowledge and experience as an experimentalist upon me and for that I am forever grateful. Secondly, I would like to thank Charlie Needham and my co-workers in the Computational Physics Group (CPG) at Applied Research Associates (ARA), Inc. I have spent the last five years working with them and their knowledge of SHAMRC and computational physics has proven extremely useful in that time. I count myself lucky to have been able to approach these problems from an experimental and numerical point of view. Without these people none of this would have been possible.

I would also like to thank my fellow graduate students, Joseph Conroy, Ross White, and Patrick Wayne as well as Dr. Sanjay Kumar and Dr. Randy Truman. Their help in acquiring and analyzing test data as well as their dedication and countless hours of work in the shock tube facility was much appreciated.

Finally, this work was funded by US National Nuclear Security Agency (NNSA) under the Stewardship Science Academic Alliances program through DOE Grant DE-PS52-08NA28920 and by the US Defense Threat Reduction Agency (DTRA) under awards HDTRA1-07-1-0036 and HDTRA1-08-1-0053. Without this funding, none of this work could have been performed.

Oblique Shock Interactions With Perturbed Density Interfaces

by

Michael J. Anderson

B.S., Aeronautical and Astronautical Engineering,

University of Illinois, 2003

M.S., Aerospace and Mechanical Engineering,
University of Southern California, 2006

Ph.D., Engineering, University of New Mexico, 2011

Abstract

This dissertation presents an experimental and numerical consideration of fluid instabilities formed by the interaction of a planar shock wave and a cylindrical column of gas seeded with glycol droplets. Seeding a fluid flow with a passive tracer is a common practice in experimental fluids research and it is important to understand how these tracers behave. It will be shown that these tracers do not explicitly follow the flow, and in extreme cases can cause hydrodynamic instabilities.

Experiments were performed in the University of New Mexico (UNM) tiltable shock tube facility and numerical analysis was performed using the Eulerian hydrodynamics code SHAMRC (Second-order Hydrodynamic Automatic Mesh Refinement Code). Two gases are considered. The first gas is sulfur hexafluoride (SF_6), which generates the well known Richtmyer-Meshkov Instability (RMI) when accelerated by

a shock wave. This instability is formed due to a mis-alignment of the pressure and density gradients during impulsive acceleration. The second gas is air. There is no density gradient between the gas column and the surrounding air, but an instability is formed that is similar in morphology to RMI due to the presence of the glycol droplets. Experimental and numerical results are presented for both types of instability at Mach numbers 1.2, 1.67, and 2.0. Also, numerical parameter studies that vary the Atwood number, Mach number, and the droplet diameter are discussed.

The cylindrical gas column represents a three-dimensional set of initial conditions which are often considered two-dimensional due to geometry. The validity of this assumption is explored experimentally and numerically for both types of initial conditions by looking at images taken (or produced) in both horizontal and vertical planes of the instability. The results show that this assumption is valid, with variations in the instabilities morphology occurring only near the walls of the shock tube. Finally, a fully 3D scenario is considered by introducing an angle of incidence between the planar shock wave and the cylindrical column.

Contents

List of Figures

List of Tables

Chapter 1

Introduction

A Richtmyer-Meshkov Instability (RMI) is generated when an interface between two fluids of differing density is impulsively accelerated. This instability was first theoretically described by Richtmyer [2] and later demonstrated experimentally by Meshkov [3]. The instability develops due to a misalignment of the density and pressure gradients which results in the deposition of vorticity, causing the formation of a perturbation that grows non-linearly with time and eventually may transition to fully turbulent flow. RMI occurs in various natural and engineering phenomena, including: supernovae explosions, deflagration to detonation transition, inertial confinement fusion, and plays an important role in mixing during combustion.

In traditional RMI, vorticity is generated due to the misalignment of pressure and density gradients in a continuous fluid phase. However, it has recently been shown experimentally [1] and numerically [4] that a similar class of instability can evolve in multi-phase flows, where the average density gradient is caused by a second, non-fluid phase. In this scenario, initial conditions consisting of a region of flow seeded with particles or droplets having a non-trivial mass are impulsively accelerated by a shock wave, causing the formation of an instability that resembles RMI. Fundamentally,

this region can be thought of as a fluid with a density equal to the mass of the secondary phase divided by the volume that it occupies, effectively spreading the mass of the secondary phase out over the entire region encompassed by the initial conditions. In this respect, it is easy to see how an instability similar in morphology to RMI might occur. The major difference in the case of the multi-phase equivalent is the absence of a true density interface between the initial conditions and the shock wave and thus the absence of the primary mechanism for RMI formation, i.e. vorticity deposition due to a misalignment of the pressure and density gradients.

1.1 The Richtmyer-Meshkov Instability

The vorticity of a velocity field is defined as the curl of that field, or $\vec{\omega} = \vec{\nabla} \times \vec{v}$. The vorticity is a vector with a magnitude that is related to the rotational motion of a fluid element and a direction perpendicular to that motion. The equation for vorticity production is derived by taking the curl of the Navier-Stokes equation, shown in Equation 1.1. Here, $\frac{D()}{Dt}$ is the material derivative, as defined in Equation 1.2. The variable $\vec{v}$ is the velocity, $\vec{g}$ represents the body forces (in this case gravity), P is the pressure, and μ is the dynamic viscosity. The resulting vorticity equation is shown in Equation 1.3 for an inviscid fluid with zero body forces.

$$\rho \frac{D\vec{v}}{Dt} = \rho\vec{g} - \vec{\nabla}P + \mu\vec{\nabla^2}\vec{v} \tag{1.1}$$

$$\frac{D}{Dt} = \left(\frac{\partial}{\partial t} + \vec{v} \cdot \vec{\nabla}\right) \tag{1.2}$$

$$\frac{D\vec{\omega}}{Dt} = \left(\vec{\omega} \cdot \vec{\nabla}\right)\vec{v} - \vec{\omega}\left(\vec{\nabla} \cdot \vec{v}\right) + \frac{\vec{\nabla}\rho \times \vec{\nabla}P}{\rho^2} \tag{1.3}$$

In Equation 1.3 the first term represents the generation of vorticity due to a velocity gradient or vortex stretching. The second term represents vorticity generation due to compressibility. For a flow at rest, there is no initial vorticity and thus both of these terms are zero. The third term is the baroclinic vorticity term. This term represents the generation of vorticity due to misalignment of the pressure and density gradients and is the primary mechanism for vorticity generation in RMI.

Figure 1.1 shows how a passing shock wave generates a Richtmyer-Meshkov instability for three initial perturbation geometries. In each geometry the interface is defined as the region separating two gases with differing densities, with the lower density gas being referred to as 'light' and the higher density gas being referred to as 'heavy'. The first geometry (top) is a planar interface between light and heavy gases with a protrusion of heavy gas into the light gas. The shock wave travels from the light gas into the heavy gas. As the shock passes the perturbation, vorticity is deposited in the form of a clockwise rotation on the upper surface and a counter-clockwise rotation at the lower surface. This interaction causes the perturbation amplitude to grow immediately. The second geometry (center) depicts a planar boundary between the light and heavy gases. In this case, the shock passes from the heavy gas to the light and the perturbation is formed by a protrusion of light gas into the heavy gas. In this geometry, the density gradient is reversed resulting in a deposition of vorticity which is opposite in sign and causes the direction of rotation to be reversed when compared with the first geometry. The amplitude of the perturbation initially decreases up until phase inversion, after which, the amplitude increases. The third and final geometry (bottom) is a cylinder of heavy gas embedded in light gas. This is a combination of the first and second geometries. As the shock enters the upstream side of the cylinder, vorticity is deposited in the same manner as the first geometry, causing immediate growth of the perturbation amplitude. Once the shock passes through the middle of the cylinder, it is passing from a heavy fluid to a light fluid, reversing the sign of vorticity deposited, as is

geometry two. This vorticity deposition results in the roll-up of the cylinder edges to form two counter-rotating vortex pairs. This final case represents the instability morphology that will be focused on in this work.

1.2 Motivation

The initial driving force behind research on RMI was nuclear weapons research in the 1960s. RMI plays an integral role during the early stages of nuclear detonation and must be accurately modeled by Computational Fluid Dynamics (CFD) codes used for nuclear stockpile stewardship. Interest in RMI was renewed with the emergence of Inertial Confinement Fusion (ICF) as a potential power source in the 1970s [6]. In ICF a pellet of fuel consisting of a core of deuterium and tritium gas surrounded by a dense ablative shell is rapidly heated [7]. This heating results in a shock wave which compresses the fuel and initiates the fusion reaction. The generation of RMI during this processresults in a non-uniform compression and can degrade the performance of the ICF fuel pellet. RMI is induced by the inward moving shock and can cause mixing of the outer shell and inner fusion gases, reducing the overall compression and temperature increase by the converging shock wave.

Another area where RMI plays a role is in the formation of supernova remnants. When a star nears the end of its life it may form a supernova if the mass of the star is large enough. A supernova is a strong shock wave, which propagates outward from the core of the star [8]. The shock wave expels most of the mass of the star and passes into the surrounding interstellar medium, creating what is known as a supernova remnant. Finger-like protrusions that form in the remnant are believed to be caused by hydrodynamic instabilities [9], mainly Rayleigh-Taylor. However, the effects of mixing caused by RMI on the expansion has been explored [10] and is now an integral part of the modeling of supernova remnant formation and evolution [11].

Finally, Richtmyer-Meshkov instabilities can also play an important role in combustion processes. Combustion can occur either subsonically (deflagration) or supersonically (detonation) [12]. In deflagration the flame front heats the surrounding fuel and advances at a velocity less than the speed of sound. In detonation a shock wave moves through the fuel, rapidly heating it and driving the combustion reactions. A deflagration wave can transition to detonation in an extremely complex process known as Deflagration-to-Detonation Transition (DDT) [13]. The mechanism by which DDT occurs is not clear in experiments, however, numerical simulations have indicated that shock waves interacting with the flame front can cause RMI to develop. The instability induces mixing of unburned materials into the burned region and can cause DDT. In a SCRAMJET (Supersonic Combustion ramjet), the residence time of fuel and oxidizer in the combustion chamber is on the order of milliseconds [14]. If the mixing of the fuel (heavy gas or droplets) and oxidizer (light gas) is not complete, combustion can be locally quenched and cause a reduction is engine efficiency. One method of mixing the reactants is through interactions with shock waves, or shock-induced mixing. The interaction of shock waves with density interfaces between the light and heavy gases or droplets will result in the formation of RMI, enhancing the mixing and promoting combustion.

There is no shortage of reasons to study Richtmyer-Meshkov instabilities, either from the point of view of limiting the instabilities impact on ICF, or utilizing the instability to promote mixing. Developing robust computational models that can accurately reproduce the instability is important to understanding these phenomena. The primary goal of this work is to explore the formation and growth of single and multi-phase RMI through experimental and numerical methods. These types of instabilities can be created in a controlled laboratory setting, which allows for the generation of repeatable experimental results. These results can be used to validate numerical models at specific points in a wide ranging parameter space, which includes, but is not limited to, variables such as the shape and composition of the

initial conditions and the shock Mach number. By using these controlled experiments as a baseline, powerful numerical models can be validated. In turn, these results increase the confidence in simulations of the complicated physical processes listed above, many of which can not be easily recreated in a laboratory setting and can only be considered numerically.

1.3 Previous Research

The Richtmyer-Meshkov instability is named for the men credited with its discovery, Robert D. Richtmyer and Evgeny E. Meshkov. Richtmyer first postulated the existence of the instability in his 1960 paper [2] where he performed a theoretical and numerical analysis. His theoretical treatment of the instability was two-fold. The first, the impulsive model, was based on the work of G. I. Taylor on the growth of instabilities at the interface of two fluids of differing density subject to an acceleration, otherwise know as the Rayleigh-Taylor Instability (RTI). Richtmyer considered an impulsive acceleration $\Delta u \delta(t)$ and showed that the growth of the amplitude η of small perturbations is given by Equation 1.4, where Δu is the velocity change across the shock front and η_0 is the initial perturbation amplitude. This is opposed to the solution found by Taylor for constant acceleration given by Equation 1.5. In these equations, k is the wavenumber, $k = \frac{2\pi}{\lambda}$ with λ being the perturbation wavelength and A is the Atwood number, given by $A = \frac{\rho_2 - \rho_1}{\rho_2 + \rho_1}$.

$$\frac{d\eta(t)}{dt} = k\Delta u A \eta_0 \tag{1.4}$$

$$\frac{d^2\eta(t)}{dt^2} = kgA\eta(t) \tag{1.5}$$

The second treatment by Richtmyer was a linear model based on the Euler equations for a shock moving from a light to a heavy fluid. He used a finite difference method to calculate perturbation growth rates based on this model. In 1969 Meshkov proved the existence of the instability through his shock tube work [3]. He performed experiments for a shock transiting from a light to a heavy fluid and from a heavy to a light fluid and found that both scenarios were unstable. This is a primary difference from the Rayleigh-Taylor instability, which is only unstable for a light fluid accelerating a heavy fluid. Since the time of Richtmyer and Meshkov there has been a great deal of research devoted to furthering the understanding of RMI. The focus here is limited to work relevant to this dissertation, namely shock accelerated heavy gas cylinders.

In 1960, Rudinger and Somers experimentally and theoretically studied the behavior of spherical and cylindrical gas bubbles accelerated by shock waves [15]. Their goal was to characterize the movement of bubbles used as passive tracers relative to the flow. They created bubbles of hydrogen, helium, and sulfur-hexafluoride (SF_6) and measured the bubble displacement with a schlieren system. Experiments were performed at Mach numbers 1.12, 1.22, and 1.28. The bubble displacements were compared to the displacement of a spark, which represents the displacement of the air behind the shock. They found that the bubble displacement was larger than the surrounding air for gases lighter than air, while the bubble displacement was smaller than the surrounding air for gases heavier than air. They also derived an expression relating the bubble velocity to the gas velocity by considering the formation of a vortex ring in the case of a spherical bubble or a vortex pair in the case of a cylinder. The result is shown in Equation 1.6, where u_b is the bubble velocity, u_g is the gas velocity, and σ is the ratio between the air and gas densities, specifically $\sigma = \frac{\rho_b}{\rho_g}$. It is noted that this expression can be rewritten in terms of the Atwood number, given by $A = \frac{\rho_b - \rho_g}{\rho_b + \rho_g}$, which is shown as Equation 1.7. A comparison between their theory and experimental measurements yielded good agreement.

$$\frac{u_b}{u_g} = 1 + \frac{2}{\pi^2}\frac{(1-\sigma)}{(1+\sigma)} \tag{1.6}$$

$$\frac{u_b}{u_g} = 1 - \frac{2A}{\pi^2} \tag{1.7}$$

In 1987, Hass and Sturtevant performed experiments to study the interaction of planar shock waves and cylindrical or spherical volumes of gas [16]. They examined helium and refrigerant 22 (R22) for the cases of cylinder and bubble (spherical) initial conditions interacting with M=1.2 shock waves. The cylinders were 5 cm in diameter and were formed by stretching a thin (0.5 μm) nitrocellulose membrane around two 3 mm thick Pyrex disks, which formed the ends of the cylinder. The volume was then filled with the desired gas. The deformation of the initial conditions after shock acceleration was visualized using a spark shadowgraph optical system. They compared the velocities of the resulting instabilities to the linear stability analysis of Richtmyer and the theory proposed by Rudinger previously presented. They found experimental velocities that were larger than the predicted values, primarily due to wall effects of the shock tube.

In 1988, Picone and Boris used the experimental results of Hass and Sturtevant as validation for numerical simulations using the FAST2D code [17]. FAST2D is inviscid, compressible fluid dynamics code that solves the Euler equations using a flux-corrected transport method. They achieved good qualitative agreement between the experimental images and numerical results as well as good quantitative agreement between the measured velocities of the upstream and downstream edges of the instability. The numerical results were also used to examine the vorticity generated by the shock/bubble interaction and to verify the non-linear theory developed by Picone for the late-time vorticity.

In 1993, Jacobs performed experiments with cylinders of SF_6 and helium at M=1.095 [18]. These experiments differed from the previous shock tube experiments, in that the initial conditions were formed by a laminar jet of gas. This setup eliminated the membrane required to separate the initial condition gases from the surrounding atmosphere used in previous experimental work. This is advantageous as the membrane can affect the flow structure and interfere with visualization techniques. The cylinder was 0.8 cm in diameter, which is significantly smaller than the 5 cm diameter cylinder used by Haas and Sturtevant. The initial condition gases were seeded with bi-acetyl gas, which was made to fluoresce with a 430 nm laser source spread into a planar sheet. This imagining technique, called Planar Laser Induced Fluorescence (PLIF), was used to visualize cross-sectional slices of the fluid instabilities. The PLIF images were similar in morphology to the experimental images observed by Haas and Sturtevant. Jacobs also observed the formation of secondary fluid instabilities (Kelvin-Helmholtz) near the edges of the vortex pair at late times for the SF_6 initial conditions, which appeared to be caused by shear between the rotating vortex and the surrounding air. Jacobs also computed the instability displacement as a function of time and compared the results to those of Rudinger and Somers. He found that their theory under-predicted the final velocity of the vortex pair.

In 1997, Rightley et. al. [19] performed shock tube experiments for a gas curtain of SF_6 being accelerated by a M=1.2 shock wave. The SF_6 was seeded with glycol droplets to visualize the flow. They performed quantitative measurements of the instability mixing widths and used a point vortex row model based on the work of Jacobs et. al. [20] to calculate the circulation, Γ. The value of Γ was calculated by constructing curve fits to experimental data using Equation 1.8.

$$w(t) = \frac{2}{k} \sinh^{-1} \left[k^2 \Gamma(t) + \sinh\left(\frac{k w_0}{2}\right) \right] \tag{1.8}$$

They also performed an analysis of the tracking fidelity of the glycol droplets used as a passive tracer. They calculated the response time of the particles and found that there was a 3 μs delay in the acceleration of a 0.5 μm particle to the piston velocity behind the shock. This resulted in the conclusion that while the droplets do not perfectly follow the flow, the droplets would track the subsequent instability that formed and yield accurate measurements of the post-shock flow.

In 1998, Vorobieff et. al. [21] used the same experimental setup as Rightley et. al. [19] to explore the transition of the instability to turbulence. They constructed second-order structure functions based on the intensity of the light scattered off of the gas curtain. Experiments were run for single and multi-mode initial conditions. Their results showed that as the gas curtain evolved towards a fully mixed state, the structure functions approached a power-law behavior with an exponent near 2/3. This behavior is often considered to be a signature of fully developed incompressible turbulence.

In 2000, Prestridge et. al. [22] performed Particle Image Velocimetry (PIV) measurements on experiments similar to those reported by Rightley et. al. [19] and Vorobieff et. al. [21]. The PIV allowed for the generation of velocity fields which were used to calculate the circulation in the flow. The circulation was compared to the model presented by Rightley and found to be in good agreement.

In 2002, Zoldi performed an experimental and numerical study of a cylinder of SF_6 accelerated by a M=1.2 shock [23]. The initial conditions were seeded with glycol droplets to allow for visualization and for use in PIV. Numerical simulations were performed with the RAGE code, which is a multi-dimensional, adaptive mesh, Eulerian hydrodynamics code. Experimental were performed in the facility used in the work of Rightley, Vorobieff, and Prestridge. The numerical results were qualitatively compared to experimental results and showed good agreement. Quantitative comparisons were made between the results by examining the height and width of

the instability, the spacing between the vortex pairs, the convective velocity of the instability, and the circulation. To match experimental results, the concentration of the SF_6 in initial conditions was reduced to 60% and the density gradient was diffused to eliminate a sharp interface between the air and initial condtions. This change was validated by obtaining images of the initial SF_6 concentration gradients using Planar Laser Rayleigh Scattering (PLRS). These images showed the SF_6 cylinder to be larger and more diffuse than the glycol droplets used as passive scalars. No attempts were made to numerically model the glycol droplets, but these results highlight the importance of understanding the behavior of passive tracers.

In addition to traditional RMI formed at the interface of two fluids, this dissertation also explores a multiphase analogue, where a shock wave accelerates a region seeded with droplets. There has been little work in the area of multiphase RMI. In 2010, Ukai performed numerical simulations for traditional and multiphase RMI for a single-mode perturbation [4]. Three types of simulations were performed, the first with a shock wave traveling from a light to a heavy gas, the second with a shock wave traveling from a light gas to a region of heavy gas seeded with particles, and a third with a shock wave passing into a region with particles and no heavy gas. The work showed numerically that the Stokes number (St), which is a measure of the particle response time over a characteristic distance, and the seeding density play an important role in how particles respond to the passing shock wave. In the case of a low Stokes number ($St << 1$), the particles behaved as passive tracers and were nearly instantaneously accelerated to the material velocity behind the shock. In this case, a RMI like instability formed with growth rates predicted by Richtmyer's theory. When the Stokes number was large, however, the particles would move relative to the flow and the acceleration was not impulsive. In this case, the instabilities that formed behaved more like a traditional Rayleigh-Taylor instability. The work also included a linear stability analysis based on a dusty-gas formulation [24] that assumes the volume fraction of the particles is very small, and that particle-particle

interactions (collisions) are negligible. It was found that for $St << 1$ the multi-phase growth model asymptotes to traditional RMI.

The first experimental proof of a multi-phase RMI analogue was reported by Vorobieff et. al. in 2011 [1]. Experiments were performed for a cylinder of air seeded with glycol droplets accelerated by shock waves at M=1.2, M=1.67, and M=2.02. The instabilities that were observed were compared with instabilities formed by similar strength shock waves interacting with a cylinder of SF_6 (traditional RMI). While the size of the gas columns were initially the same, the traditional Richtmyer-Meshkov instabilities were significantly larger than the multi-phase analogue. These results are presented in detail in Chapter 4, where they are compared to results of numerical simulations.

1.4 Narrative Summary

This dissertation covers the experimental and numerical study of shock accelerated single and multi-phase initial conditions performed in the University of New Mexico shock tube facility. Chapter2 presents the experimental and numerical methods used in these efforts. Chapter 3 covers experimental and numerical results for a cylinder of SF_6 seeded with glycol droplets accelerated by M=1.22, M=1.67, and M=2.0 shock waves. Chapter 4 covers experimental and numerical results for a cylinder of air seeded with glycol droplets accelerated by similar strength shock waves. Chapter 5 presents a quantitative analysis of the perturbation amplitude growth rate for single-phase RMI. Chapters 6 explores the assumption of a quasi two dimensional flow field by examining three dimensional experimental and numerical results, while Chapter 7 explores fully three dimensional results by accelerating the initial conditions with a shock wave at an 15 degree angle of incidence relative to the initial condition cylinder. Finally, Chapter 8 summarizes all of the results presented.

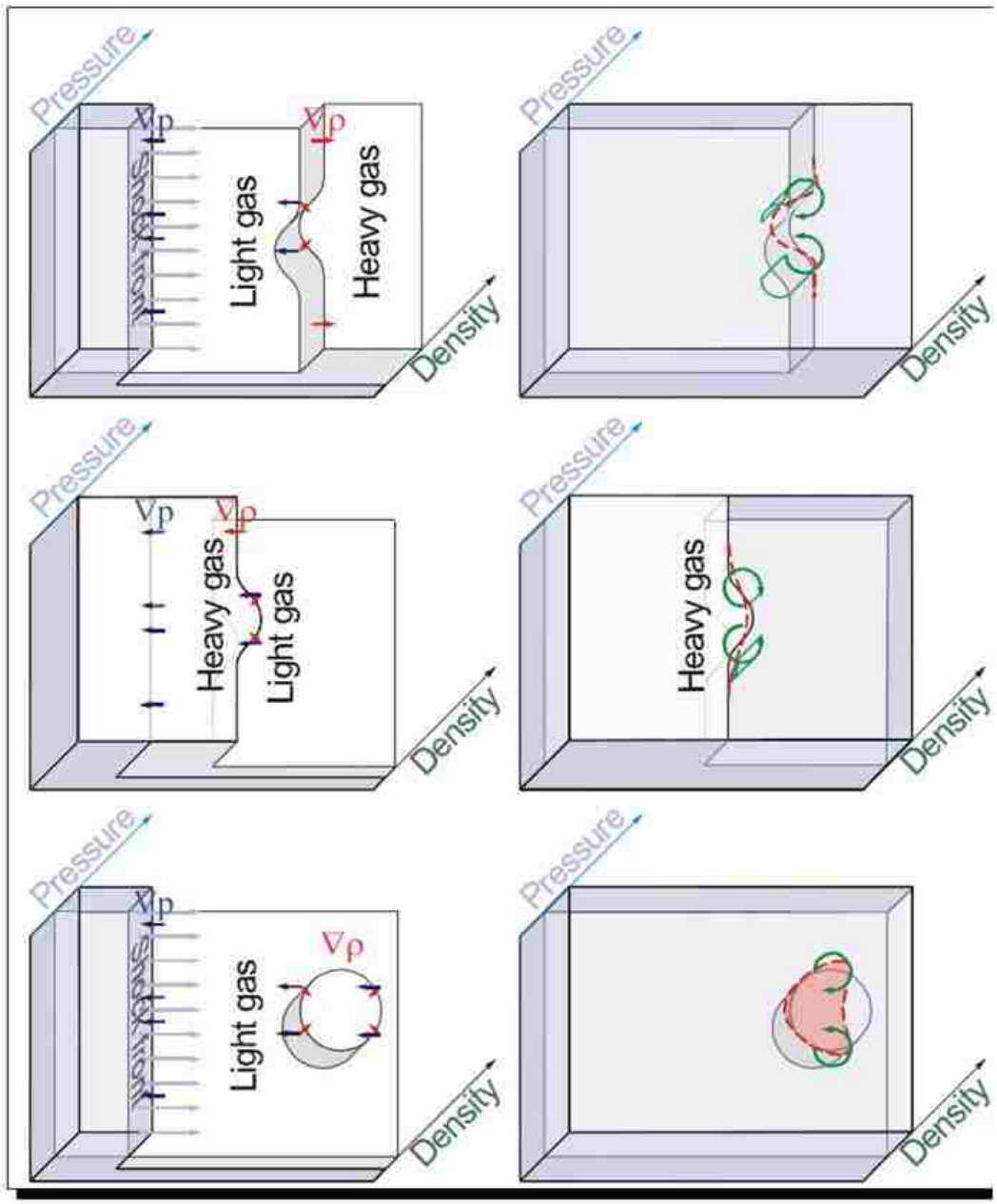

Figure 1.1: Richtymyer-Meshkov instability formation for light to heavy gas (top), heavy to light gas (middle), and a cylinder of heavy gas embedded in light gas (bottom) [5].

Chapter 2

Experimental and Numerical Methods

The experimental data presented here was obtained using the shock tube located at the University of New Mexico (UNM) shock tube facility. The facility was built with Defense Threat Reduction Agency (DTRA) funding in 2007-2009. The details of the facility and the experimental setup are given in the first section. The numerical simulations of the shock tube experiments were performed using the Computational Fluid Dynamics (CFD) code SHAMRC. To get a detailed characterization of the experimental initial conditions, the CFD code FLUENT was used. A synopsis of both codes is given in the second and third sections respectively.

2.1 Experimental Methods

The UNM shock tube facility, shown in Figure 2.1 and 2.2, is used to study planar and oblique interaction of shock waves with gaseous density interfaces and multiphase flows. The shock tube is comprised of a driver section, a driven section, an optically

transparent test section, and a run-off section. The shock tube is mounted to the wall in a manner that allows for variation in both the height of the shock tube from the floor and the angle with respect to horizontal. The shock tube can be raised to a height of six feet in a horizontal configuration and tilted to angles as high as 30 degrees from the horizontal position (this limit is imposed by the height of the ceiling in the facility). In addition, the shock tube is isolated from vibrations through a series of rubber dampers. The flexibility of the mounting system allows for a variety of test configurations and enables the subtraction of background images used in high speed imaging. For the experiments described in this work, the shock tube was mounted both horizontally and at an angle of 15 degrees.

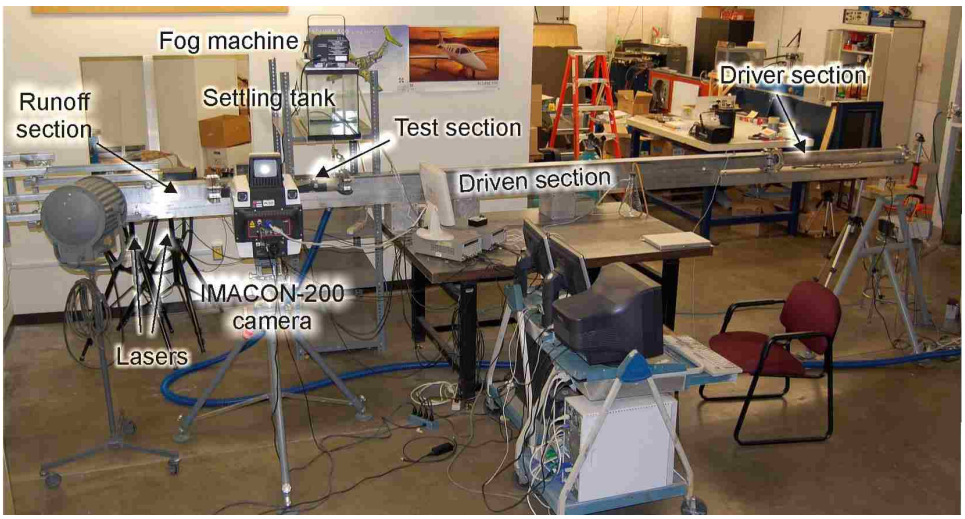

Figure 2.1: UNM shock tube facility

Before an experimental run, a polypropylene diaphragm is inserted between the flanges of the driver and the driven section, which makes it possible to pressurize the driver section. For these experiments, the driver gas was helium. The diaphragm is ruptured by an electrically driven four-blade puncturer mounted inside of the driver section, releasing a planar shock wave into the driven section. The diaphragms are roughened pre-shot to ensure a clean rupture. To increase the strength of the shock

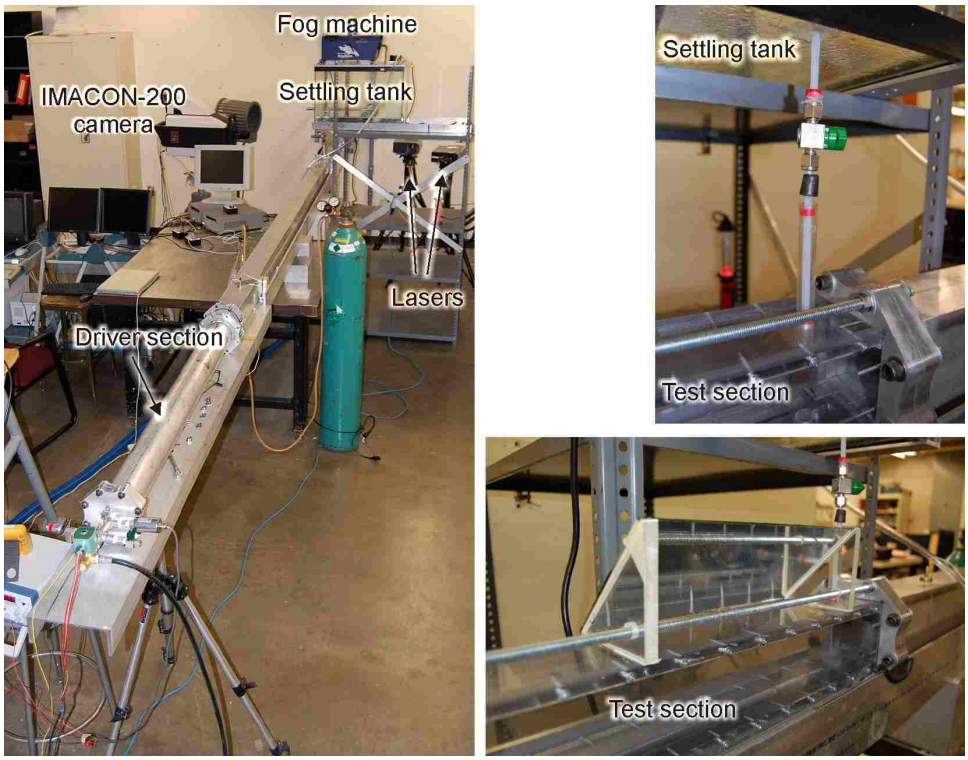

Figure 2.2: View of the experimental setup from the upstream direction with close-ups of the concentric-flow nozzle and test section.

generated, the driver section is pressurized to higher levels, as such, the number of diaphragms required is also increased. A shot at $M = 1.67$ utilizes two diaphragms and a shot at $M = 2.02$ requires 3 diaphragms. Alternatively, a paper diaphragm can be used for low Mach number shots. In this case, the strength of the shock is adjusted by varying the number of sheets placed in between the driver and driven sections. This method reliably ruptures at a given pressure determined by the number of sheets used and does not require the use of the puncture device described earlier. In the case of $M = 1.22$ shots, a single piece of paper is required. Table 2.1 shows the values of pressures required for typical shock strengths used in this work.

The driven section, whose total length is 3.2 m, is instrumented with two Omega pressure transducers that are connected to a National Instruments PXI-1002 board

Table 2.1: Shock tube pressures for various Mach numbers

Mach Number	Piston Velocity ($\frac{m}{s}$)	Pressure (Pa)
1.2	103.97×10^4	1.53063×10^5
1.67	303.73×10^4	4.13685×10^5
2.0	425.31×10^4	8.27370×10^5

with a digital oscilloscope. The latter transfers the recorded pressure traces to a computer, where they are stored for post processing and analysis. The pressure signal from the second transducer indicates the passage of the shock wave and is used to trigger a Stanford Research DG-535 digital delay generator. The delay generator sends trigger signals to the high speed imaging system. Images are recorded by a DRS Imaging IMACON-200 high framing rate intensified camera with a 1200x980 pixel frame resolution with ten bits per pixel. The images are illuminated by two New Wave Gemini double-pulsed Nd:YAG lasers. Each laser pulse is triggered by a separate pulse from one of the two DG-535 delay generators. The presence of two delay generators is necessitated by each having only four trigger channels, while the desired number of trigger signals is five (one for the camera and four for the laser pulses).

The laser pulses are emitted at 532 nm, have a duration of about 5 ns, and an optical energy about 0.2 J per pulse. As each laser head has a maximum repetition rate of 15 Hz, there are only four laser pulses (two heads per laser) available for each experiment, thus limiting the number of exposures per experiment to four. Each laser is mounted on a tripod along with a cylindrical lens and a spherical lens that expand the laser beam into a laser sheet. These laser sheets illuminate the same horizontal or vertical planar section of the flow, passing through the transparent wall of the shock tube. The entire test section of the shock tube is built of 12.7 mm thick polycarbonate for unimpeded optical access.

Experimental images are obtained in one of two possible observation planes. The first configuration consists of laser sheets that pass through the test section on a horizontal plane. The laser sheets illuminate a horizontal cross-section of the instability which is captured by the camera via a mirror placed at a 45 degree angle above the test section. The second configuration utilizes the same mirror to direct the laser sheet vertically through the test section. In this configuration, the camera is able to obtain experimental images directly through the side of polycarbonate test section.

To generate initial conditions, a 75 liter settling tank above the test section is filled with a mixture of the injected gas (air or sulfur hexafluoride) and droplets. In the experiments described in the following chapters, an American DJ Stallion commercial fog-making machine was mounted on top of the settling tank to discharge fog (dipropylene glycol droplets with an average diameter between 1 and 10 microns) into the tank. The fog that is produced is hotter than ambient air. To counteract buoyancy effects, the fog plume is directed into an ice bath placed inside the settling tank directly below the fog machine. If particles coalesce to scales larger than micron-sized, they settle to the bottom of the tank and are not injected into the test section. The initial conditions flow from the tank via a plastic tube with protrudes into the tank 3 inches. The tube ends in a valve which can be turned on or off to start or stop the flow of the gas column.

The air-droplet or SF_6-droplet mixture is injected into the shock tube through a concentric-flow nozzle mounted flush with the top wall of the test section. Two different tubes were used as inner nozzles in this work. The earliest work presented, which includes late time images of RMI and the images of the multiphase RMI, used a plastic tube with an inner diameter of 6.35 mm. This tube was easily deformed, affecting the quality of the initial conditions. The tube was replaced by an aluminum tube with the same outer diameter, but with an inner diameter of 4.5 mm. This change improved the quality of the initial conditions, making the experimental results

more repeatable. The inner tube carries the droplet-seeded air or SF_6. Unseeded air flows through the outer concentric nozzle which has a 19.05 mm diameter. This concentric nozzle setup reduces shear between the quiescent air filling the test section and the droplet-seeded jet. The jet moves at a velocity of approximately 1 m/s, which is 2 orders of magnitude smaller than the typical velocity of gases behind the shock front. The axis of the concentric flow nozzle is vertical, so the flow of the gas-droplet mixture (which is heavier than air) is gravity-stabilized. At the bottom of the test section, the droplet-seeded jet exits through a 19.05 mm diameter hole. A gentle suction is applied to this hole to ensure that the bottom of the initial condition column does not transition to turbulence. The density of SF_6 is roughly 5 times heavier than air, so gravitational forces acting on the fluid are sufficient to drive these initial conditions through the test section. The air-droplet initial conditions have roughly the same density as air, therefore, a small positive overpressure is applied to the settling tank in the form of a fan to force these initial conditions through the test section.

Measurements of the average SF_6-droplet and air-droplet mixture density in the settling tank were performed as follows. For the SF_6-droplet initial conditions, the settling tank was filled with SF_6 and a 0.83 liter sample container was filled from the plastic tube used to feed the injection nozzle. The container was filled through a hole in the lid for a period of two minutes to ensure that the container was completely full. It was found that filling the container for more than two minutes did not change the measured mass. The container was weighed on a scale accurate to 0.01 grams. After each measurement, the container was purged of SF_6 and re-weighed. The difference in the weight of the full and empty container gives a mass which can be divided by the container volume to give the average density. A series of these measurements were taken and averaged together, resulting in an average density of 3.701 kg/m^3. Measurements were also taken with the SF_6 seeded with glycol droplets and it was found that the seeding had a negligible effect on the measured mass. The

ambient density of the air in the laboratory based on the temperature and pressure was calculated as 1.18167 kg/m^3 on the day of the measurements. This yields an Atwood number of approximately 0.5.

For the air-droplet mixture, a 1 liter sample container was placed into the tank near the hole drilled in its bottom for the attachment of the nozzle. The tank was filled with droplets from the fog making machine. Then the sample container was closed with a tight-fitting lid, removed, and weighed on a scale accurate to 2×10^{-4} g. Subsequently, the lid was removed, the contents of the container flushed with air, the lid put back, and the weight recalculated. Comparison of the two measurements produces the density difference due to the presence of the droplets. Multiple repetition of the measurements results in an average density of 0.062 kg/m^3 for the air-droplet initial conditions. Based on the air density calculated above, this yields an Atwood number of approximately 0.03.

2.2 Numerical Modeling with SHAMRC

The Eulerian computer code SHAMRC (pronounced shamrock) is a two or three dimensional, finite difference, hydrodynamic computer code. SHAMRC, which stands for **S**econd-order **H**ydrodynamic **A**utomatic **M**esh **R**efinement **C**ode, is a descendant of SHARC (**S**econd-order **H**ydrodynamic **A**dvanced **R**esearch **C**ode), which is in turn a descendant of the HULL code developed at the Air Force Weapons Laboratory (AFWL) in the early 1970's. It is used to solve a variety of airblast related problems which include high explosive (HE) detonations, nuclear explosive (NE) detonations, structure loading due to airblast, thermal effects on airblast, cloud rise, conventional munitions blast and fragmentation, shock tube phenomenology, dust and debris dispersion and atmospheric shock propagation. The code has the capability to run with a single Eulerian grid or with the Automatic Mesh Refinement (AMR)

option that divides the computational domain into smaller Eulerian grids at several levels of refinement to provide high-resolution results [25]. Its capabilities and attributes include multiple geometries, non-responsive structures, non-interactive and interactive particles, several atmosphere models, multi-materials, a large material library, HE detonations, a K-ϵ turbulence model, and water and dust vaporization. SHAMRC is second-order accurate in both space and time and is fully conservative of mass, momentum and energy. It is fast because it employs a structured Eulerian grid and efficient due to the use of the pre-processor SRCLIB. SHAMRC was used in this work to model the interaction between the passing shock wave and both types of initial conditions. The details of these calculations are discussed in the following chapters.

One of the features of SHAMRC that makes it efficient is that a custom set of code is tailor made for each problem. SHAMRC does not exist as a single executable, instead, a collection of source files exist as meta-code. This meta-code forms a library that is managed by a program called SRCLIB [26]. The user "makes" the code prior to each calculation by running the SRCLIB pre-processor, thus creating a FORTRAN source file that contains code specific to the options set in an input file. The code is then compiled to create an executable. In addition to getting only the code specific to the requirements of a problem, when the source code is made any data structures that are required are dimensioned to the correct size to minimize memory usage. In essence, the making process optimizes SHAMRC for a particular problem, decreasing the time and memory required to complete the simulation. Users also have the ability to make changes to the source code through a standalone file which is incorporated into the SHAMRC libraries during the making process. This allows users to develop new models or make changes to existing models as they see fit. The SHAMRC library contains several files, but there are three main programs necessary for any calculation. Program KEEL is used to setup the computational grid and any associated models. Program SHARC is the finite difference solver that advances the fluid flow state in

time. Finally, program PULL is used to plot the results generated by KEEL and SHARC. Each of these programs and the options required to run them are covered in great detail in the SHAMRC User's Manual [27] and will not be described here.

An overview of the SHAMRC differencing method and any models relevant to the calculations performed for this work is provided below. Readers who are interested in a more detailed examination of the differencing method, other models, or the parallel implementation are directed to the SHAMRC Methodology Manual [25]. SHAMRC solves the conservation equations for mass, momentum, and energy for a compressible, non-conducting, inviscid fluid, which are given in Equations 2.1, 2.2, and 2.3. Also required for closure is a relation, or equations of state, defining the pressure in a zone based on the density and internal energy. A list of the variable descriptions and their units is given in Table 2.2.

$$\left(\frac{\partial}{\partial t} + \vec{v} \cdot \vec{\nabla}\right) \rho + \rho \vec{\nabla} \cdot \vec{v} = 0 \tag{2.1}$$

$$\rho \left(\frac{\partial}{\partial t} + \vec{v} \cdot \vec{\nabla}\right) \vec{v} + \vec{\nabla} P + \rho \vec{\nabla} \phi - \kappa \nabla^2 \vec{v} = \vec{0} \tag{2.2}$$

$$\rho \left(\frac{\partial}{\partial t} + \vec{v} \cdot \vec{\nabla}\right) E + \vec{\nabla} \cdot P\vec{v} + \rho \vec{v} \cdot \vec{\nabla} \phi - \kappa \nabla^2 H - \rho \dot{Q} = 0 \tag{2.3}$$

The solution method of the preceding equations is a conservative, two-phase, operator-split, explicit, time-marching method that is second-order accurate in space and time. The basic fluid equations are divided into Lagrangian and Eulerian terms and their solution is divided into two corresponding phases. The energy redistribution terms are treated in a separate routine after the Lagrangian update, and before the Eulerian remap. Figure 2.3 outlines the order of the solution phase.

Table 2.2: Shock tube pressures for various Mach numbers

Variable	Description	Units
ρ	material density	$\frac{g}{cm^3}$
P	pressure	$\frac{dynes}{cm^2}$
I	specific internal energy	$\frac{ergs}{g}$
$\vec{v}$	fluid velocity vector	$\frac{cm}{s}$
$E = I + \frac{\vec{v}\cdot\vec{v}}{2}$	total energy density	$\frac{cm}{s^2}$
ϕ	external potential (e.g., gravity)	$\frac{ergs}{g}$
κ	turbulence energy density	$\frac{ergs}{g}$
$\dot{Q}$	heat or energy transfer	$\frac{ergs}{g-s}$
t	time	s

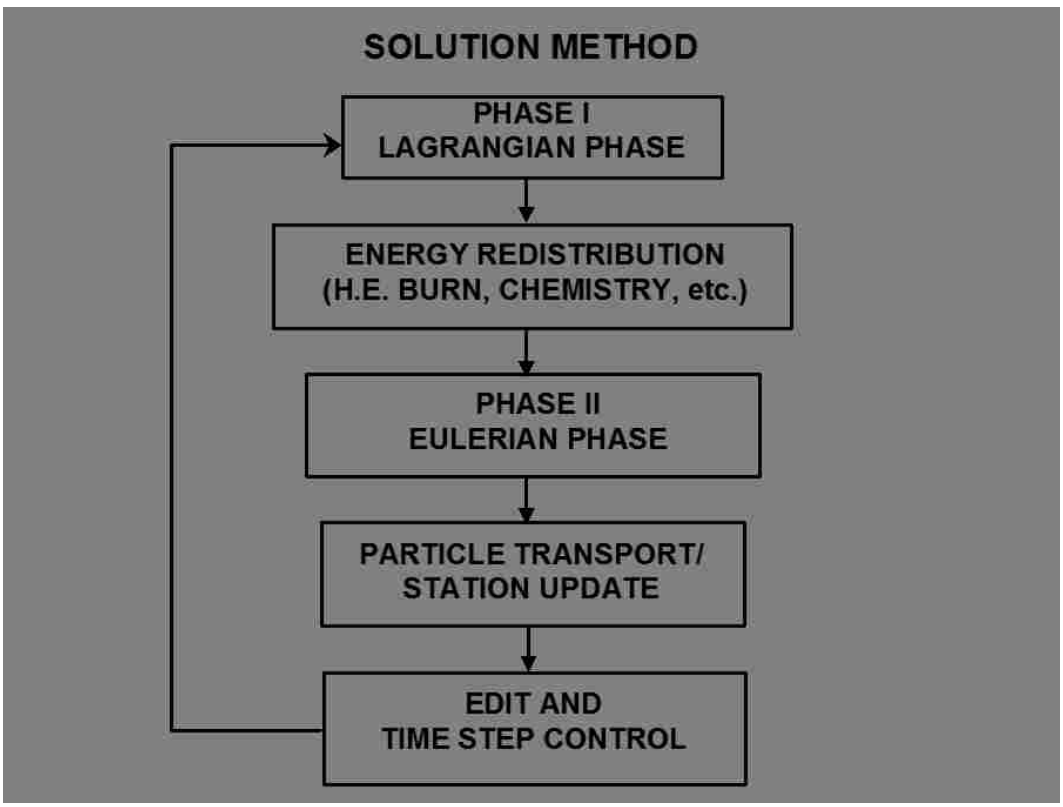

Figure 2.3: SHAMRC solution phase program flow.

The first phase is a Lagrangian step in which the conservation equations are solved in a Lagrangian frame of reference. The boundary values are calculated for each zone based on zone centered quantities and the velocity and energy are updated by a half time step. These boundary values are used to calculate an intermediate pressure at the zone boundaries, which is in turn used to update the zone energy and velocity by a full time step. After the Lagrangian phase any energy transfer models are applied. Some examples are radiation transport, high explosive detonation, or chemical reaction, etc. Note that this phase is absent for the calculations performed here. The second phase is the Eulerian part of the solution. The first phase essentially performs a second-order Lagrangian calculation. Since SHAMRC is based on an Eulerian reference frame, the results of the first phase must be remapped into the fixed mesh. This takes the form of an advection calculation which fluxes hydrodynamic variables. The method is conservative of mass, momentum, and energy and completes a single SHAMRC time step. If particles are present in the calculation, they are processed after the completion of this phase. As particles motion is important to the calculations performed here, the SHAMRC particle model will be explored in more detail.

SHAMRC has the capability to model Lagrangian particles that move through the mesh. Each particle can exchange mass, momentum, and energy with the surrounding fluid. Mass can be exchanged via particle combustion or droplet evaporation, however these models are not used in this work. The particles exchange momentum with the fluid via drag forces and energy exchange is performed via heating or cooling due to conduction and convection. Each particle has a position, velocity, mass, radius, density, and energy and can be thought of as a computational particle representing a cloud of tens or hundreds of millions of physical particles in the case of micron sized particles. The cloud is given the physical characteristics of an individual particle, which include the radius and material properties. These properties are used to calculate the mass, momentum, and energy exchange for the computational

particle cloud. The particles are assumed to have a much higher density than the embedding fluid, and as such have a negligible volume. Since the particle volume is neglected it does not affect the pressure calculation for fluid in a computational zone. There exist situations when particles are tightly packed and this assumption is not valid. There are special models in SHAMRC to take into account the volume of a cloud of particles and the effects of this tight packing on the cloud response in terms of momentum exchange through an increased drag coefficient. As the packing density of the fog droplets in the initial conditions is low, these models are not needed for this work. The particles are spherical in nature and are subjected to drag forces according to the equation for drag over a sphere, given in Equation 2.4 [28]. In this equation, Re is the particle Reynolds number given by $Re = \frac{\rho_g * V * D_p}{\mu_g}$, where ρ_g and μ_g are the gas density and dynamic viscosity, V is the particle velocity, and D_p is the particle diameter.

$$C_d = 0.47 + \frac{36}{Re} \tag{2.4}$$

In addition to the standard particle drag law, there is also a correction for the Mach number of the flow. The form of the correction is given in Equation 2.5 [29]. In these equations, C_d^{sp} refers to the drag coefficient for a spherical particle.

$$\begin{aligned}
C_d &= C_d^{sp} && M < 0.3 \\
C_d &= C_d^{sp} + \frac{1 - 0.47}{1.5 - 0.3}(M - 0.3) && 0.3 < M < 1.5 \\
C_d &= C_d^{sp} + \frac{0.93 - 1}{6.0 - 1.5}(M - 1.5) && 1.5 < M < 6.0 \\
C_d &= C_d^{sp} + 0.46 && M > 6.0
\end{aligned} \tag{2.5}$$

2.3 Numerical Modeling with FLUENT

The CFD code FLUENT is a commercial code distributed and maintained by ANSYS, Inc. It provides comprehensive modeling capabilities for a wide range of incompressible and compressible, laminar and turbulent fluid flow problems. FLUENT can model a broad range of transport phenomena (heat transfer, chemical reactions, etc.) and can model complex geometries. FLUENT also has several methods of modeling multiphase flows. FLUENT solves the mass, momentum, and energy conservation equations for a fluid flow. As opposed to SHAMRC, where Euler's equations are solved for momentum conservation, FLUENT also has the capability to solve the full Navier-Stokes equations. In light of this, FLUENT was used to develop a model of the initial conditions that could be used as input for the 2D and 3D SHAMRC calculations. The code's mass diffusion and multiphase modeling capabilities were used to model how the cylinder of SF_6 seeded with glycol droplets evolved as it flows from the initial condition tube and through the shock tube test section. The calculation setup and results are presented in Chapter 3. The exact details of the FLUENT models will not be discussed here, as it is commercial software and the documentation is readily available in the form of the theory [30] and user [31] manuals.

Chapter 3

Richtmyer-Meshkov Instabilities

3.1 Overview

A Richtmyer-Meshkov Instability (RMI) [2, 3] is generated when an interface between two fluids of differing density is impulsively accelerated. The instability develops due to misalignment of the density and pressure gradients. This misalignment results in the deposition of vorticity, causing the formation of an instability that grows non-linearly with time and eventually may transition to fully turbulent flow. In this work, RMI experiments were performed initially as control experiments to test the high speed imaging system, develop timings for future experiments, and to validate numerical modeling. The results presented in this chapter are obtained at an Atwood number of 0.5 for Mach numbers 1.22, 1.67, and 2.02 at multiple downstream locations.

3.2 Experimental Results

Experimental data was acquired primarily at two downstream camera positions. The first position was centered at 16.51 cm from the initial conditions. The camera frame width was 5.08 cm, so that images could be acquired from 13.97 cm to 19.05 cm downstream of the initial conditions. Figure 3.1 shows typical images obtained at this downstream location for three Mach numbers. Here, the shock passes over the cylindrical initial conditions from left to right, forming the instability. There are two structures visible in these images. The first is the edge of two counter-rotating vorticies. Noticeably absent absent is any structure inside of the instability. This fact will be explored further in the next section. The second structure visible is a protrusion or jet of material from the center of the instability. As the RMI grows, secondary baroclinic instabilities cause perturbations in the vortex cores while Kelvin-Helmholtz instabilities cause perturbations at the edge due to shear with the surrounding flow. When the perturbations on the edges of the vortex cores meet at the centerline of the instability, they merge to form this structure. Again, this phenomenon will be explored in greater detail in the next section.

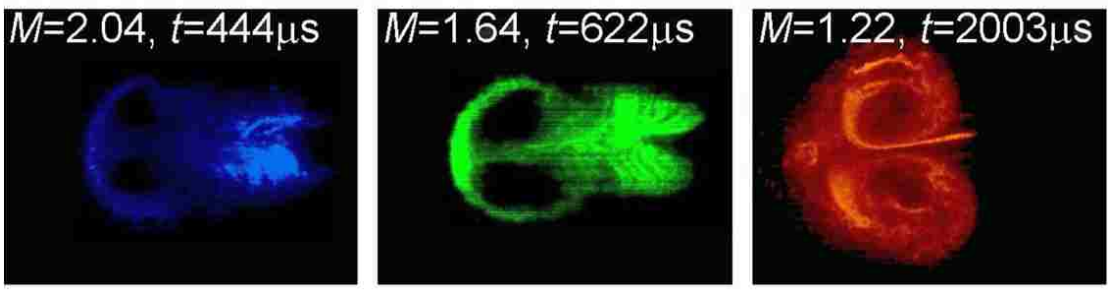

Figure 3.1: RMI at 19.05 cm downstream of the initial conditions for Mach number 1.22, 1.64, and 2.04 [1].

The second set of images were taken at a point just downstream of the initial conditions. The camera was centered so that images could be obtained as the shock

passed through the initial conditions. These images show the initial development of the instability and provide a good baseline for comparison with early time numerical results. Figure 3.2 shows the evolution of the RMI for five times at an interval of 50 μs starting with the initial conditions. The laser illumination is narrowed into a thin sheet, however, nearby droplets above and below the laser sheet in the initial conditions are also illuminated. This provides a look at the column on initial conditions in addition to a single planar slice. The formation of the two counter-rotating vorticies is clearly visible. These images will be used for validation of the SHAMRC modeling of RMI at early times and as a baseline comparison for the early time formation of the multiphase instabilities introduced in the next chapter.

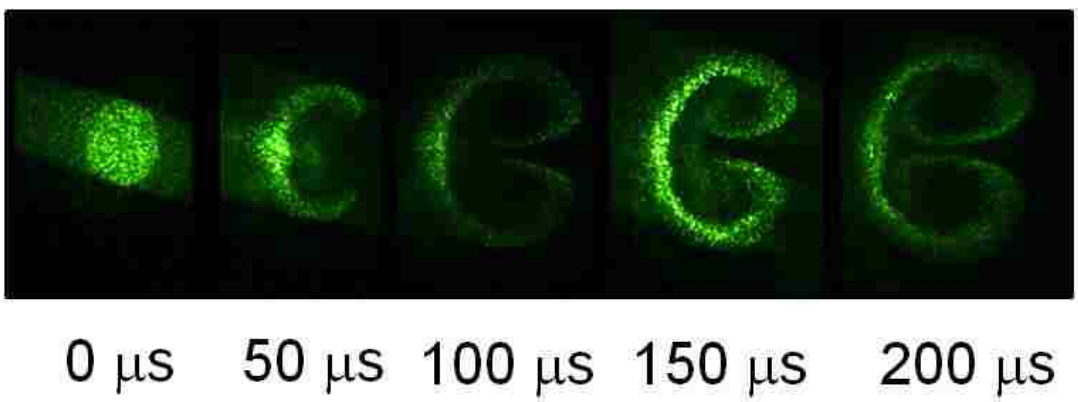

Figure 3.2: RMI at early times.

3.3 Initial Condition Characterization

The density of the gas in the settling tank was measured as described in Chapter 2 and found to be $3.701 \times 10^{-3} \frac{g}{cm^3}$. Initial SHAMRC calculations with a cylinder of initial conditions at this density and a diameter equal to that of the initial conditions tube produced an instability with a different morphology than what was seen in experiments. The instability exhibited the two counter-rotating vortices, but also

produced various secondary structures that were not observed. Tomkins et. al. [32] and Zoldi [23] observed that when SF_6 is used as the initial conditions gas, the cylinder that is formed has a lower density near the edges due to diffusion with the surrounding air. Tomkins also found that the maximum concentration of SF_6 was approximately 0.84 % by mass, which agrees well with the measured density of the gas in the settling tank. Numerical simulations of the injection system were performed to obtain a detailed description of the density field as a function of cylinder radius.

The CFD code FLUENT was used to model the injection system. The simulation was performed in 2D axisymmetric coordinates with the species transport model enabled to capture the effects of diffusion. Gravity effects were enabled to drive the heavier gas down through the test section, as this is the primary mechanism for forming the initial conditions in the lab. The flow was assumed to be laminar, so no turbulence models were used. This assumption was based on the maximum flow velocity through the pipe, which was found to be approximately 1.5 m/s in the FLUENT calculation. From this velocity and the gas properties of the initial conditions, the Reynolds number ($Re = \frac{\rho V d}{\mu}$) is approximately 1200. This value is well below the typical Reynolds number for transition to turbulent flow, $Re \approx 6300$ [28].

Figure 3.3 shows the injection system as modeled in FLUENT. The top region represents the settling tank. This area is initially filled with a mixture of SF_6 and air to obtain the measured density. The same mixture was fed into the top boundary at the same ratio via an ambient pressure boundary to keep the settling tank filled. Directly below the settling tank is the initial condition feeder tube. The resolution in the tube is 0.45 cm, with 10 elements spanning the radius of the tube. Outside of the feeder tube is the co-flow nozzle. The nozzle resolution is the same as the feeder tube with 13 elements spanning the thickness. The co-flow nozzle is fed at the top by a mass flow inlet to maintain the shape of the initial conditions. The actual flow

through the experimental setup was not measured, so a mass flow of $1 \times 10^{-4} g/s$ was chosen to approximately match the velocity in the feeder tube. Both the feeder tube and co-flow nozzle discharge into the test section. The test section is bounded top and bottom by solid walls and at the sides by an ambient pressure inlet. Below the test section is the initial condition exit hole. It is the same diameter as the co-flow inlet and has a small negative pressure applied to it to help maintain the cylindrical shape of the initial conditions. Here the bottom boundary was modeled as a pressure exit with a pressure of 101324 Pa. Figure 3.4 shows contours of velocity magnitude and species concentration from the FLUENT calculation of the injection system. In the figure, the SF_6 concentration spreads out as the initial conditions fall through the test section. From the velocity magnitude contours, the maximum velocities occur near the center of the initial condition column and are low enough for the assumption of laminar flow to be acceptable.

Figure 3.5 shows how the species concentration of SF_6 changes as a function of radius from the cylinder center at three different heights in the shock tube. The three lines represent distances of 1.905, 3.81, and 5.715 cm from the top of the shock tube. This figure shows that the initial condition column is thicker than the diameter of the feeder tube which has a radius of 0.2286 cm. Also, the column gets wider as it falls from the top of the shock tube to the bottom. At the same time, the inner core of SF_6 narrows, resulting in a lower density gradient and Atwood number near the bottom of the shock tube.

To verify the convergence of the FLUENT model, two additional calculations were run. The first implemented second order upwind schemes instead of the first order upwind schemes used previously. The second refined the mesh by a factor of two. The species concentration versus radius plots for these calculations are shown at the mid-plane of the shock tube in Figure 3.6. There is no change in the species concentration when compared to the baseline calculation, which leads to the conclusion that the

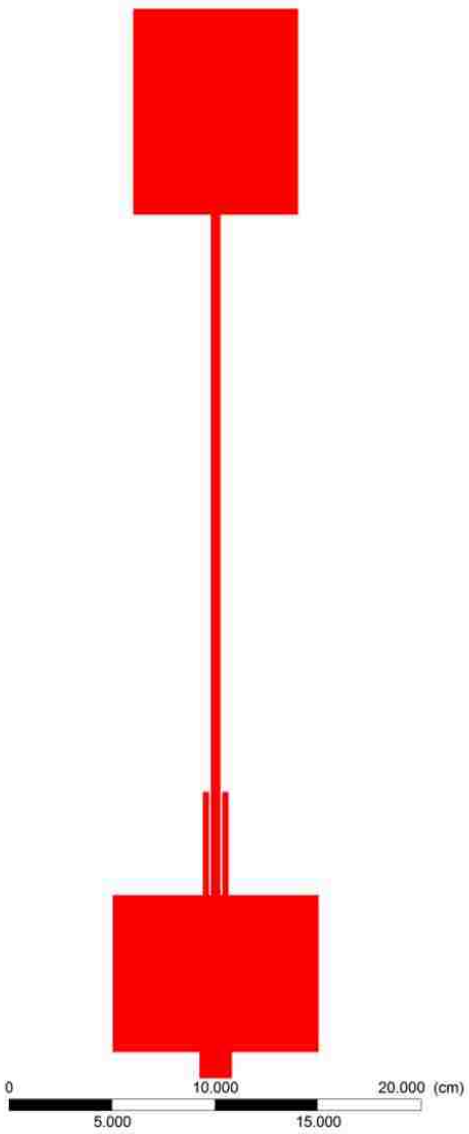

Figure 3.3: The injection system as modeled in FLUENT.

original model has converged.

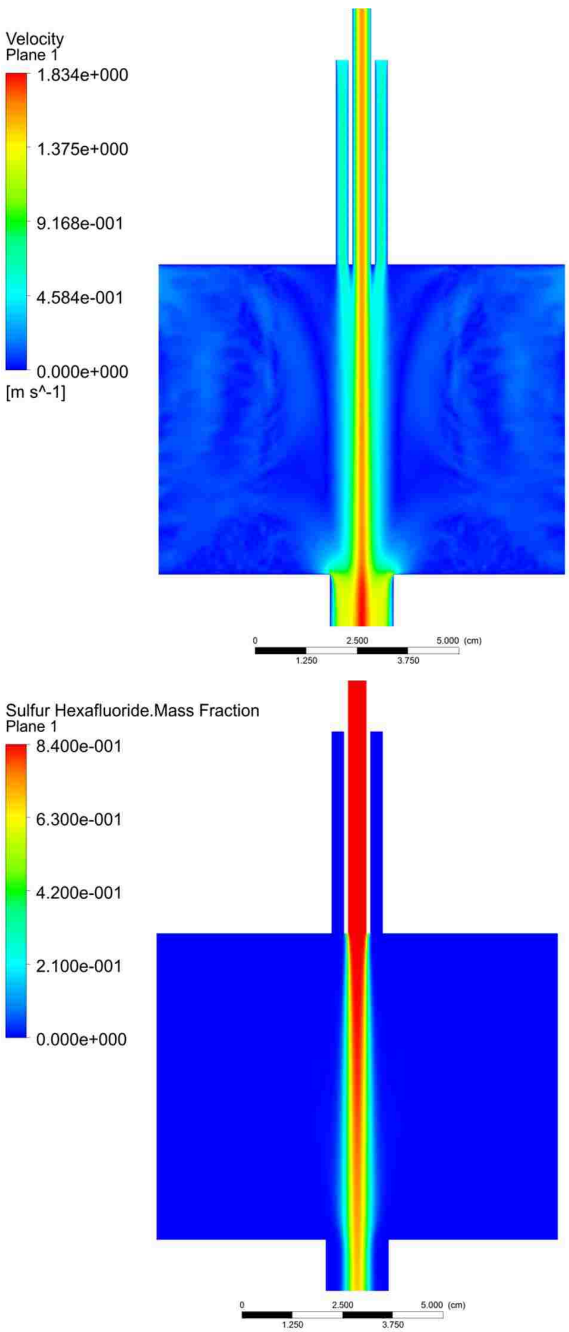

Figure 3.4: Velocity magnitude and mass fraction contours in the injection system.

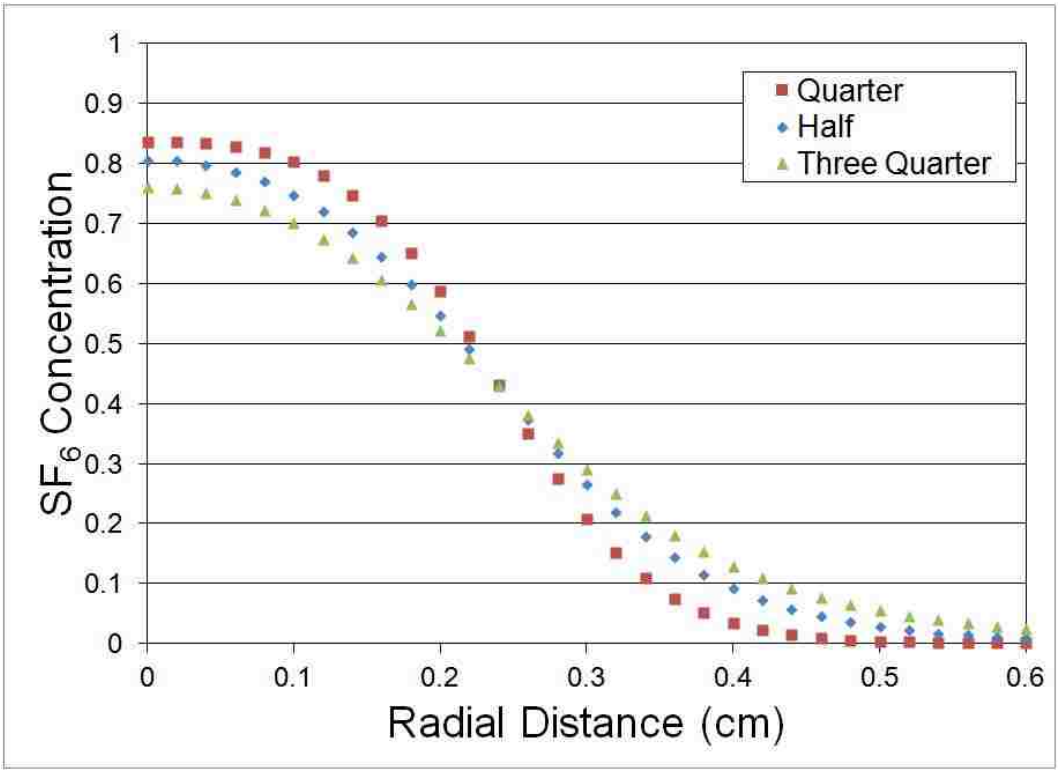

Figure 3.5: SF_6 concentration as a function of cylinder radius at 1.905 (Quarter), 3.81 (Half), and 5.715 cm (Three Quarter) from the top of the shock tube.

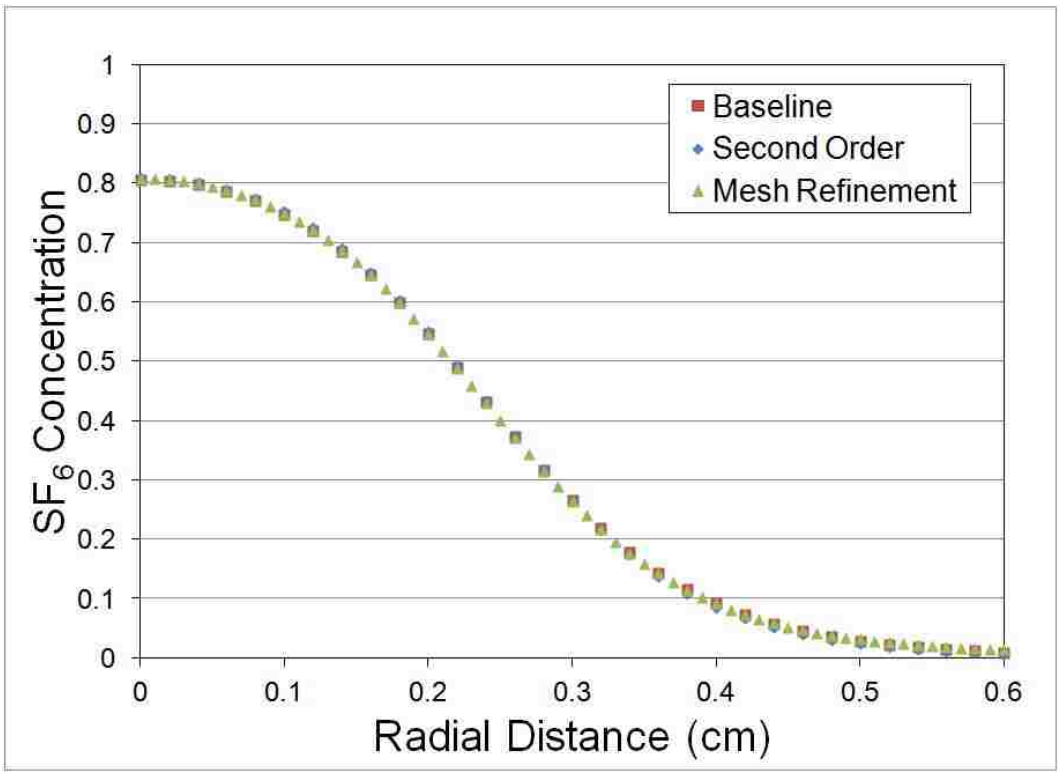

Figure 3.6: Comparison of density as a function of radius for higher order methods and increased mesh refinement.

3.4 Initial Condition Characterization

Numerical calculations to model the formation and growth of RMI were run using SHAMRC. A 2D Cartesian mesh was used with dx and dy of 0.005 cm. The mesh extended to the shock tube wall in the y direction, a distance of 3.81 cm. The x extent was set to 40 cm so that the instability could be observed in the same region as visualized in experiments before being swept from the grid. Additionally, a plane of symmetry along the x-axis was used to reduce the total number of zones required to 6 million.

To generate the shock waves in the simulations, high pressure and temperature air at a specific velocity was placed upstream of the initial conditions. To maintain steady flow, these conditions were also fed in from the left boundary. The Rankine-Hugoniot relations for a calorically perfect gas were used to determine the gas properties required to generate the appropriate Mach number. These relations are given in Equations 3.1, 3.2, and 3.3 [33]. In these equations, P is the pressure, ρ is the density, e is the internal energy, u is the velocity in a shock stationary reference frame, γ is the ratio of specific heats, and the subscripts 1 and 2 denote conditions upstream (ahead) and downstream (behind) of the shock wave respectively.

$$\frac{P_2}{P_1} = 1 + \frac{2\gamma}{\gamma+1}\left(M_1^2 - 1\right) \tag{3.1}$$

$$\frac{\rho_2}{\rho_1} = \frac{u_1}{u_2} = \frac{(\gamma+1)M_1^2}{2+(\gamma-1)M_1^2} \tag{3.2}$$

$$e_2 - e_1 = \frac{p_1 + p_2}{2}\left(u_1 - u_2\right) \tag{3.3}$$

To look at the effects of varying Mach number, experiments were performed at Mach numbers ranging from 1.22 to 2.02. Due to the variability in Mach number generated in the experiments, the numerical calculations were run at M=1.2, M=1.67, and M=2.0. While these Mach number do not exactly match their experimental counterparts, due to variations in the experimental Mach number, they do provide a reasonable approximation to the average values obtained. The material properties for air used for each Mach number are given in Table 3.1. The ambient density of air in SHARMC is $1.225 \times 10^{-3} \frac{g}{cm^3}$ and the ambient energy is $2.044 \times 10^{9} \frac{ergs}{g}$. The ambient density of air in the shock tube facility is approximately 20% lower than ambient air density, however, by matching the desired Mach number, the pressure and density ratios across the shock will be achieved regardless of the ambient conditions used in the calculations.

Table 3.1: Material Properties for SHAMRC Equation of State

Mach Number	Piston Velocity ($\frac{cm}{s}$)	Energy ($\frac{ergs}{g}$)	Density ($\frac{g}{cm^3}$)
1.2	1.0397×10^4	2.30861×10^9	1.643×10^{-3}
1.67	3.0737×10^4	2.94730×10^9	2.632×10^{-3}
2.0	4.2531×10^4	3.46533×10^9	3.267×10^{-3}

The FLUENT results were used as initial conditions in the SHAMRC calculations. To import these initial conditions in the SHAMRC model, two cubic splines were used to generate a continuous function for density as a function of radius. To transfer this information to SHAMRC, several annuli were generated with material densities equivalent to the density found from the cubic spline at a radius equal to the center of the annulus. In the experiments, the visualization plane was at the center of the shock tube, so the density profile used in the SHARMC calculations is also taken from the mid-plane of the shock tube in the FLUENT calculation. The SF_6 was modeled as an ideal gas with equations of state given by $P = (\gamma - 1)\rho I$ and

$T = (PW_M)/(R\rho)$. In these equations, P is the pressure, ρ is the density, γ is the ratio of specific heats, I in the specific internal energy, T is the temperature, W_M is the molecular weight, and R is the universal gas constant. Since the maximum species concentration exiting the settling tank was measured as 0.84, the density of the SF_6 was set to $3.675 \times 10^{-3}\ g/cm^3$, which yields an Atwood number of 0.5 at the ambient air density ($1.225 \times 10^{-3}\ g/cm^3$) found in SHAMRC. The ratio of specific heats, or γ, was set to 1.4 and the molecular weight was set to 86.83 to match the ambient temperature (287.87) in SHAMRC. The decision was made to match the Atwood number measured in the lab and not the actual density. On a given day, the pressure and temperature in the lab can vary, but the Atwood number will remain fairly constant. This choice provides a good baseline when comparing to test data.

Figure 3.7 shows density contours of the SF_6 along with the early time experimental RMI images. The images have been scaled so that they are the same size relative to each other. When comparing the density contours to the experimental images, it is apparent that the experimental initial conditions observed are smaller than the density contours. The width of the initial conditions in the experiment is approximately 0.44 cm, which is just smaller than the inner diameter of the feeder tube. Additionally, while the basic morphology of two counter-rotating vorticies is present, there are structures that appear in the SHAMRC calculations that are not visible in the experimental images. The most noticeable of which is a filament of material formed from the lower density regions surrounding the high density core of SF_6. As the instability grows, these secondary features are absorbed into the vortex core and the overall structure exhibited by the density contours matches better with the experimental images, however, there is still a noticeable absence of material at the core of the instability in the experimental images.

One possible explanation for these differences is that the density contours of SF_6 are not visible in the experimental images due to the imaging technique being used.

The SF_6 is seeded with glycol droplets, which are illuminated by the lasers. Initially, it was believed that the droplets would act as passive tracers and follow the flow exactly, leading to the highest concentrations in areas where the density is highest. From these images, it is clear that this is not the case and the droplets will have to be explicitly modeled as discrete particles to match the experimental results. This result is not surprising, as the work by Rightley et. al. [19] performed an analysis on the motion of glycol droplets embedded in a gas curtain of SF_6. They showed that the droplets do not exactly follow the fluid and that there is some lag due to acceleration of the particles by the fluid motion.

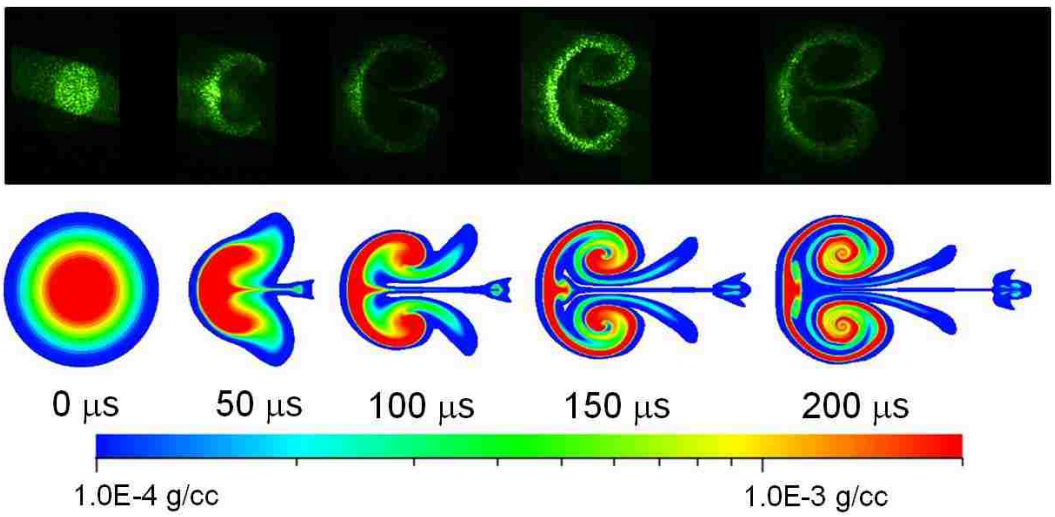

Figure 3.7: Comparison between density contours generated by SHAMRC (bottom) and experimental images (top) for early times.

3.5 Numerical Modeling with Glycol Droplets

To investigate the effects of the fog droplets on the instability formation, a SHAMRC calculation was run with the massive interactive particle model. For this calculation, particles with a diameter of 1 μm were placed uniformly into the region containing

SF_6. The total mass of particles was 1.666×10^{-5} g, which matches the density measurements outlined in the previous chapter for the air-droplet initial conditions. Tracer particles were also placed into this calculation to illustrate the differences. In SHAMRC, the velocity of a tracer particle is set to the zone velocity in which it resides and therefore follows the flow exactly. Figure 3.8 shows results for tracer particles (top) and the massive particles (bottom) at early times. By comparing Figure 3.8 with Figure 3.7, it can be seen that the tracer particles form a similar structure as the density contours, although the information about the fluid density is lost. By contrast, the massive interactive particles do not have their velocities explicitly set by the surrounding flow. They are accelerated by the flow due to drag forces and are able to slip relative to the flow. Initially, these results exhibit a similar morphology to the tracer particles, but as the counter-rotating vortex pair forms the particles are driven from the core of the vorticies by centrifugal forces. This phenomenon is also observed in the experimental images and is caused by the finite mass of the glycol droplets. The total mass of the particles is negligible when compared to the mass of the SF_6, which is responsible for the formation of this instability; however, there are phenomena that are observed solely due to the particles and the imagining technique being used. While the SHAMRC calculation with the massive particles does provide a better match to the morphology of the experimental results, it still produces an instability that is too large and exhibits secondary structures not observed in the lab.

To accurately reproduce the test images, it is necessary to better characterize the initial conditions with respect to the particles. To do this, a FLUENT calculation was run with the mixture model to simulate the presence of the glycol droplets. The mixture model allows for the simulation of multiphase flows where the phases move at different velocities, but have local equilibrium. The model is particularly useful for simulating multiphase flows in which the particulate phase is uniformly or nearly uniformly distributed in size. This model is simpler and faster than the full multiphase

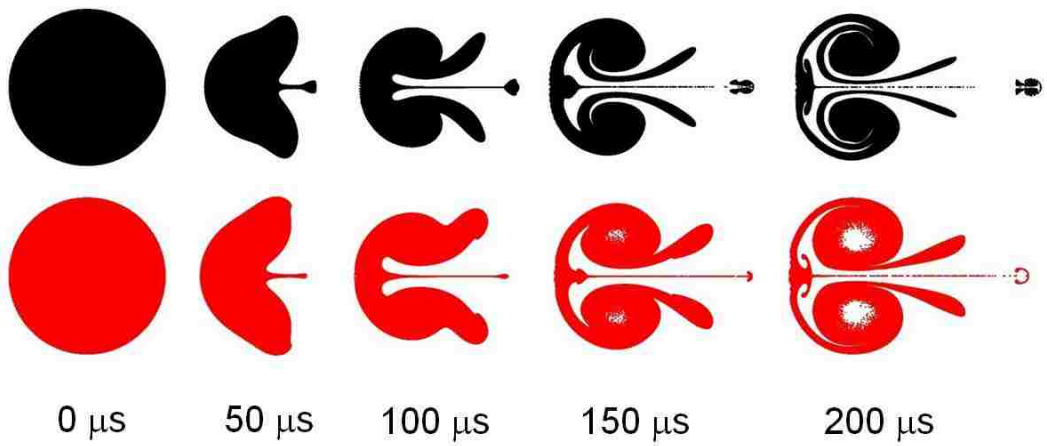

Figure 3.8: Comparison of SHAMRC calculations with tracer particles (top) and massive interactive particles (bottom) at early times.

Eulerian model and can obtain similar results for the scenarios described above. A more detailed description of the mixture model can be found in the FLUENT theory guide [31].

For this calculation, the secondary phase will be modeled as glycol droplets with a uniform diameter of 1 μm. These particles are accelerated by drag forces according to the Schiller-Naumann [31] model. The settling tank is filled with the same concentration of SF_6 with an added mass of the secondary phase corresponding to the mass reported in Chapter 2 for the air-droplet initial conditions. Figure 3.9 shows contours of the volume fraction of the particulate phase. Figure 3.10 shows a detailed comparison of the relative concentrations of the two phases at the center plane of the shock tube. The calculation shows that the particles reside in a smaller region than the SF_6. In fact, the particles occupy a region only marginally wider than the radius of the feeder tube. While mass diffusion causes the SF_6 to spread into the surrounding air, there is no similar mechanism to cause the droplets to do the same. These results match well with the initial condition diameter measured from experimental data of 0.44 cm.

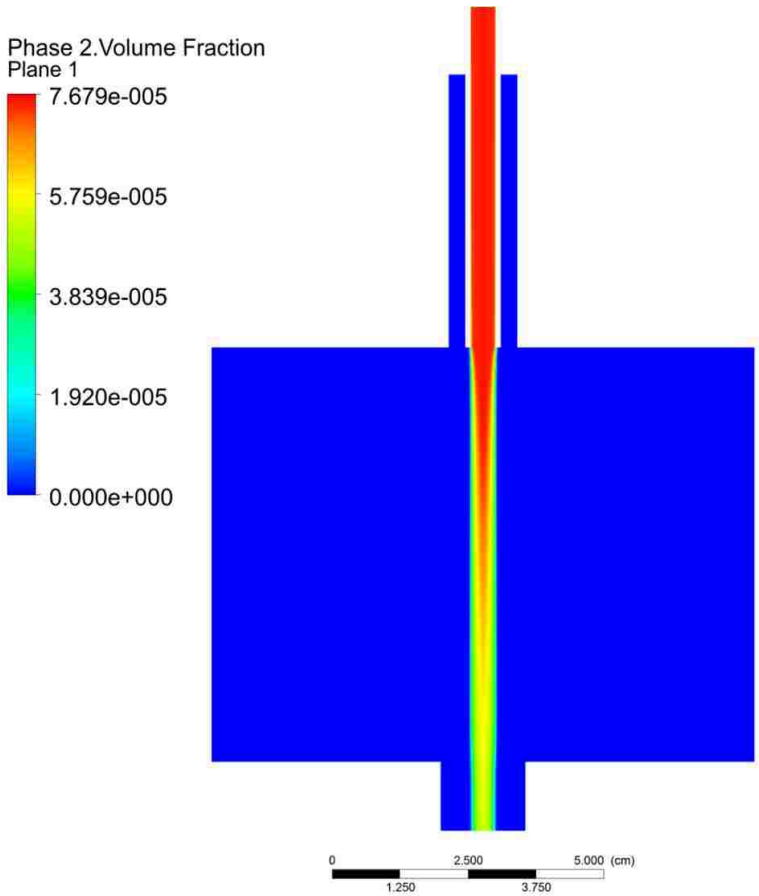

Figure 3.9: Volume fraction contours of the particulate phase.

A SHAMRC calculation was run with the new initial conditions to see what effect they would have on the RMI. To match the FLUENT results, a region of particles was created using the setmetal option in SHAMRC. This option places particles into zones containing a specific material at a mass based on a percentage of the mass in the zone. This feature is used to fill complicated geometries with particles, or to generate a group of particles that have some specific distribution of diameters. To fill the appropriate zones in the mesh with the proper amount of material a cubic spline and a linear fit were used to match the fluent results for the particle mass concentration as a function of radius depicted in Figure 3.10, similar to how the initial conditions

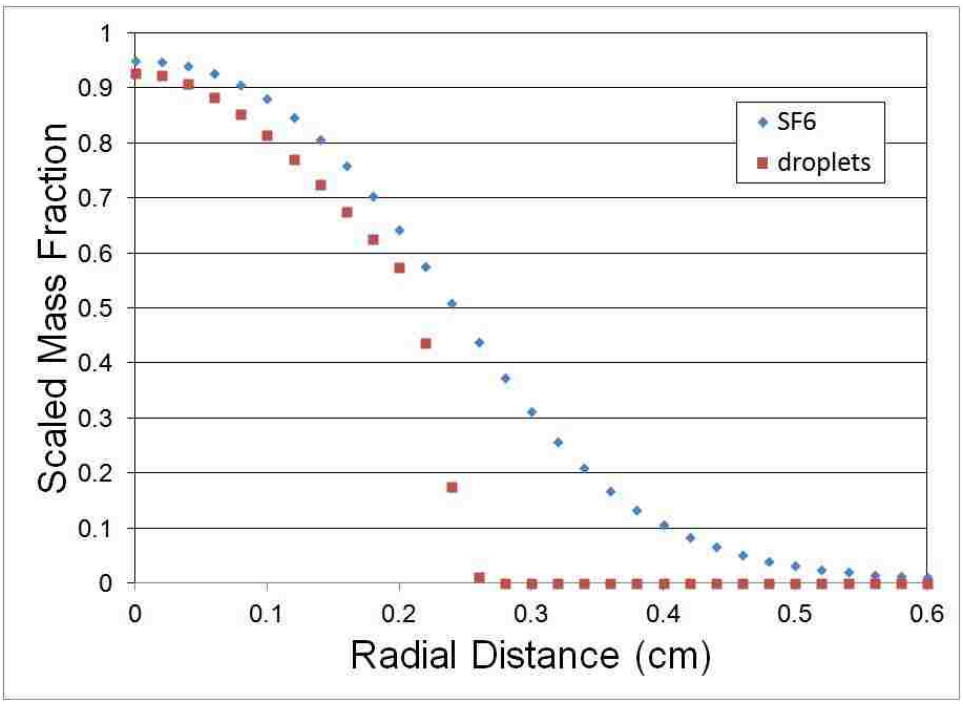

Figure 3.10: SF_6 and droplet concentration as a function of cylinder radius at the shock tube center.

for SF_6 were created. Figure 3.11 shows a compilation of the experimental images (top) and images of the particles from the SHAMRC calculation (bottom). In the SHAMRC images, the particles are colored by their diameter. As the particles have a uniform diameter of 1 μm the variations in color only indicate the position of separate particles, not differing density. The initial conditions in the SHAMRC simulation now appear to be roughly the same size as what is observed in experiments. Also, the resulting instability that is formed in the SHAMRC calculation matches well with the morphology that is observed in experiments. The vortex cores are absent of droplets and there are no secondary filaments observed. The biggest difference between the numerical and experimental results is a slight mismatch in the thickness of the instability. The instabilities produced by SHAMRC appear to be thinner than those observed in experiments at later times. This is likely due to the lack of a

distribution of sizes for the particle diameters. In the numerical simulations, all of the droplets are exactly 1 μm in diameter, while in the experiments it is probable that some of the particles are slightly smaller or larger than this size. This variation in size would have the effect of spreading the particles out slightly as they are initially accelerated due to differences in drag forces, which are highly dependent on the particle diameter. This concept will be explored in depth in Chapter 3, where the effects of particle size on instability formation are examined numerically.

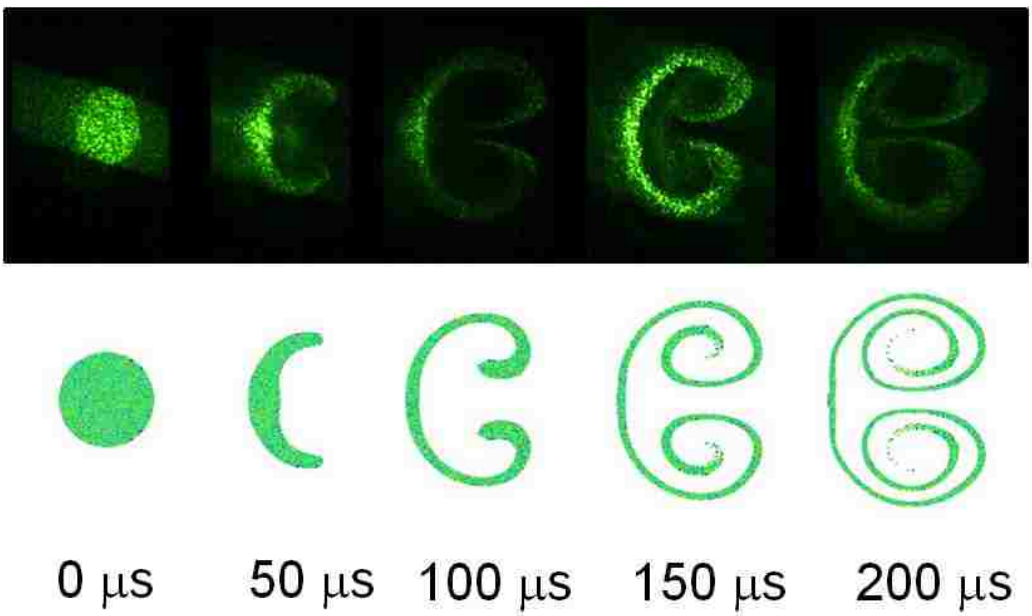

Figure 3.11: Comparison between particle images from SHAMRC (bottom) and experimental images (top) for early times.

With satisfactory comparisons of the experimental and numerical results at early times, a comparison can be made between these results at the farther the downstream position. Figure 3.12 shows the particles at a downstream distance of 16.51 cm, which is identical to the position at which the experimental image was taken. The numerical results are in good agreement with the experimental morphology as well and the instability size that is observed. One major difference is the size and thickness of plume of droplets being ejected from the center of the instability. The plume gen-

erated in the SHAMRC simulation is sparser than what is observed experimentally. One possible explanation is that the numerical particles do not exactly reproduce the motion of each physical particle in the cloud, resulting in a plume which is less dense in appearance. Another possibility is that the fog droplets are being modeled by a uniform distribution in particle diameter. It is likely that there is some small variation in the particle sizes, which would result in particles being accelerated relative to one another. This motion could result in a plume that appears fuller. Another small difference is the apparent size of the void at the center of the vortex. The numerical calculations appear to over predict the area of this region. This difference could again be explained by the lack of a particle size distribution. The effects of particle size on instability formation will be explored much more thoroughly in the next chapter, and it will be shown that the particles can have a large effect of the morphology that is observed.

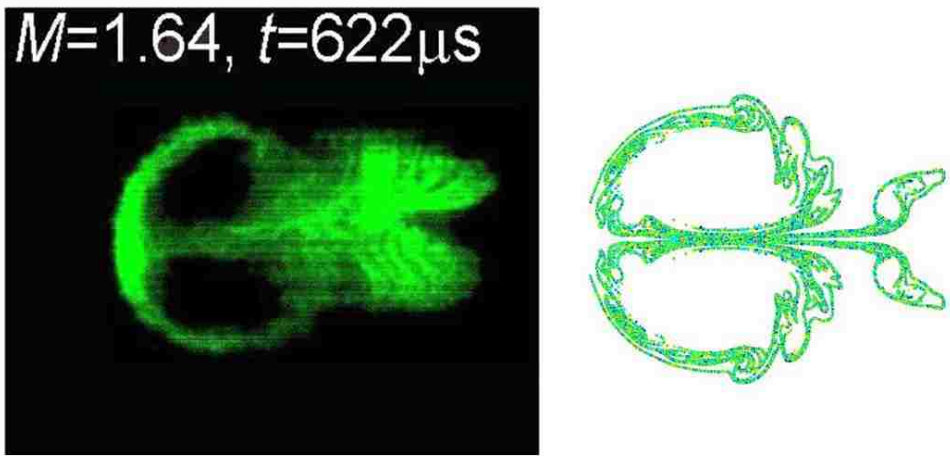

Figure 3.12: Comparison between particle images from SHAMRC (right) and experimental images (left) for late times.

3.6 Mach Number Variation

In the previous section, SHAMRC was used to successfully reproduce the experimental results for M=1.67. In this section, experimental results for M=1.2 and M=2.0 are compared to numerical results generated from the same initial conditions used to successfully reproduce the results at M=1.67. Figure 3.13 shows a comparison at early times between the experimental and numerical results for M=2.0. The instability grows at a faster rate and appears to be slightly smaller in height than the instability that is formed at M=1.67. The SHAMRC results appear to capture both of these features. Figure 3.14 shows a comparison at early times between the experimental and numerical results for M=1.2. This instability grows at a much slower rate than the instabilities formed at the higher Mach numbers. The instability is also noticeably bigger than the other instabilities. Again, SHAMRC is able to match both of these features. Finally, Figure 3.15 shows a comparison of the SHAMRC and experimental results at the downstream position of 16.51 cm. The agreement between the SHAMRC and experimental results at late times is not as good as the agreement at early times, especially for M=1.2. The small differences that are observed at early times for the low Mach numbers are amplified at late times, resulting in a morphology that is not observed in the experiments, namely the central plume of ejected droplets. Overall the morphology and size of the instabilities presents a good match to experimental data.

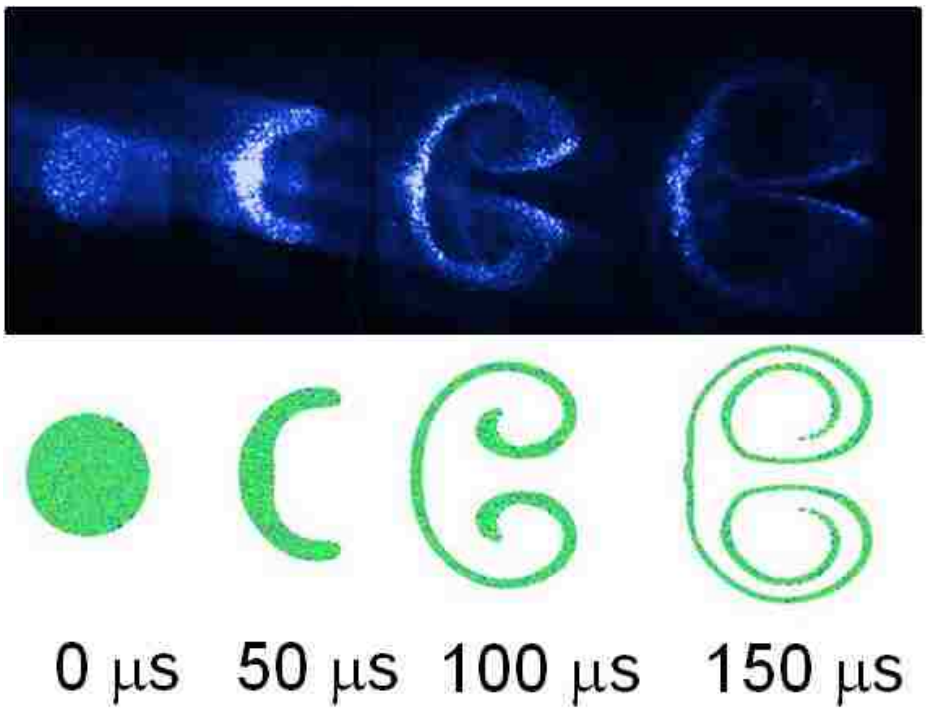

Figure 3.13: Comparison between particle images from SHAMRC (bottom) and experimental images (top) for early times at M=2.

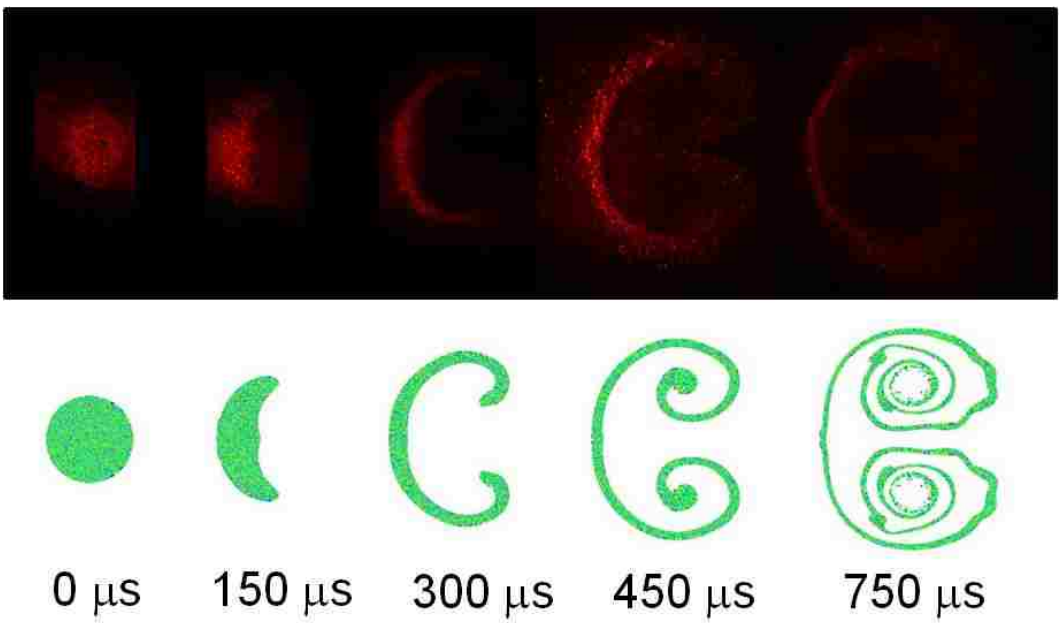

Figure 3.14: Comparison between particle images from SHAMRC (bottom) and experimental images (top) for early times at M=1.22.

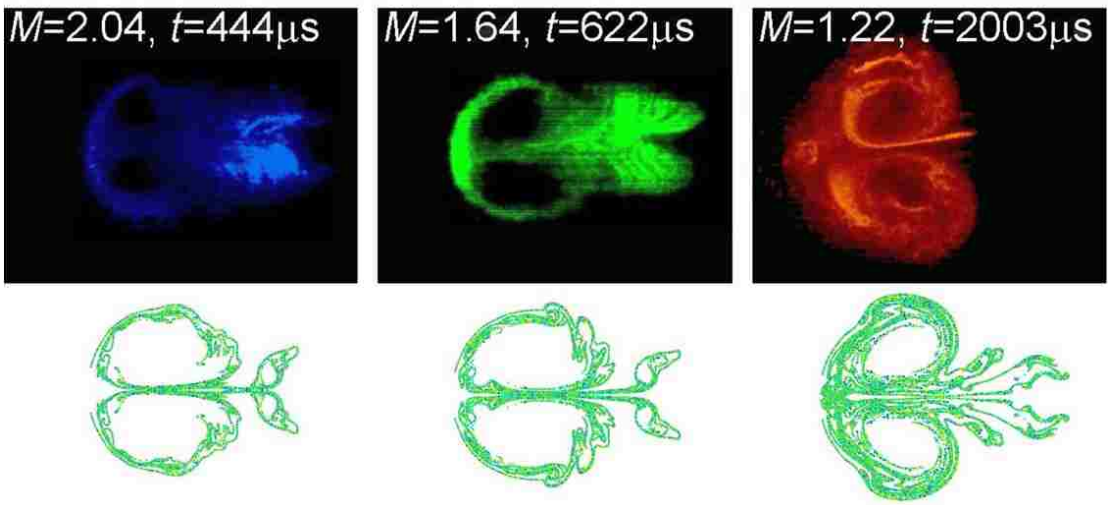

Figure 3.15: Comparison between particle images from SHAMRC (bottom) and experimental images (top) for late times at Mach number 1.22, 1.67, and 2.0.

Chapter 4

Multi-phase Fluid Instabilities

4.1 Overview

In the previous chapter the numerical and experimental results for the traditional Richtmyer-Meshkov Instability (RMI) were introduced. This instability forms due to vorticity deposition by the misalignment of pressure and density gradients across a fluid-fluid interface. Recent experimental work by Vorobieff et. al. [1] and numerical work by Ukai [4] have shown that a similar type of instability can form in multiphase flow. In this case, the morphology of the instability that forms is similar to traditional RMI, however; the mechanism behind its formation is different due to an absence of a fluid-fluid interface.

This chapter first introduces experimental data for these types of instabilities gathered at a variety of Mach numbers and downstream locations for the experimental setup described in Chapter 2. Next, two types of numerical approaches are undertaken using SHAMRC to model this instability. The first approach is to approximate the droplet phase as a fluid with a density equivalent to spreading the mass of the discrete droplets out over the region of the initial conditions. It has

already been shown in Chapter 3 that SHAMRC can successfully model traditional RMI, however; this scenario is for a significantly lower Atwood numbers than those previously considered. The second approach it to model the droplets with the particle models found in SHAMRC. These two methods will be compared against each other. Finally, a series of SHAMRC calculations are presented to demonstrate how the size of the droplets affects the instability.

4.2 Experimental Results

The experimental initial conditions consisted of a vertical column of slowly moving air seeded with glycol droplets. The vertical velocity is small in relation to the shock velocity and can be neglected in the following numerical models. The particles are accelerated by a shock wave generated as described in Chapter 2. The images in Figure 4.1 shows the evolution of the laser illuminated horizontal cross-section of this column, as it and the surrounding air are accelerated by a planar shock moving at an average velocity of about 570 m/s (Mach number M = 1.66+/-0.02, with small variations from experiment to experiment). What is visible in the images is Mie scattering off droplets in the laser-illuminated plane. The dark areas of the images correspond to droplet-free air, while brighter zones contain droplets.

The images in Figure 4.1 are a compilation of six experimental image sequences taken at various locations downstream on the initial conditions. The shock direction is from bottom to top. The timings of individual exposures are marked in the figure, with $t = 0$ corresponding to the time at which the shock wave passes through the center of the initial conditions. The shock Mach number for each exposure is also displayed in this figure. The Mach number is calculated by measuring the time between pressure peaks recorded by the pressure transducers. The numbers to the left of the image denote the distance from the center of the initial position of the

column in mm.

The initial conditions of the experiment (first image in Figure 4.1) are nearly two-dimensional, with little variation in the direction normal to the plane of view. In the early images of the sequence of Figure 4.1 (third to fifth), the smallest droplets form a line parallel to the shock front, and larger droplets trail farther upstream, forming a tail-like structure, due to smaller droplets achieve momentum equilibrium with the embedding flow faster than the larger ones. Overall, this momentum exchange leads to the air-droplet mixture mean velocity in the section of the flow containing particles being lower than that of the surrounding particle-free air. Shear between the areas with lower and higher velocities in turn leads to formation of counter-rotating vorticies on both sides of the column which are apparent in the seventh and subsequent images in Figure 4.1.

The morphology that develops at later times as the result of this shock-driven interaction is superficially similar to that of a cylinder of heavy gas initially embedded in lighter gas and accelerated by a planar shock [13], where two counter-rotating vorticies form due to RMI. However, what happens in the two cases on the microscopic scale is quite different, and there are also discernible differences in the flow morphology due to traditional RMI and to the multiphase RMI, as Figure 4.2 illustrates. This figure shows the evolution of the air-droplet and air-SF_6 instabilities at identical downstream locations for differing Mach numbers. The experimental images were illuminated with a green laser, here; false color has been added to distinguish between different Mach numbers. Blue for $M = 2.02$, green for $M = 1.67$, and red for $M = 1.22$.

With SF_6 injection, an initially cylindrical, diffuse interface forms between the heavy gas and the lighter gas (air), resulting in a density gradient being added to the initial conditions, producing RMI upon shock passage. The counter-rotating vortex pairs are evident in all the cases, however, for the case of RMI, another feature gains

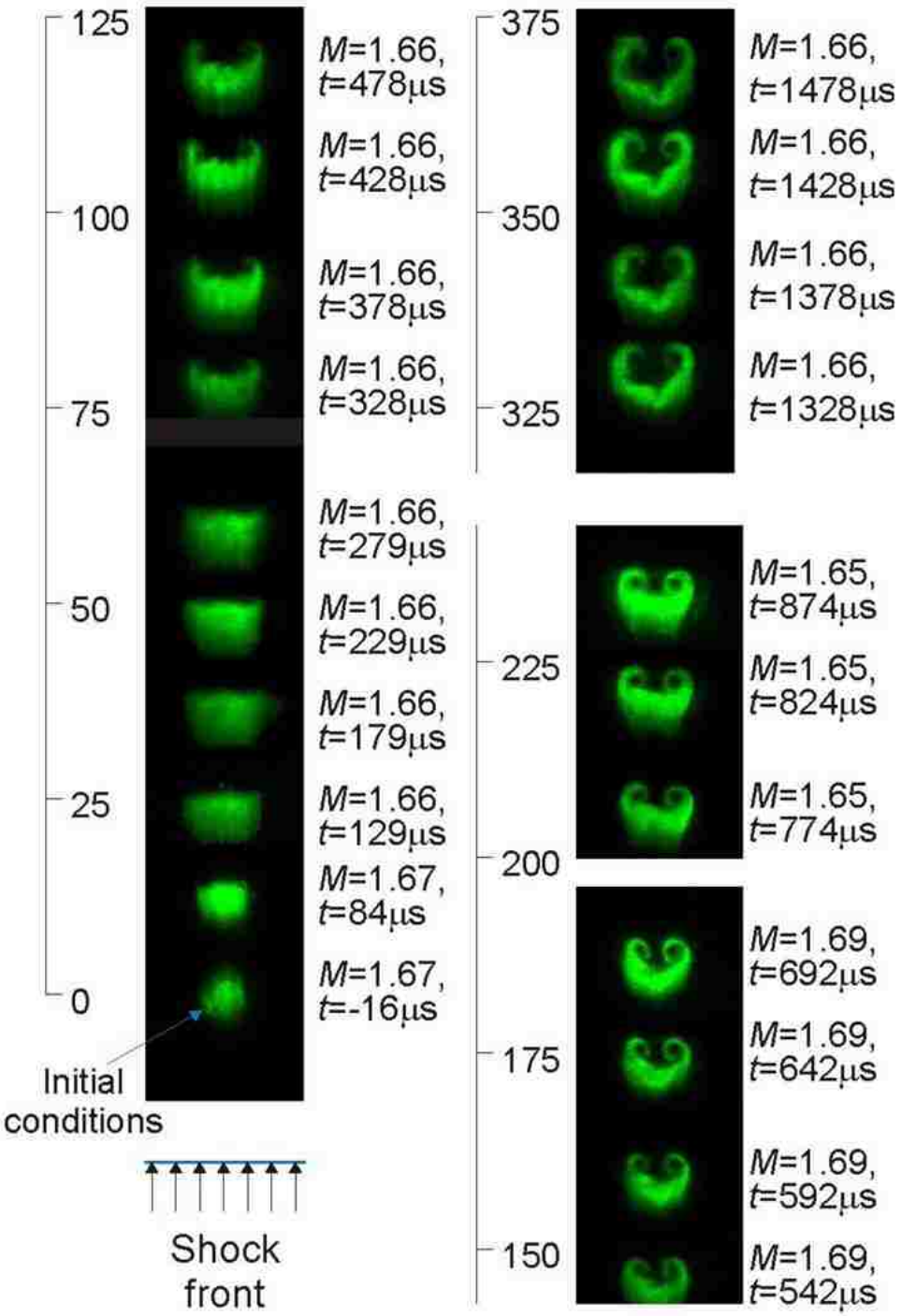

Figure 4.1: Mosaic of six experimental image sequences showing the evolution of a shock-accelerated column of glycol droplets in air [1].

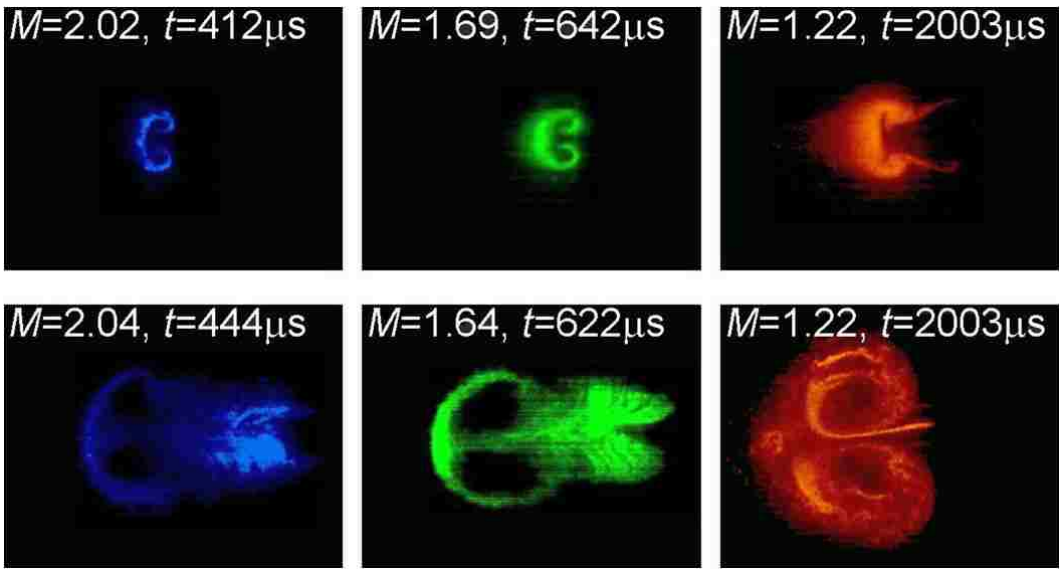

Figure 4.2: Images of the instability of a droplet-air column (top) and droplet-SF_6 column (bottom) [1].

prominence as the Mach number increases, namely a central spike that emerges due to secondary instabilities. This feature is notably absent in the images of the droplet-seeded column. The RMI images also manifest small-scale structures that form due to secondary instabilities and lead to the flow transitioning to turbulence. In the case of RMI, the flow behavior at small scales associated with these features is known to become statistically consistent with models of fully developed turbulence [34].

The small-scale structures visible in the top column of Figure 4.2 arise both due to shear (Kelvin-Helmholtz instability) and to the secondary baroclinic instability induced by pressure-density misalignment in the cores of the vorticies comprising the counter-rotating pair. Some evidence of the shear-driven secondary structures may be present in the late-time (t $>$ 1 ms) images of the droplet-column instability as well, however, even at the latest times observed, no evidence of transition to turbulence was seen. Another notable feature of 4.2 is the rather weak dependence of the apparent size of the counter-rotating vortex pairs on the Mach number.

Figure 4.3 shows the early time growth of the air-droplet instability (top) and the SF_6-droplet column (bottom). The images were taken from $M = 1.67$ shots and have a spacing of 25 *us* between frames. Of particular note is the rapid growth and formation of the RMI instability when compared with the air-droplet instability. In many earlier experiments, tracer particles or droplets were used under the assumption that they would behave as a passive scalar. These results demonstrate that such an assumption is generally not valid. However, in the presence of RMI, its much faster growth begins to dominate the flow from the time shortly after shock acceleration, as Figure 4.3 illustrates.

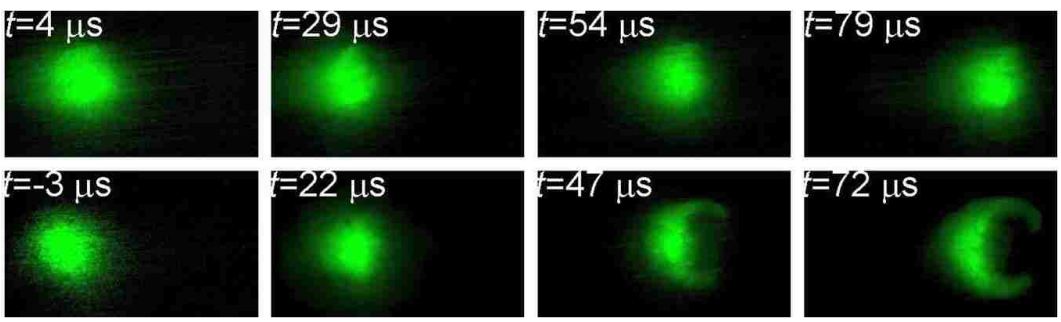

Figure 4.3: Comparisons of early-time evolution of air-droplet column (top) and SF_6-droplet column (bottom) for $M = 1.67$ [1].

4.3 Numerical Modeling

Numerical calculations to model the formation and growth of the observed instabilities were run using SHAMRC. A 2D Cartesian mesh was used with dx and dy of roughly 0.005 cm. These dx and dy were chosen so that there would be exactly 128 zones across the diameter of the IC column, which was set to the inner diameter of the injection tube used in these experiments, 0.635 cm. Note that this diameter is slightly larger than the initial conditions presented in the previous chapter. This is due to a change in the injection system to improve the quality of the initial conditions,

presented in Chapter 2. The validity of this choice for initial condition diameter was verified by examining images taken of the initial conditions during experiments. The mesh extended to the shock tube wall in the y direction, a distance of 3.81 cm. The x extent was set to 51 cm so that approximately 2 ms of instability growth could be modeled before the instability was swept from the grid. Additionally, a half plane of symmetry along the x-axis was used to reduce the total number of zones required to 9 million.

4.3.1 Modeling with a Pseudo-Glycol Fluid

The first approach used to model the initial conditions in SHAMRC was to approximate the air-glycol mixture as a perfect gas with the same average density. The perfect gas equations of state are defined as $P = (\gamma - 1)\rho I$ and $T = (PW_M)/(R\rho)$. In these equations, P is the pressure, ρ is the density, γ is the ratio of specific heats, I in the specific internal energy, T is the temperature, W_M is the molecular weight, and R is the universal gas constant. To determine the density of the pseudo-glycol fluid, a container with a known volume of the air-glycol mixture was weighed with a high accuracy scale. The result was the difference between the densities of air and the air-glycol mixture, found to be 0.06 ± 0.01 kg/m^3. The local elevation causes a 15% reduction in the standard air density of 1.225 kg/m^3. Together with the measured density differential, this yielded an Atwood number $A = (\rho_2 - \rho_1)/(\rho_2 + \rho_1)$ of approximately 0.03.

To match laboratory conditions and maintain the appropriate Atwood number, the simulations were run at an ambient density of 1.051 kg/m^3 for air and a density of 1.116 kg/m^3 for the pseudo-glycol fluid. A γ of 1.4 was chosen for the pseudo-glycol fluid to match air. The ambient energy and atomic weight were chosen to maintain pressure and temperature equilibrium between the initial conditions and ambient air.

Figure 4.4 shows side-by-side comparisons of images taken during several experiments along with images from a SHAMRC calculation with $A = 0.03$ and $M = 1.67$. The images from the calculation display the density of the pseudo-glycol fluid and have all been scaled to the same size. The scaling factor was chosen so that the images of the initial conditions are the same size for the test data and numerical results. This scaling allows the direct comparison of the sizes of the instabilities observed in experiments and those generated in the numerical simulation. The timings of the exposures are displayed below the corresponding images. with the time $t = 0$ corresponding to the time at which the shock wave reaches the center of the initial conditions.

From this image, it is clear that the morphology of the instability created in the numerical calculation is a good qualitative representation of what is observed in experiments. To quantify these results, measurements were taken from each image to determine the width of the instability as a function of time. The streamwise perturbation width is defined as the extent of the instability in the direction of the shock. Figure 4.5 illustrates the definition of the perturbation width W and height H. Figure 4.6, left shows all the test data collected along with the SHAMRC data for Mach numbers of 1.22 (red squares), 1.67 (blue diamonds), and 2.02 (green triangles) for an initial condition Atwood number of 0.03. The test data are shown as open symbols, while the SHAMRC data points are filled.

The experimental setup only allows for the collection of four data points for each shock tube run. This results in a spread in the experimental data which can be accounted for by small differences in the shape of the initial conditions and the Mach number, resulting in non-uniform vortex formation. The SHAMRC data was generated in a calculation with perfectly formed initial conditions and as such does not display this spread. In Figure 4.6, the numerical results form a lower bound for the experimental data with a slope that matches the experimental data, indicating

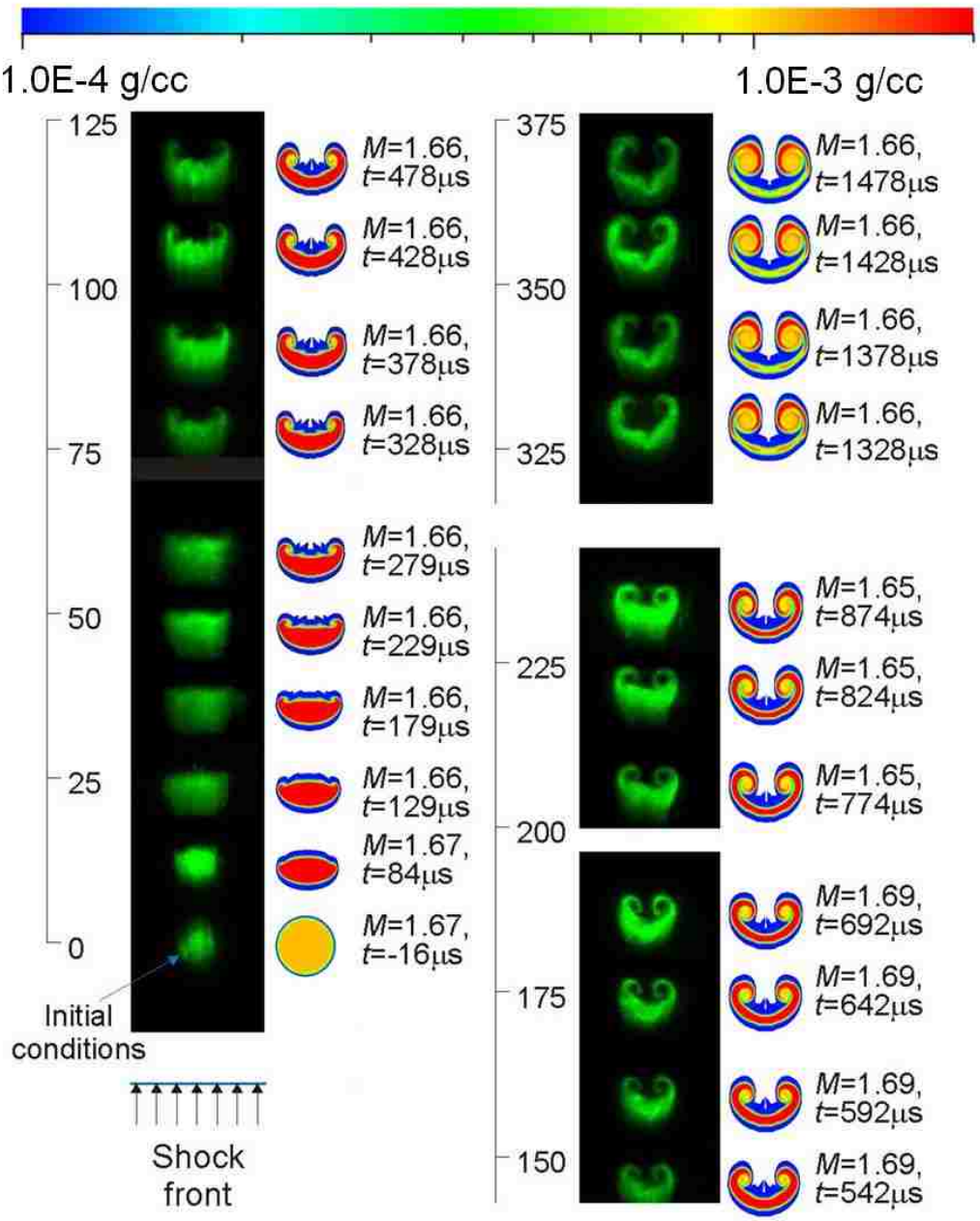

Figure 4.4: Multi-phase instability evolution. Green images - experiment (planar laser visualization), color images - numerics. Scale left of the images indicates downstream distance in mm, labels to the right indicate timings and Mach numbers.

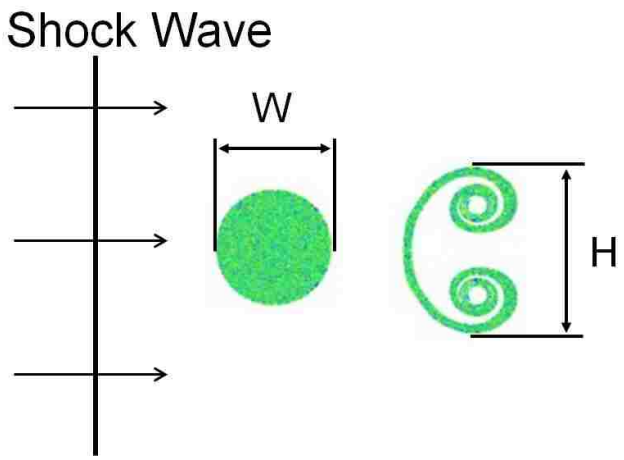

Figure 4.5: Definition of streamwise pertubation width and height.

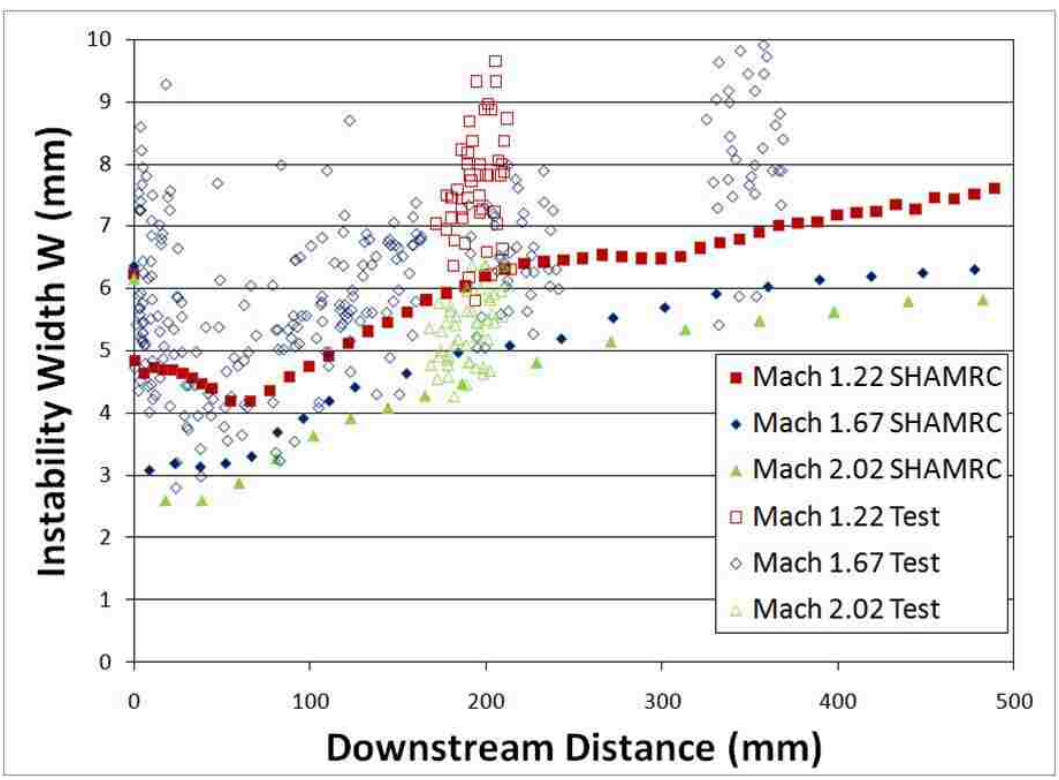

Figure 4.6: Perturbation width for SHAMRC calculations (filled) and test data (open) at various Mach numbers.

a similar growth rate. The main difference between the two data sets is the larger size of the experimental instability. This difference is nearly constant over time and is due to the assumption made to model the initial conditions as a continuous fluid instead of discrete particles. In the experiments, the larger particles get accelerated to the piston velocity more slowly than their smaller counterparts. This lag causes a spread in the initial conditions which can be seen clearly in the early images of Figure 4.1. The comparisons above demonstrate that SHAMRC can be used with the current assumptions to model the first order effects of the glycol-air initial conditions and the resulting instabilities that are formed.

4.3.2 Modeling with Discrete Particles

The geometry of this calculation and the shock initial conditions were identical to the calculation run in the previous section. The difference was that instead of creating initial conditions with the pseudo-glycol fluid, glycol droplets were used. To match the Atwood number of the previous calculation, 1.03×10^{-5} g of droplets were placed into the calculation. Sixteen computational particles were placed in each zone inside the initial condition cylinder for a total of 102,992 particles. Each computational particle represents a cloud of physical particles with a combined mass of 1.0×10^{-10} g. For this calculation a uniform particle distribution of 1.0 microns in diameter was used. The density of glycol is 1036 kg/m^3, so a physical droplet with this radius has a mass of 5.4245×10^{-16} kg and each computational particle represents 184,349 physical particles. SHAMRC does not model particle-particle interactions, however, the seeding density of the particles is small enough that these types of interactions happen very infrequently and do not need to be modeled.

Figure 4.7 is a comparison of the experimental (left column) and numerical (right column) images presented in Figure 4.4 with corresponding images from the particle

simulation (center column). The images are again scaled so that the initial conditions are the same size as the test data. These images are placed in between the images from the test data and previous modeling effort with a pseudo-glycol fluid. It is clear from looking at the images that both methodologies yield instability morphologies that are similar to those seen in experiments. A feature that both methods fail to resolve is the tail of trailing particles that is observed in experiments. It was expected that this feature would be absent when modeling the instability with a pseudo-glycol fluid, however; it should be possible to reproduce this feature with the particle approach. The likely culprit is the use of a mono-disperse particle size. With the current setup, all particles will be accelerated at the same rate across a plane parallel to the shock front. The only difference will appear in a plane perpendicular to the shock where particles on the edge of the initial conditions are subjected to a shear that causes the instability to form. If some of the particles are subjected to a slightly different drag force a tail will likely appear.

The preceding shows that SHAMRC can successfully reproduce the instability with a discrete particle model. The investigation can now be turned to how the size of the particles affects this instability. Calculations were run with a mono-disperse particle size distribution of 0.5, 0.7, 1.0, 3.0, 5.0, 10.0 and 25.0 microns in diameter. Figure 4.8 shows images from each calculation at 250, 500, 1000, and 1500 micro-seconds. The images are order from left to right by diameter and top to bottom by time. Figure 4.8 demonstrates how changing the diameter of the particles in the initial conditions affects the instability that is formed. In the case of the 3.0 micron particles, the edges of the instability have only just begun to turn back in on themselves at 1500 micro-seconds while the instabilities formed by smaller particles have rolled up several times. From the figure, it can be seen that increasing the size of the particles effectively decreases the intensity of the vortex pairs that are formed. Again looking at the 3.0 micron particles, the size of the instability is larger than those formed by those with smaller particles. The vortex pairs formed by increasingly

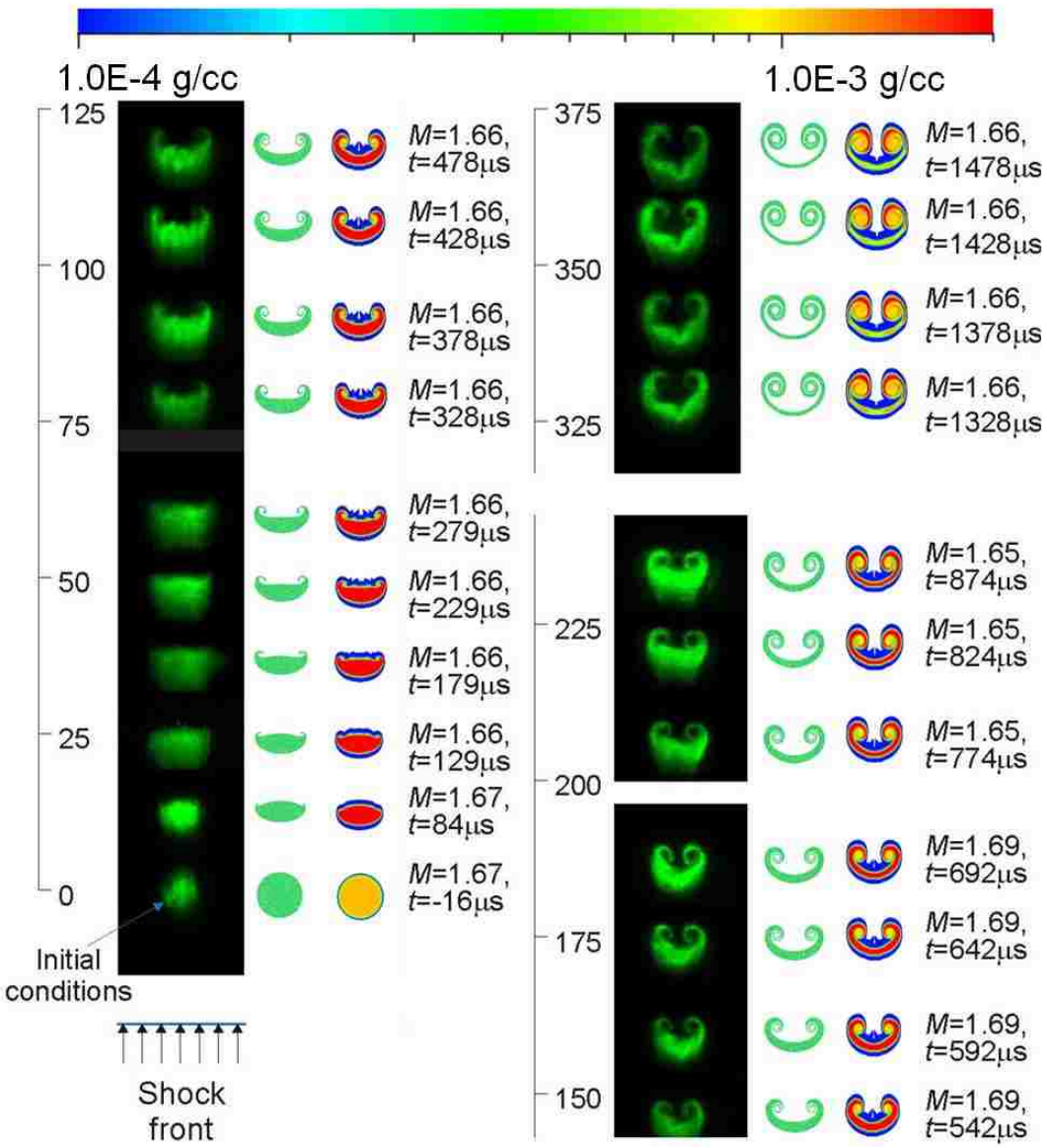

Figure 4.7: Instability Evolution. Green images - experiment (planar laser visualization), color images - numerics. Scale left of the images indicates downstream distance in mm, labels to the right are timings and Mach numbers of experimental images.

larger particle sizes are bigger in size and slower to develop than those formed by smaller particles. Figure 4.9 shows the instability perturbation widths measured for each particle size. All particles sizes undergo an initial period of compression during which the particles are accelerated to piston velocity behind the shock. This is followed by a period of linear growth during which the instability begins to form. Both of these periods increase in length with increasing particle size. The final stage is a period of non-linear growth similar to what is displayed by traditional RMI.

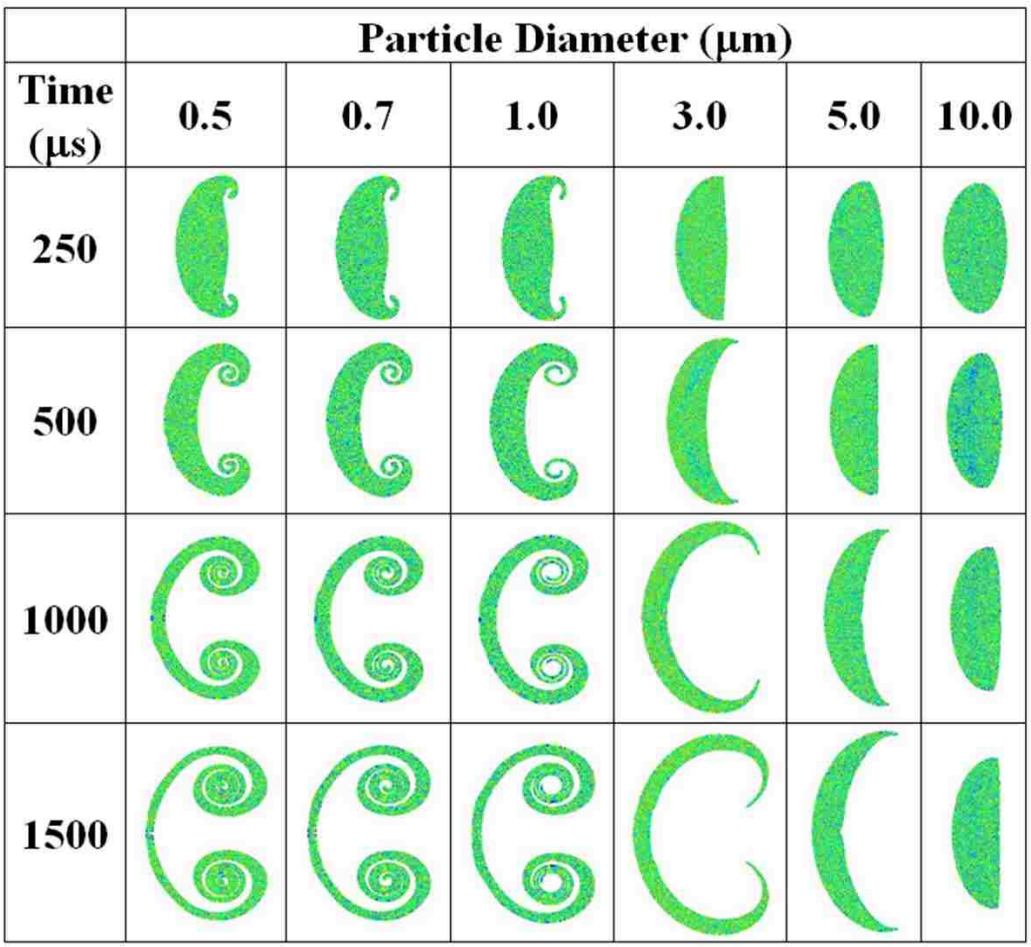

Figure 4.8: Instabilities that are formed by mono-disperse particle distributions ranging from 0.5 microns to 10 microns in diameter.

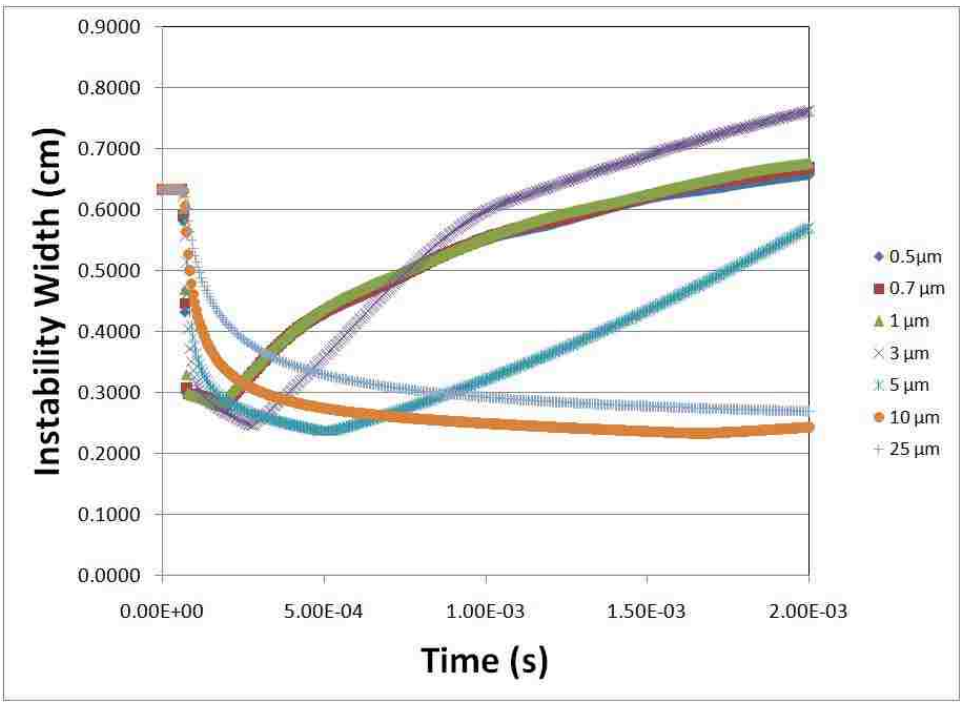

Figure 4.9: Perturbation widths for instabilities that are formed by mono-disperse particle distributions ranging from 0.5 microns to 25 microns in diameter.

The effects of a differing uniform particle size have been studied, but not the effect of a non-constant particle distribution. Figure 4.10 shows three particle distributions that have been chosen for this study. The shape of the distributions are normal in log space and are centered about a particle diameter of 3.0 microns. The form of the Probability Density Function for a log-normal distribution is shown in Equation 4.1. In this equation, F is the probability of a diameter x, σ is the standard variation, and μ is the mean. To vary the distributions, different values were chosen for the standard deviation while the mean was held constant at 3 microns. The three distributions shown in Figure 4.10 represent a standard deviation of 0.2 (distribution 1), 0.5 (distribution 2), and 1.0 (distribution 3) microns.

$$F(x:\mu,\sigma) = \frac{1}{x\sigma\sqrt{2\pi}} \exp\left(\frac{-(\ln x - \mu)^2}{2\sigma^2}\right) \tag{4.1}$$

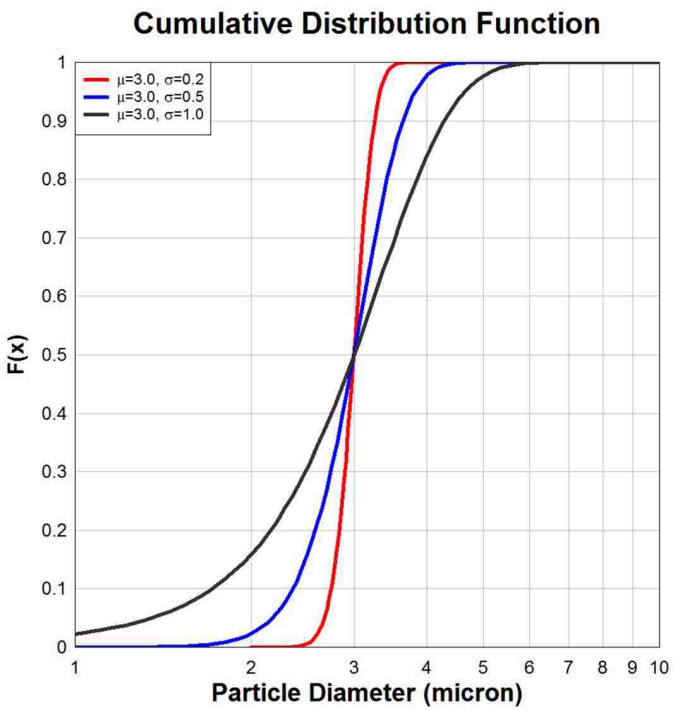

Figure 4.10: Particle distributions for SHAMRC calculations. Distribution 1 is shown in red, distribution 2 is shown in blue, and distribution 3 is shown in black.

Figure 4.11 shows images from each calculation at 250, 500, 1000, and 1500 μs. The images are ordered so that the width of the particle distribution increases from left to right. With a distribution of particle sizes, the instability forms a tail of the largest particles. This tail is formed due to a delay of the acceleration of large particles. A distribution that has a higher standard deviation or is "wider" generates a larger tail. Figure 4.12 shows the instability widths measured for each particle distribution. The wider distributions create a tail of particles that is larger than the width of the instability. This tail masks the growth of the instability and causes the instability width to remain fairly constant. For a distribution with a smaller

standard deviation, the tail essential shifts the instability width curve by a small constant.

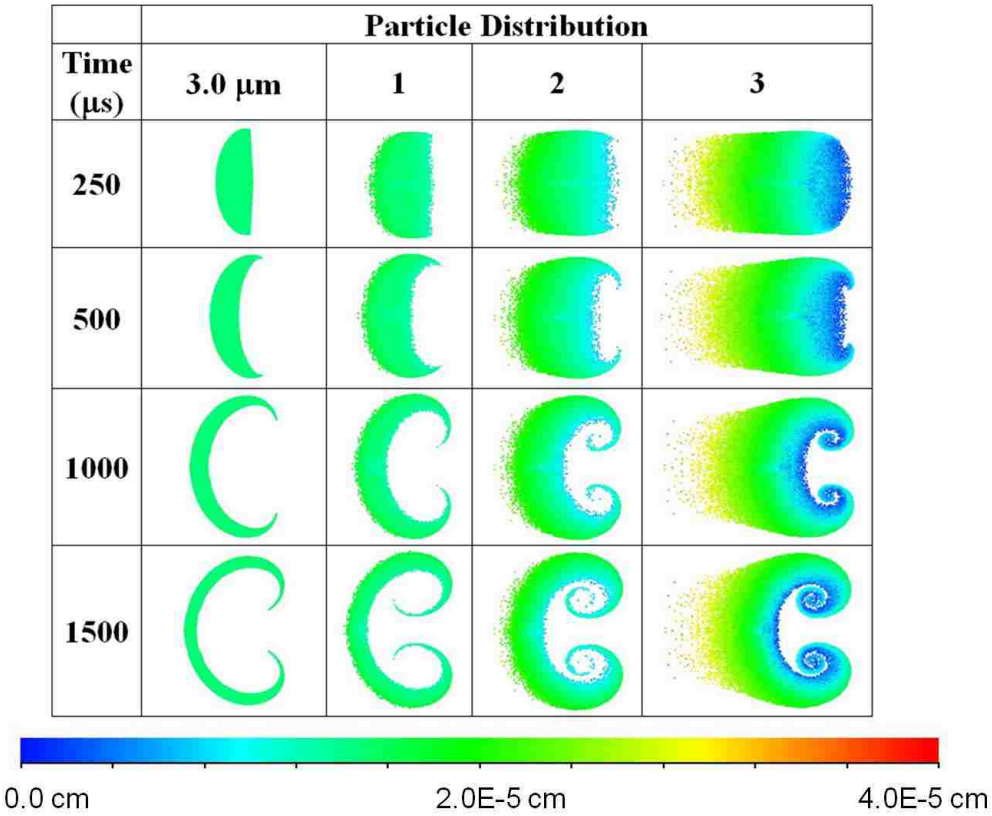

Figure 4.11: Instabilities that are formed by non-uniform particle distributions shown in Figure 4.10.

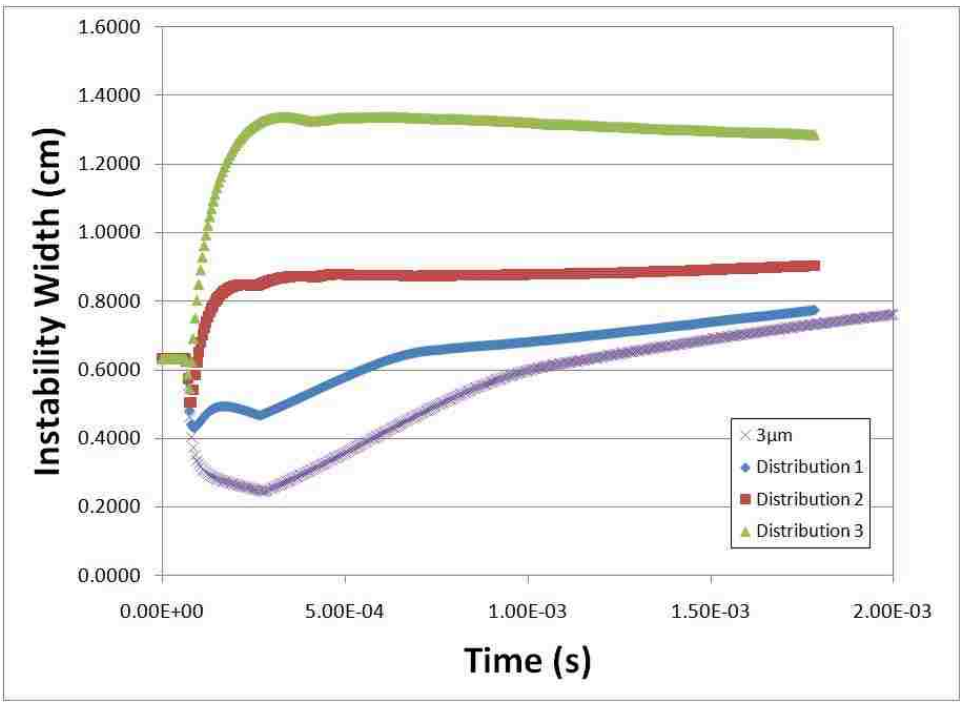

Figure 4.12: Perturbation widths for instabilities that are formed by non-uniform particle distributions shown in Figure 4.10.

Chapter 5

The Effects of Atwood and Mach Number Variation on Classical RMI

5.1 Overview

In chapter 3 the traditional Richtmyer-Meshkov Instability (RMI) was introduced. Experimental results were presented and it was shown that the numerical code SHAMRC could be used duplicate the morphologies seen in laboratory experiments once the initial conditions were properly characterized. With this baseline established, SHAMRC can be used to explore the parameter space surrounding the experimental results. The results of a numerical parameter study for Atwood numbers ranging from 0.1 to 0.5 will be presented in the following sections. The effects of Atwood number on the instability growth rate and the convective velocities of the vortex cores will be examined.

Also presented in this chapter is a numerical parameter study on the effects of

varying the shock Mach number of the growth rate. In principle, it is easy to vary the shock Mach number by simply adjusting the pressure in the shock tube driver section, however, difficulties still exist. Small variations in pressure at low Mach numbers can result in large variations in the Mach number and the high material velocities of the post shock gases at high Mach numbers can make image acquisition difficult. As such, SHAMRC simulations at Mach numbers 1.2, 1.4, 1.7, 2.0, and 2.5 were performed. The effects of Mach number on the instability growth rate will be examined in the second section.

5.2 Atwood Number Variation

The initial conditions that were used for this study were identical in shape to the initial conditions derived from FLUENT results in chapter 3. To reduce the Atwood number, the density of the gas used to represent SF_6 was varied. Table 5.1 gives the material properties used for each Atwood number. The ratio of specific heats, or γ, was held constant at 1.4. The total particle mass in each calculation was also adjusted relative to the fluid density to keep the ratio between fluid and particle masses the same as what is seen in experiments. These initial conditions may not correspond exactly to reproducible experimental conditions, but they will provide a means of comparing the effects of increasing the Atwood number on RMI formation and growth.

The results of the SHAMRC calculations are shown as density contours in Figure 5.1 and particles plots in Figure 5.2. The images are taken from a series of times ranging from 50 μs to 500 μs after acceleration by the shock wave. In both figures the Atwood number increases from left to right and time increases from top to bottom. These figures qualitatively display the effects of increasing the Atwood number on the instability growth. As the Atwood number increases, the density gradient between

Table 5.1: Material Properties for SHAMRC Equation of State

Atwood Number	Density ($\frac{g}{cm^3}$)	Energy ($\frac{ergs}{g}$)	Molecular Mass ($\frac{g}{mol}$)
0.1	1.497×10^{-3}	1.69175×10^{9}	35.37
0.2	1.838×10^{-3}	1.37788×10^{9}	43.43
0.3	2.275×10^{-3}	1.11321×10^{9}	53.75
0.4	2.858×10^{-3}	8.86127×10^{8}	67.53
0.5	3.675×10^{-3}	6.89123×10^{8}	86.83

the initial conditions and the ambient air is higher. This increased density gradient leads to an larger amount of vorticity being deposited by the passing shock wave due to the baroclinic vorticity term in the vorticity equation, which takes the form shown in Equation 5.1.

$$\frac{D\omega}{Dt} = \frac{1}{\rho^2}\nabla\rho \times \nabla p \tag{5.1}$$

The evolution of the instability can be broken into three distinct regimes. The first is a linear growth region predicted by the linear theory of Richtmyer. In this region, the instability has a shape similar to the images in the upper-left region of Figures 5.1 and 5.2. This period of linear growth lasts approximately 50 μs after shock compression for an Atwood number of 0.5 and up to 200 μs for an Atwood number of 0.1. The end of the first region is marked by the initial formation of two counter-rotating vortex cores. The second regime is that of nonlinear growth characterized by the formation and growth the vortex cores. During this period, the increase in size of the instability slows while material is wrapped into the vortex cores. The end of this regime is marked by the formation of secondary instabilities, either due to shear at the exterior of the instability (Kelvin-Helmholtz) or due to baroclinic instabilities at the vortex core. This regime corresponds to a band stretching from the lower left to the upper right of Figures 5.1 and 5.2. It spans times of approximately

50 to 350 μs after shock compression for an Atwood number of 0.5 and from 200 μs to times greater than 1.5 ms for an Atwood number of 0.1. The third and final regime is that of rapid nonlinear growth. During this phase, the secondary instabilities that developed in the second phase become stronger and more intense, leading to eventual breakdown of the vortex core and the formation of a plume of material that is ejected downstream of the instability. It is during this period that transition to turbulence may occur. In this stage, the instability takes on the appearance of the images in the lower right-hand corner of Figures 5.1 and 5.2. This also corresponds to the late-time experimental and numerical images from Chapter 3.

Figure 5.3 provides a quantitative look at the streamwise perturbation width as a function of time for increasing Atwood number. The perturbation width is defined as the distance from the upstream edge to the downstream edge in the direction of travel. Here, the particles occupy the regions of highest density and therefore, the extents of the particle cloud will be used to define the perturbation width. Distinctly visible in this figure are the three regimes outlined above. Also shown is the initial compression of the instability by the passing shock wave that occurs before the linear growth phase. As the Atwood number is increased, the vorticity deposited by the shock increases due to the increased density gradient. This causes the counter-rotating vortex pair to form more quickly and grow at an increased rate.

A non-dimensional time τ can be developed from the linear growth rate analysis of Richtmyer and is shown as Equation 5.2.

$$\tau = kA\Delta V(t - t_0) \tag{5.2}$$

Here, A is the Atwood number, ΔV is the piston velocity or material velocity behind the shock wave. The variable k is the wavenumber defined as $k = \frac{2\pi}{\lambda}$, where λ is the perturbation wavelength, which is set to the initial instability width (for the particles), 0.4983. The variables t and t_0 correspond to the current time and

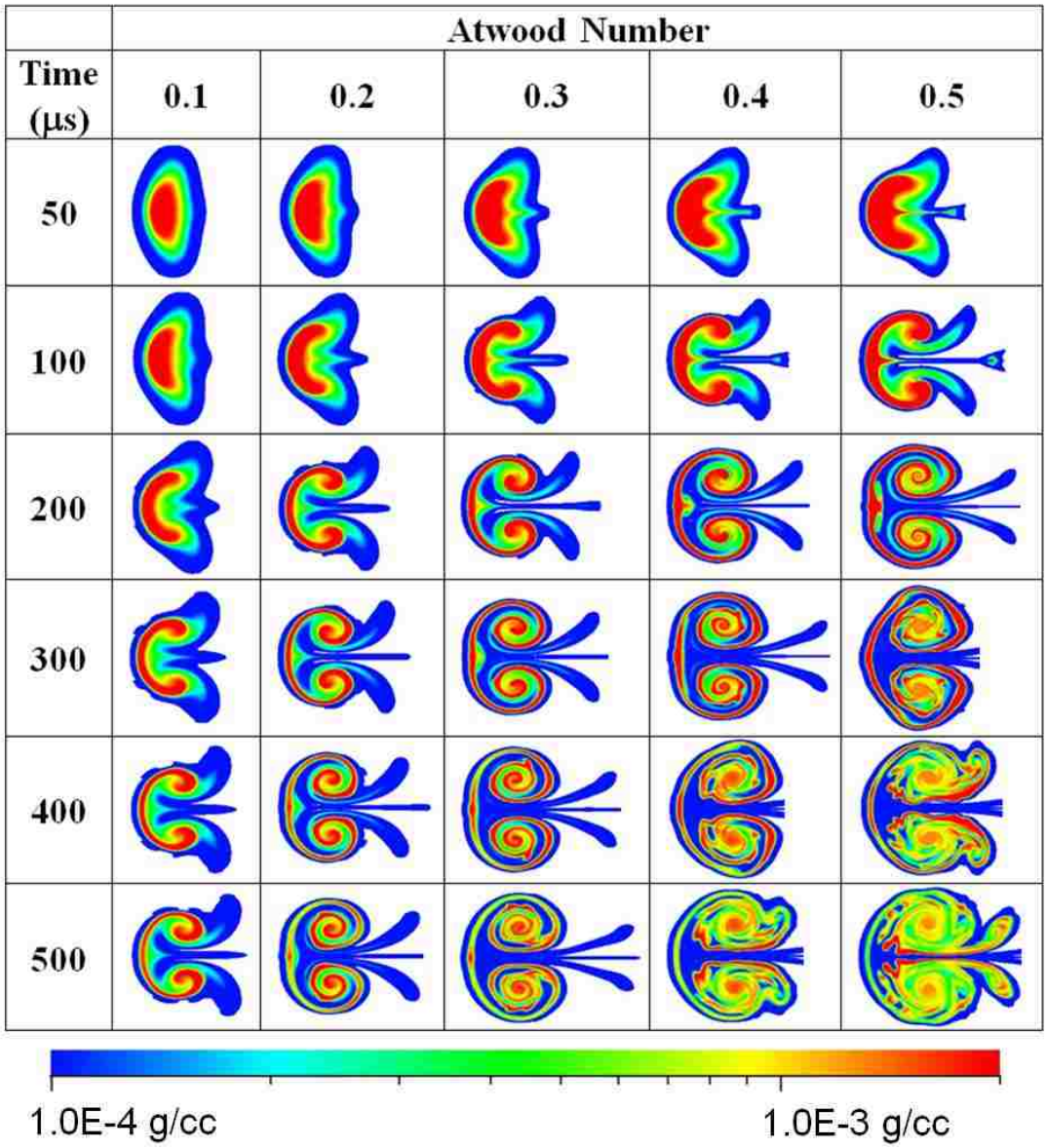

Figure 5.1: Density contours from SHAMRC calculations for increasing Atwood number.

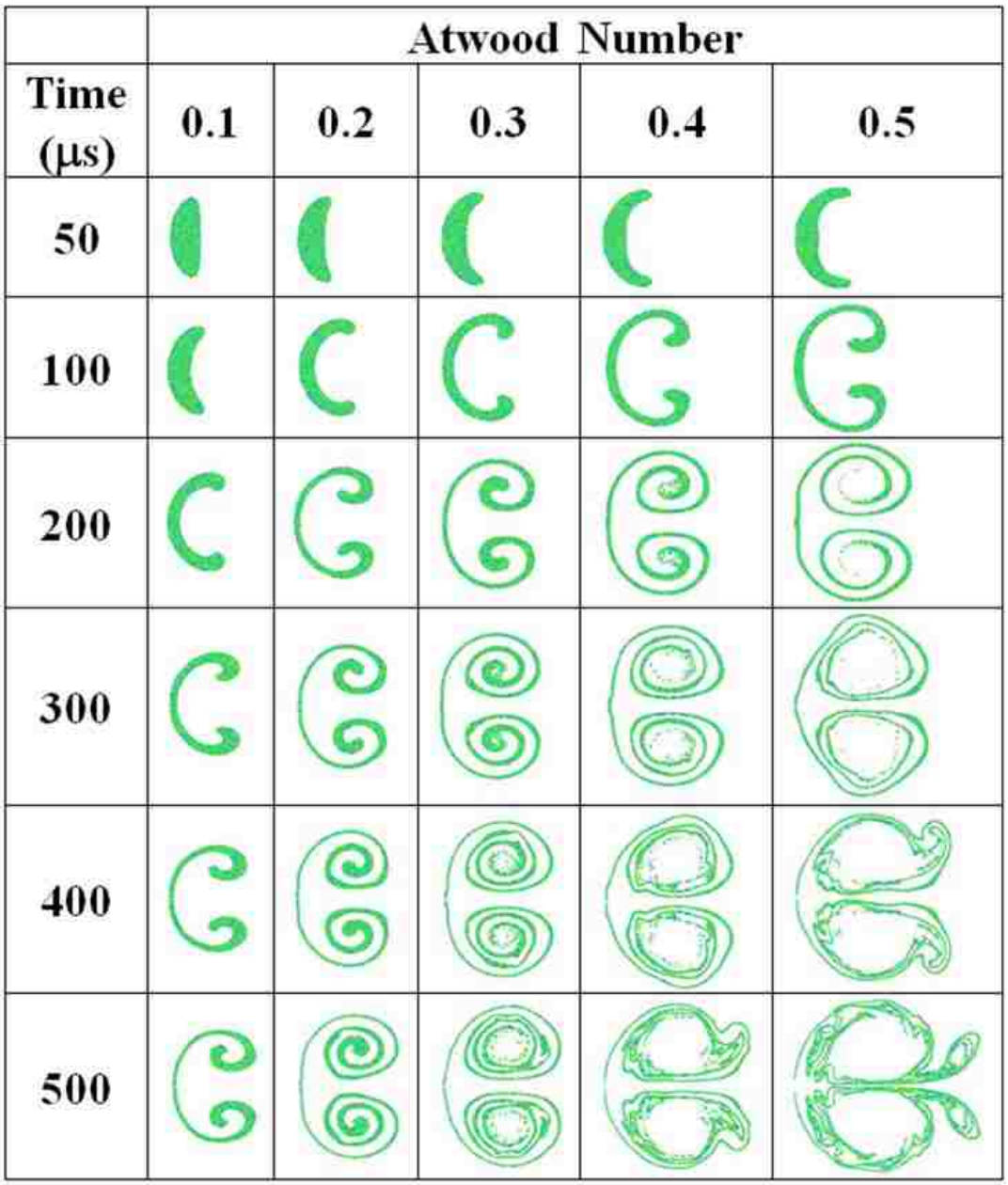

Figure 5.2: Particle plots from SHAMRC calculations for increasing Atwood number.

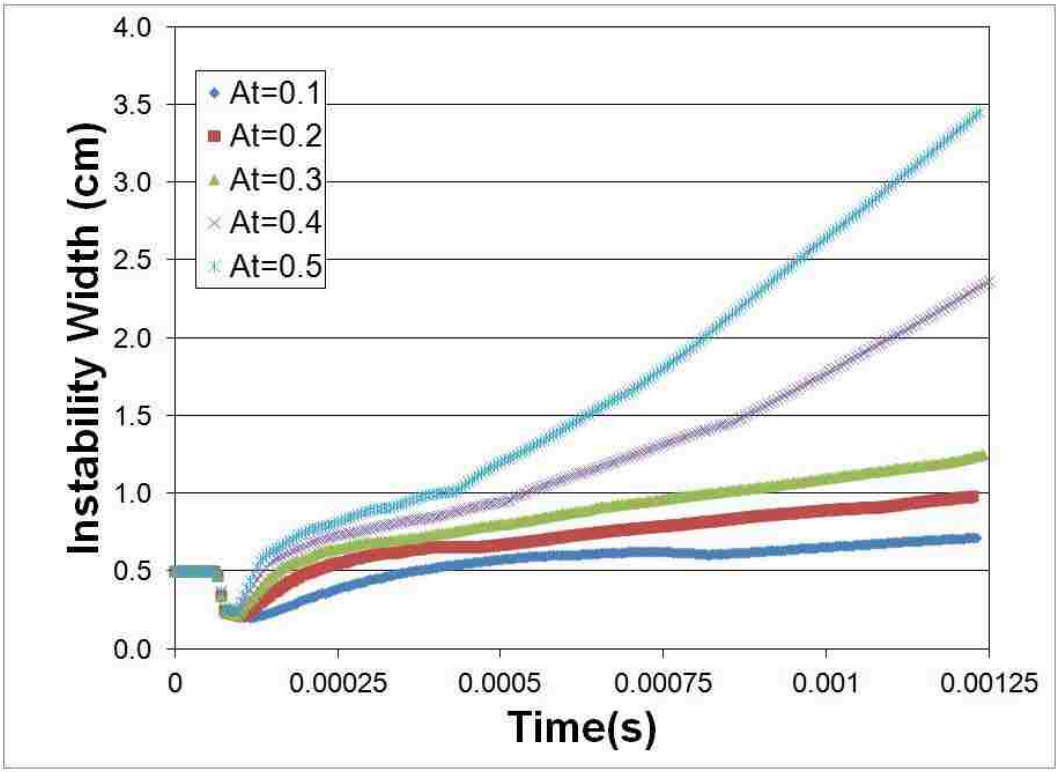

Figure 5.3: Perturbation width as a function of time for multiple Atwood numbers.

initial time, which is measured as the time of maximum compression of the initial conditions. To scale the instability width, a non-dimensional scaling parameter σ is introduced as $\sigma = \frac{w}{w_0}$ where w is the streamwise perturbation width and w_0 is the minimum perturbation width. The values chosen for w_0 and t_0 are shown in Table 5.2 and were calculated from SHAMRC results. The resulting scaling is shown in Figure 5.4 and demonstrates that for the first and second regimes the growth rate for this instability can be collapsed to a single curve for multiple Atwood numbers. The failure of the scaling method to collapse the third phase of instability growth is not surprising, as during this phase the linear growth rate developed by Richtmyer is no longer appropriate due to the formation of secondary instabilities and breakdown of the vortex core.

Table 5.2: Initial times and instability widths.

Atwood Number	t_0 (s)	w_0 (cm)
0.1	1.2×10^{-3}	0.2037
0.2	1.0×10^{-3}	0.2095
0.3	9.5×10^{-5}	0.2205
0.4	9.0×10^{-5}	0.2360
0.5	8.0×10^{-5}	0.2516

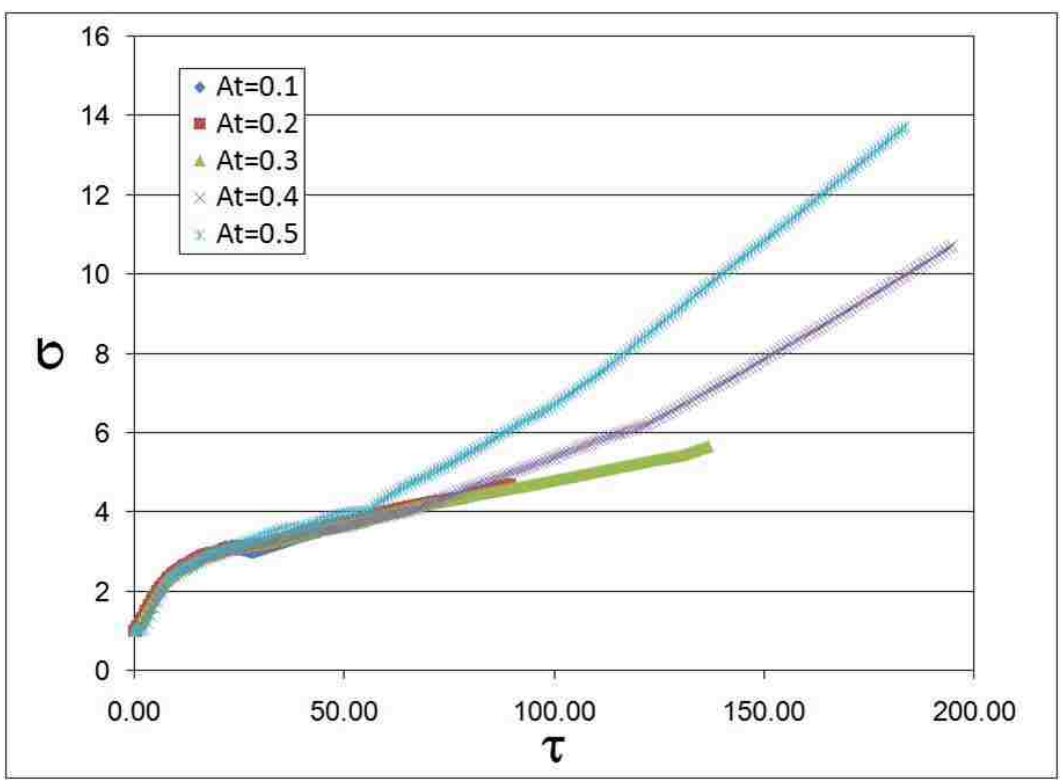

Figure 5.4: Scaled instability size as a function of scaled time for multiple Atwood numbers.

Jacobs et. al. [18] introduced a model for instability growth in dual-interface studies. Rightley et. al. [19] extended the model to be a single parameter fit based on the circulation and applied it to experiments involving a gas curtain of SF_6. The model approximates the instability as an infinite row of counter-rotating point vorticies with the same magnitude of circulation Γ. The basic form on the is given in Equation 5.3 with k, t_0, and w_0 defined as before.

$$w(t) = \frac{2}{k} \sinh^{-1} \left[k^2 \Gamma \left(t - t_0 \right) + \sinh \left(\frac{k w_0}{2} \right) \right] \tag{5.3}$$

The value of Γ was adjusted for each Atwood number to generate the best fit to SHAMRC data. The results are shown in Figure 5.5 and the values chosen for Γ for each Atwood number are shown in Table 5.3. Equation 5.3 is a good fit to the SHAMRC results for times before the appearance of secondary instabilities. These times are marked by an increase of the growth rate of the instability and are listed for reference in Table 5.3.

Table 5.3: Circulation used to generate the best Jacobs fits to SHAMRC data

Atwood Number	Γ $(\frac{cm^2}{s})$	Onset of Secondary Instabilities (s)
0.1	250	1.0×10^{-3}
0.2	600	5.0×10^{-4}
0.3	1050	4.0×10^{-4}
0.4	1900	3.0×10^{-4}
0.5	3500	2.75×10^{-4}

In addition to increasing the growth rate of the instability, it was noted that increasing the Atwood number also had the effect of decreasing the velocity at which the instability propagates downstream. A similar concept was theorized by Rudinger [15] and observed by Jacobs [18]. Rudinger theorized that the instability would have

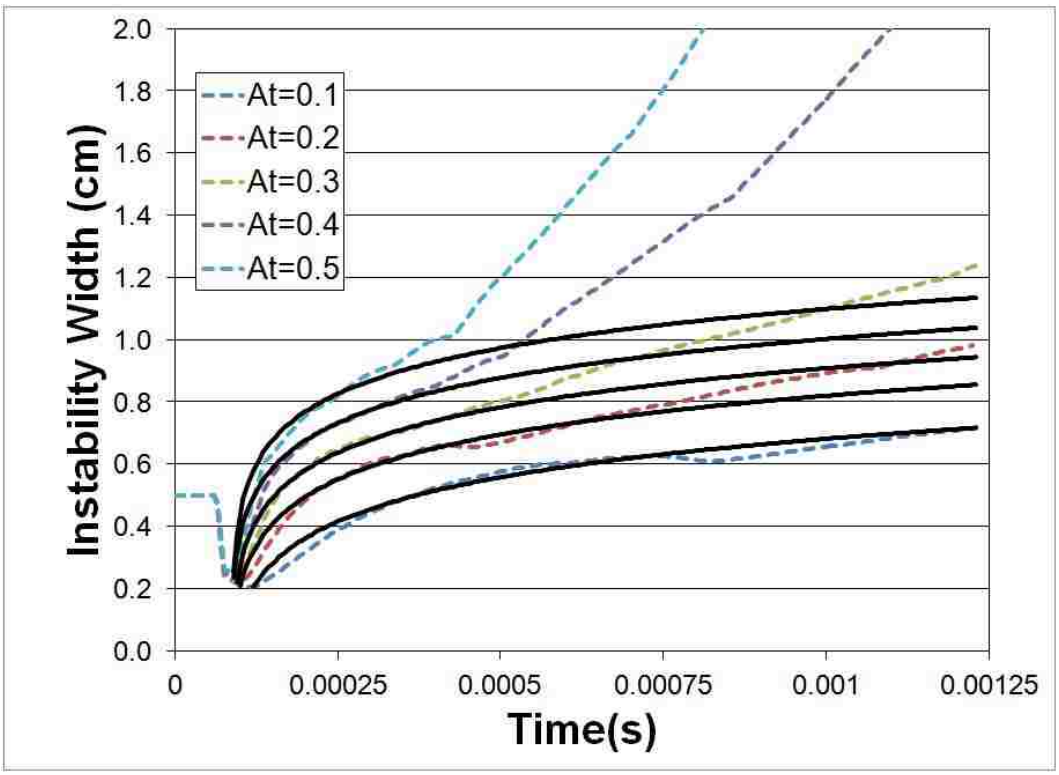

Figure 5.5: Fits to SHAMRC data based on the Jacobs scaling (drawn as solid black lines).

a velocity equivalent to that of a pair of counter-rotating vortex pairs. He found that the relative velocity of the vortex pair could be defined as $U_{vp} = \frac{2}{\pi^2} AV$, where A is the Atwood number and V is the post-shock velocity. Jacobs applied this theory to his experimental results and found this theory to under-predict the actual instability velocity at late times for a cylinder of SF_6. Figure 5.6 shows Rudinger's theory as well as the calculated average instability velocity from the SHAMRC calculations for varying Atwood number. The figure also shows the result of a proposed modification to the linear fit. The original model has been modified so that $U_{vp} = \frac{3}{2\pi^2} AV$ and provides a good match to the SHAMRC results.

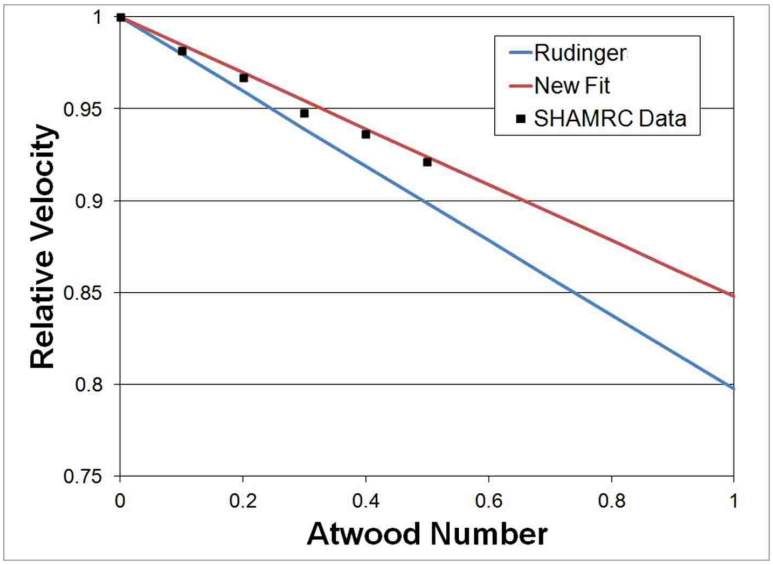

Figure 5.6: Instability velocity relative to the shock piston velocity.

5.3 Mach Number Variation

To study the effects of changing the Mach number, calculations were run with the same initial conditions as for the Atwood number parameter study with an Atwood number of 0.5, but with varying Mach number. In addition to the calculation previously presented in the previous section at M=1.7, calculations were run at M=1.2, M=1.4, M=2.0, and M=2.5. A summary of the initial conditions used to generate the different Mach numbers in air is given in Table 5.4.

In the previous section, the SHAMRC results were plotted at similar times, which correlated roughly to the same downstream position. It was shown at the end of the section that there was some discrepancy due to different instability convective velocities caused by the varying Atwood number. For the Mach number study, there is a wide range of convective velocities expected due to the wide range of Mach numbers and piston velocities considered. To examine the effect of changing the Mach number, SHAMRC images are instead considered at identical downstream

Table 5.4: Material properties for SHAMRC air equation of state

Mach Number	Piston Velocity ($\frac{cm}{s}$)	Energy ($\frac{ergs}{g}$)	Density $\frac{g}{cm^3}$)
1.2	1.0397×10^4	2.30861×10^9	1.643×10^{-3}
1.4	1.9443×10^4	2.57055×10^9	2.070×10^{-3}
1.7	3.1524×10^4	2.99155×10^9	2.692×10^{-3}
2.0	4.2531×10^4	3.46533×10^9	3.267×10^{-3}
2.5	5.9545×10^4	4.39566×10^9	4.083×10^{-3}

locations. These results are shown as density contours in Figure 5.7 and particle plots in Figure 5.8 The images are produced at 1.0, 3.0, 6.0, 9.0, 12.0, and 15.0 cm downstream of the initial conditions.

There are a few trends that are observable from these images. First, as the Mach number increases, the perturbation width of the instability increases while the perturbation height of the instability deceases at similar downstream locations. This feature was also observed experimentally and reported in Chapter 3. This result indicates that the instabilities have an increased vorticity for higher Mach numbers. This arises from a stronger pressure gradient due to the higher Mach number. Second, in Figure 5.7, the images at 1.0 cm downstream exhibit a spike of material that forms on the downstream side of the instability due to shock focusing. This spike increases in size for increasing Mach number. Third, in Figure 5.8, the rate at which the particles are entrained into the vortex core is accelerated with higher Mach number. This is again due to the greater vorticity deposition at higher Mach numbers and reconfirms the first observation. Finally, in both figures, secondary instabilities appear sooner at higher Mach numbers.

Figure 5.9 provides a quantitative look at the streamwise perturbation widths as a function of time for increasing Mach number. These results are similar to the results

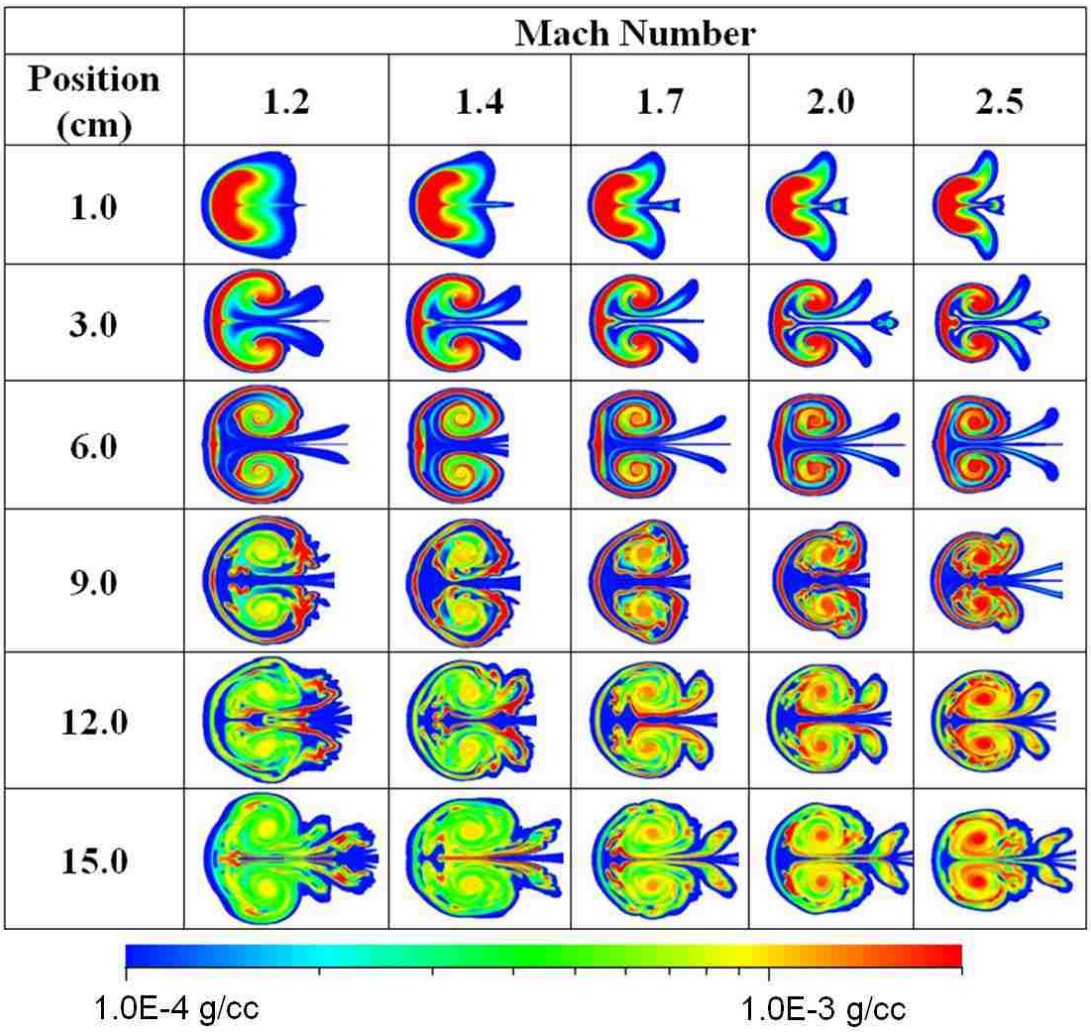

Figure 5.7: Density contours from SHAMRC calculations at Mach numbers ranging from M=1.2 to M=2.5.

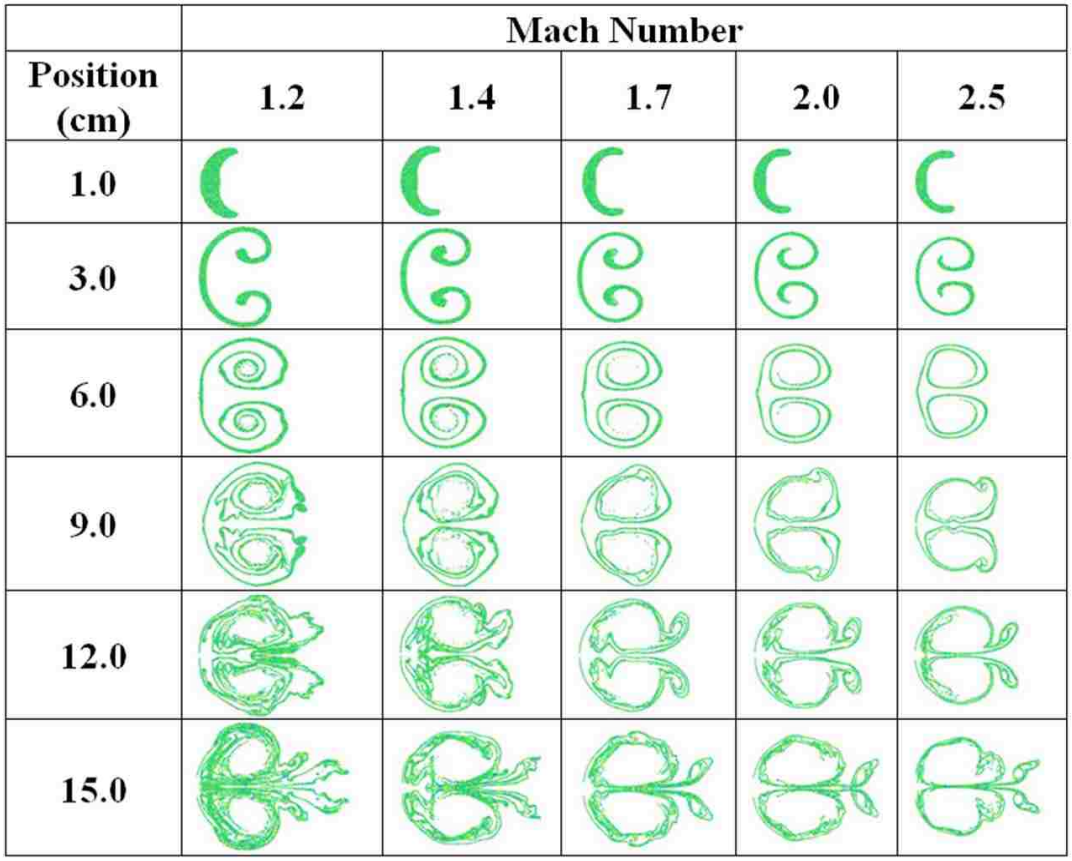

Figure 5.8: Particle plots from SHAMRC calculations for Mach numbers ranging from M=1.2 to M=2.5.

presented in Figure 5.3 for increasing Atwood number with a couple of differences, primarily visible during the compression phase. First, increasing shock strength leads to a higher pressure ratio across the shock, which results in a larger compression and a smaller initial instability width. Second, higher Mach numbers have faster piston velocities, which results in a shorter time required to compress the initial conditions.

The non-dimensional scaling developed in the previous section was applied to the SHAMRC results and is shown in Figure 5.10. The values for w_0 and t_0 are shown in Table 5.5. The proposed scaling does a good job of collapsing the SHAMRC results

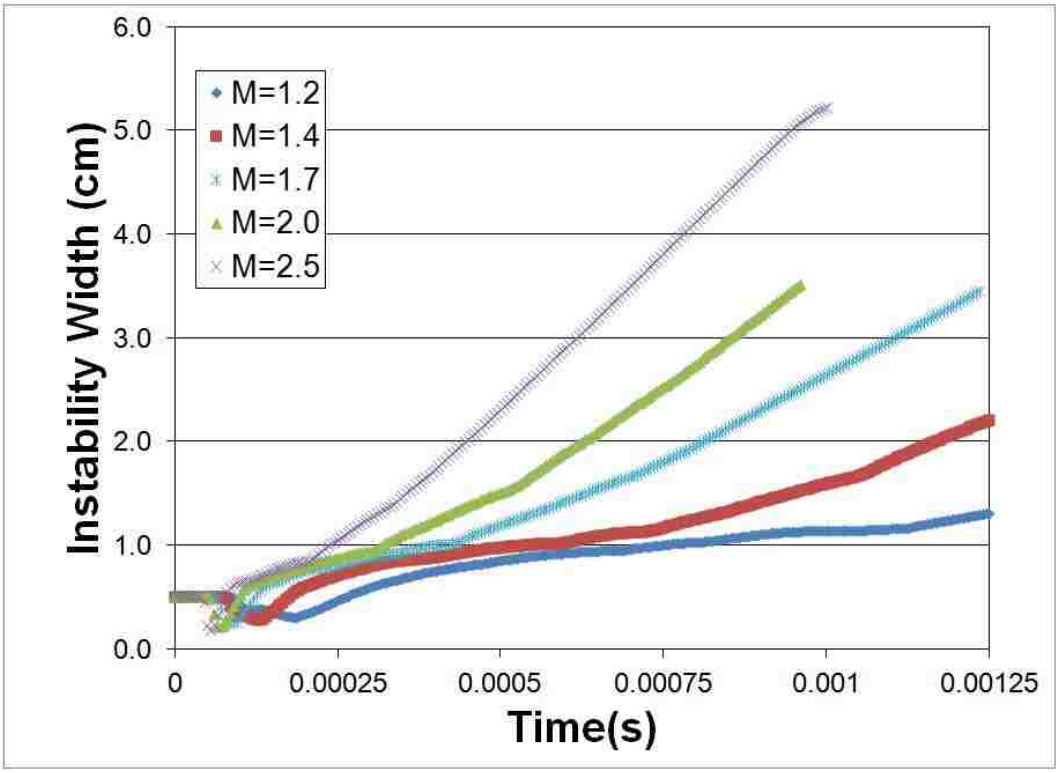

Figure 5.9: Instability size as a function of time for multiple Mach numbers.

to a curve of approximately the same shape; however, there appears to be an offset between the results at different Mach number. A similar result was observed by Orlicz et. al. [34]. In that work, experiments were performed for a curtain of SF_6 at Mach numbers 1.2 and 1.5. They were able to collapse their results for these two Mach numbers to a single curve by adding a small offset. By looking at Figure 5.10, it appears that this method will not be sufficient to collapse the results to a single curve as the distance between the curves is not constant for differing Mach number. Instead, a new Mach dependent non-dimensional instability width σ^* is defined as $\sigma^* = \frac{w}{w_0} M^a$, where M is the Mach number and a is a scaling parameter. Figure 5.11 shows results for $a = -0.4$. This scaling appears to collapse the results to a single curve for times leading up to the formation of the secondary instabilities and is good for a range of Mach numbers.

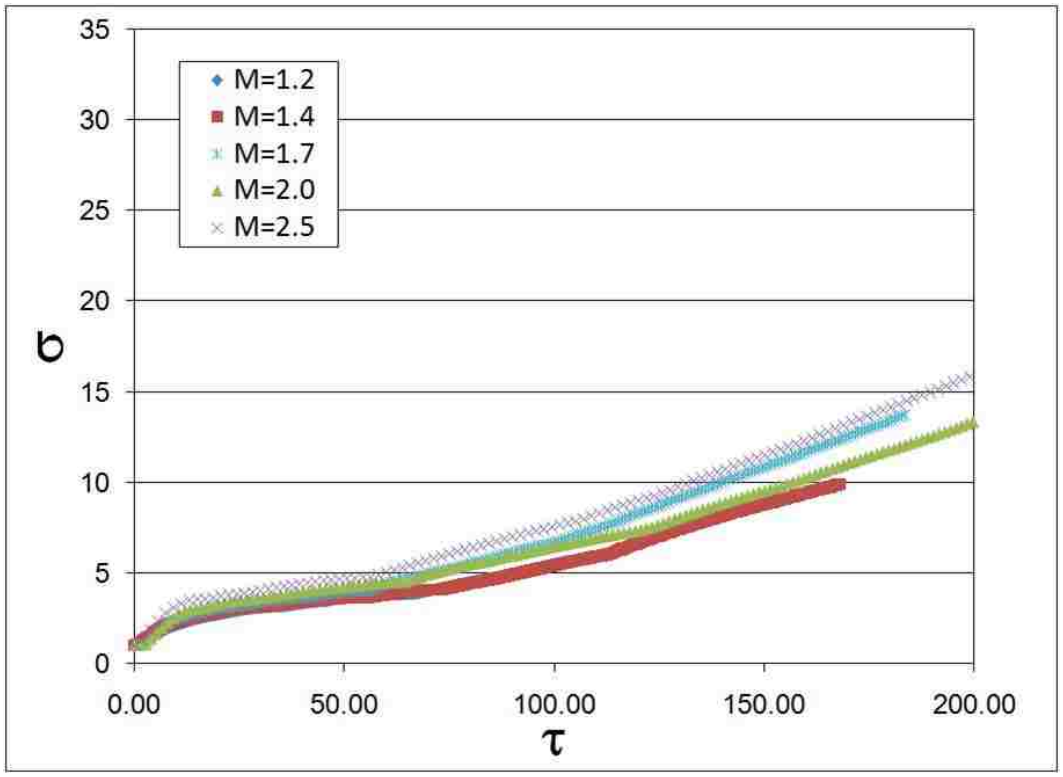

Figure 5.10: Scaled instability width as a function of scaled time for multiple Mach numbers.

Table 5.5: Initial times and perturbation widths.

Mach Number	t_0 (s)	w_0 (cm)
1.2	1.8×10^{-4}	0.3007
1.4	1.3×10^{-4}	0.2779
1.7	8.0×10^{-5}	0.2516
2.0	6.5×10^{-5}	0.2097
2.5	5.5×10^{-5}	0.1781

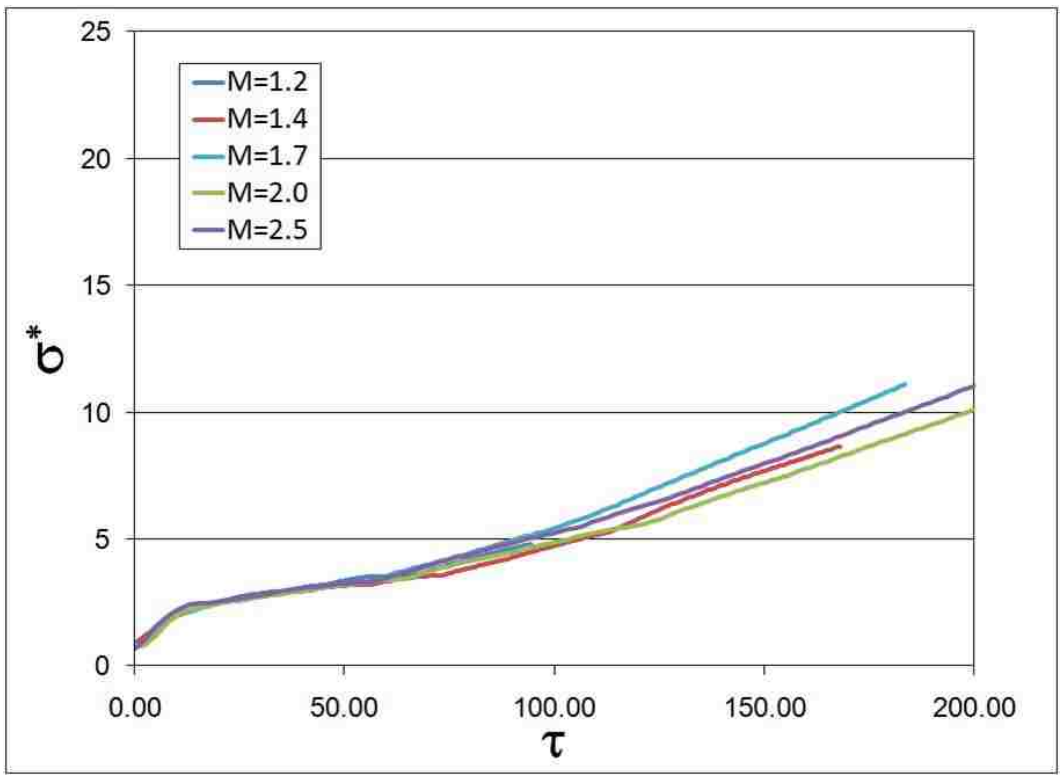

Figure 5.11: Scaled instability width as a function of scaled time for multiple Mach numbers with new scaling.

Chapter 6

Three-dimensional Richtmyer-Meshkov Instability

6.1 Overview

The previous chapters presented experimental results for initial conditions that were assumed to be nearly 2D. Making this assumption allows for two simplifications, one for experimental visualization and the other for numerical modeling. From an experimental point of view, the assumption of 2D initial conditions means that the experimental images obtained will be identical regardless of the vertical position of the visualization plane in the shock tube cross section. From a numerical point of view, this assumption allows for great simplification of the calculations and eliminates the need for costly 3D simulations, thus reducing the time required to obtain results, or allowing for calculations at a much higher level of resolution. This chapter addresses this assumption in detail by presenting experimental results obtained at multiple planes in the shock tube and results from full 3D calculations for both the traditional and multi-phase RMI presented previously. Additionally, the results

presented in this chapter will be used as a baseline in the next chapter, where the shock tube is tiled to create an angle of incidence between the shock wave and the gas column.

6.2 Experimental Results

To examine the three-dimensionality of the instabilities generated, the imaging system was modified to visualize a vertical cross-section of the flow as opposed to the horizontal planes presented previously. Figure 6.1 shows schematics for both horizontal and vertical planes of visualization. In the horizontal configuration, the laser sheet passes through test section, illuminating a cross-section of the gas cylinder. Images are captured via a mirror mounted to the top of the test section. For vertical planes, the laser sheet passes through the test section by reflecting it off the mirror used to acquire the horizontal images. Experimental images are taken by the camera directly through the side of the test section. This method works well for imaging any regions downstream of the initial conditions, however, it is not possible to create vertical slices of the initial conditions using this technique due to obstruction of the laser sheet by the initial condition nozzle. To overcome this difficulty, the laser sheet was directed through an optical window mounted at the end of the runoff section, which provides unobstructed access for the light sheet. The drawback of this configuration is that only one laser can be used, thus limiting the number of images that can be obtained to two.

Figure 6.2 shows vertical slices of the initial conditions and instability that is created for the air-droplet initial conditions accelerated by a M=1.67 shock. The figure is a compilation of images obtained from four different experiments. As there is only one laser (two pulses) available for imaging of the initial conditions in the vertical plane, each experiment yields only two images and several experimental

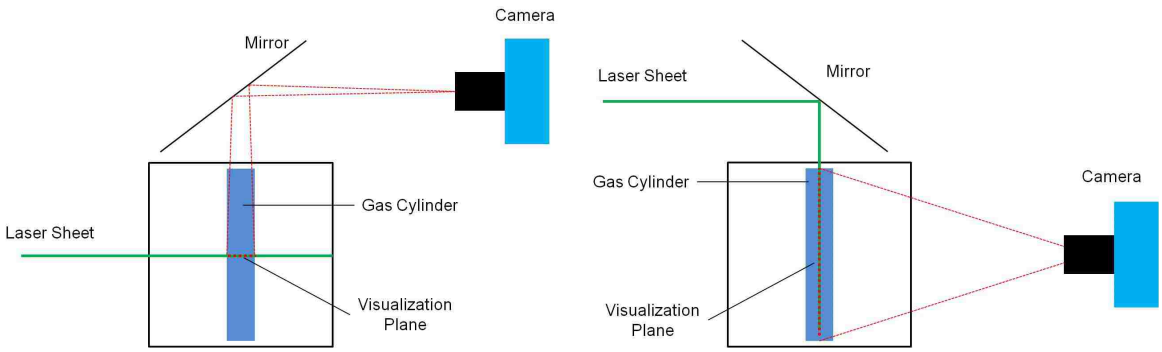

Figure 6.1: Schematics for image acquisition in the horizontal (left) and vertical (right) planes.

runs were performed with differing delays between the two frames to obtain images at multiple downstream locations. The frame height of each image is 7.62 cm to capture the entire vertical extent of the gas column. The images span a time of 225 μs after shock acceleration over a distance of approximately 7 cm downstream of the initial conditions. Note that the spacing between these images is not to scale. The direction of travel is from left to right. There is very little of the instability structure visible in these images as the growth rate of the multi-phase instability is slow due to the low Atwood number, as was discussed in Chapter 4. One feature of note is the bend in the column at the top and the bottom of the shock tube as it is accelerated downstream. This is an interesting feature as it shows that the initial conditions, which started as a right cylinder, do not maintain this shape near the top and bottom on the shock tube. This feature will be explored in greater detail in the numerical modeling section. Also of note, is that the angle of the column with respect to the horizontal is nearly constant at all times.

The left side of Figure 6.3 shows a compilation of images in the vertical plane produced by accelerations of the SF_6-droplet initial conditions by a M=1.67 shock. The frame width is the same as for the air-droplet initial conditions show previously, however, the images only span a range of 125 μs due to the increased width of the

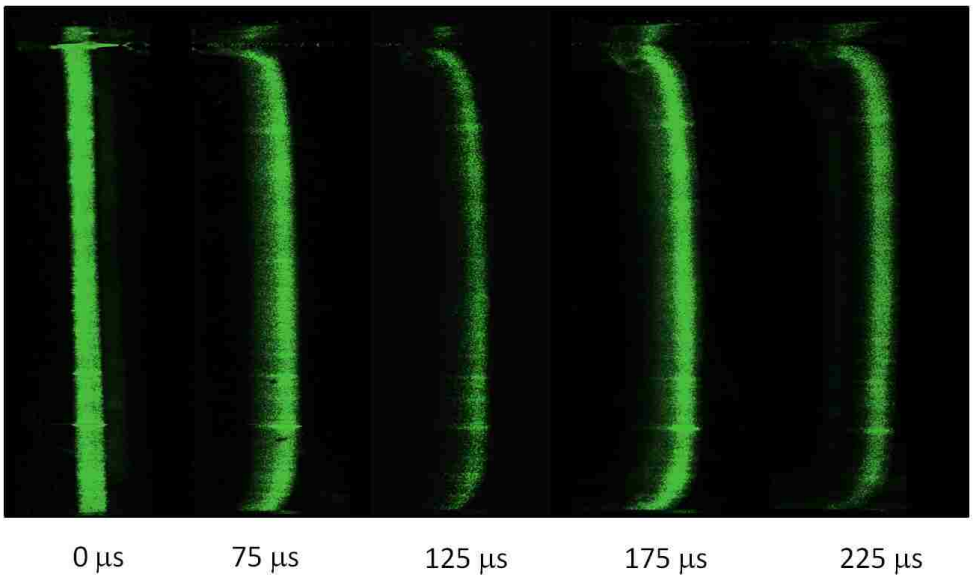

Figure 6.2: Experimental images in the vertical plane of the air-droplet instability at M=1.67 for early times.

instability in the streamwise direction. Again visible in these images is the bend in the cylinder at the top and the bottom of the shock tube. On the right of Figure 6.3 is a characteristic image taken from the horizontal plane at 100 μs. Two regions of importance are highlighted in this image. The first, denoted A, is a bridge of material that forms between the two vortex cores. This structure is always visible in the vertical visualization plane as it crosses the centerline of the instability (shown as a the dashed line), which coincides with the laser sheet. It is the sole structure seen in the vertical plane at 75 μs and is the left-most structure visible at 125 μs. The second region of interest, denoted B, is the point along the centerline where the two counter-rotating vorticies are closest to one another. This point also shows up in the vertical plane and is visible as the right-most structure at 125 μs. This region may not actually cross the centerline, however, it is illuminated due to the presence of particles in or near the laser sheet. It may or may not be visible depending on the size of the instability.

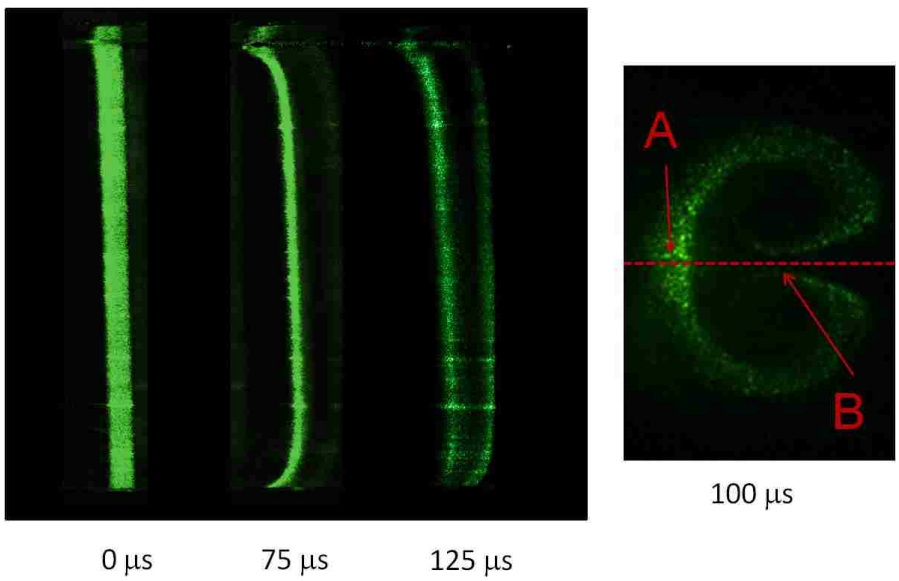

Figure 6.3: Experimental images in the vertical plane of the SF_6-droplet instability at M=1.67 for early times (left) and a characteristic image from the horizontal plane along the centerline (right).

Figure 6.3 shows vertical slices of both instabilities at a distance of 19.05 cm downstream of the initial conditions and are taken approximately 600 μs after acceleration by a M=1.67 shock wave. This image illustrates the differences in the growth rates of the two instabilities. The multi-phase instability has a small growth rate, and the secondary structures are not large enough to meet at the centerline and thus are not visible in the vertical plane. The traditional Richtmyer-Meshkov instability has a much higher growth rate and at these late times and forms a secondary plume of material that is ejected from the center of the instability. This plume forms the main structure visible in this image. Also visible is the bridge connecting the two vortex cores at the back of the instability. At these late times, this bridge is no longer a vertical column due to the formation of secondary instabilities. The dark areas between the bridge and the plume are regions occupied by the centers of the vortex pairs. The instability also has a noticeably different structure near the top and bottom of the shock tube and the curvature of the column is still visible, al-

though not as apparent as in the multi-phase instability. The angle that the back of the column makes with the horizontal is nearly constant in times, however the downstream side of the column appears to rotate due to the increased growth rate and thus wider instability perturbation width near the top of the column.

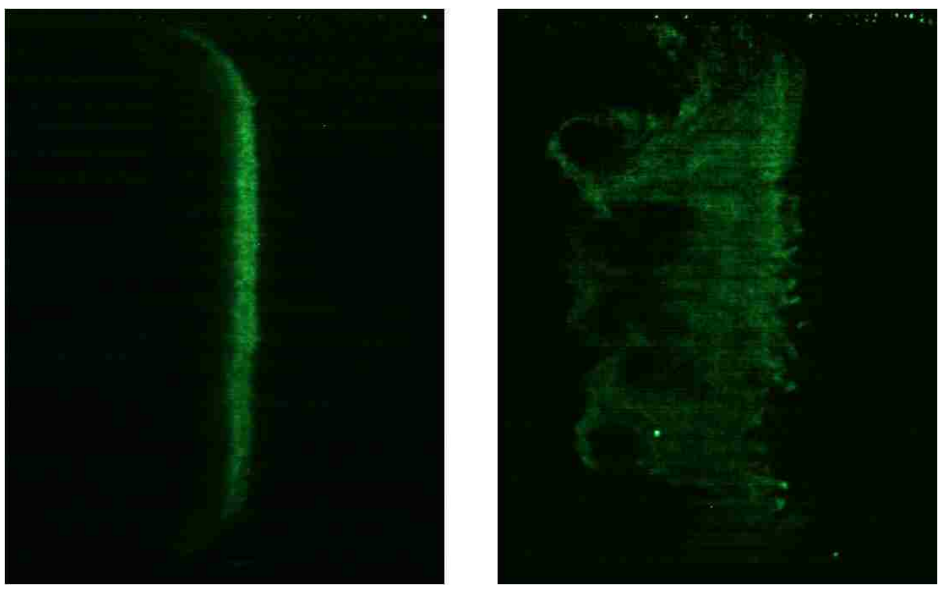

Figure 6.4: Experimental images in the vertical plane of the air-droplet (left) and SF_6-droplet (right) instabilities at M=1.67, 19.05 cm downstream.

6.3 Numerical Setup

To model the experimental results, 3D SHAMRC calculations were performed. The gas cylinder was generated by using the FLUENT results obtained in Chapter 3. In 2D, the FLUENT results were imported into SHAMRC by generating a cubic spline that matched the density as a function of radius. This spline was used to generate a series of annuli (25 separate rings for air and SF_6) with varying density to create the cylinder of initial conditions. This method is not feasible for 3D as it involves generating a different cubic spline for each column height. Instead, the

2D FLUENT results were imported into a 2D SHAMRC calculation using the area feed-in option. This capability fills a region of a SHAMRC mesh with conditions supplied via an auxiliary data file, which contains cell properties on a triangular grid. The data file is created by a standalone program that parses a file containing a series of points containing pertinent hydrodynamic variables (velocity, pressure, temperature, density). The standalone program generates a triangular mesh of data points that can be read by SHAMRC. The resulting 2D SHAMRC mesh can be read into a 3D SHAMRC mesh in a process which maps the 2D plane into a 3D cylinder. The particles are generated in the same fashion. A FLUENT dump containing information about the particle mass for each cell in the mesh is used to generate a 2D SHAMRC mesh which contains zones filled with a place holder material. This mesh is again read into a 3D SHAMRC mesh and particles are placed into each cell containing the place holder material, similar to the 2D initial conditions created in Chapter 3. Approximately 2 million particles are required for a 3D calculation with one computational particle per cell.

The 3D calculations were split into two steps, both with a zone resolution of 0.01 cm in all directions. The total cell count for each calculation was approximately 600 million zones. The first step spans from 3.0 to 17.0 cm in the x-direction, from 0.0 to 3.81 cm in the y-direction (utilizing a half-plane of symmetry), and from -7.0 to 7.0 cm in the z-direction. The shock wave propagates in the x-direction with the gas column centered at 4.5 cm. The shock wave was generated by a constant feed in boundary condition with material properties for M=1.67 as defined in Chapter 3. The shock tube has a height of 7.62 cm, however, to model the holes in the shock tube for the gas cylinder entrance and exit the mesh was extended beyond the shock tube walls and filled with non-responding islands with a cylinder cut in them. The islands behave as a solid surface that is not affected by the surrounding flow and are used in SHAMRC to generate solid objects.

Figure 6.5 shows a vertical slice from the SHAMRC calculation. This figure consists of contours of fluid density and shows the initial gas column as well as the holes in the shock tube. The islands are plotted in white. The calculation was run until just before the shock wave exits the mesh. At this time, the instability has passed from the region containing the holes in the shock tube and as a result, the mesh can be resized in the z-direction. The results of step 1 were placed into a second calculation that spans from -3.81 to 3.81 cm in the z-direction and from 10 cm to 30 cm in the x-direction. The y-direction extent was unchanged. Additionally, to minimize boundary effects, expanding zones were added to the mesh in the x-direction beyond 30 cm to allow for run-off of the shock wave. These zones start at a resolution of 0.01 cm, but increase in size by 5% every zone. This allows the mesh to be extended far beyond the area of interested with minimal computational expense.

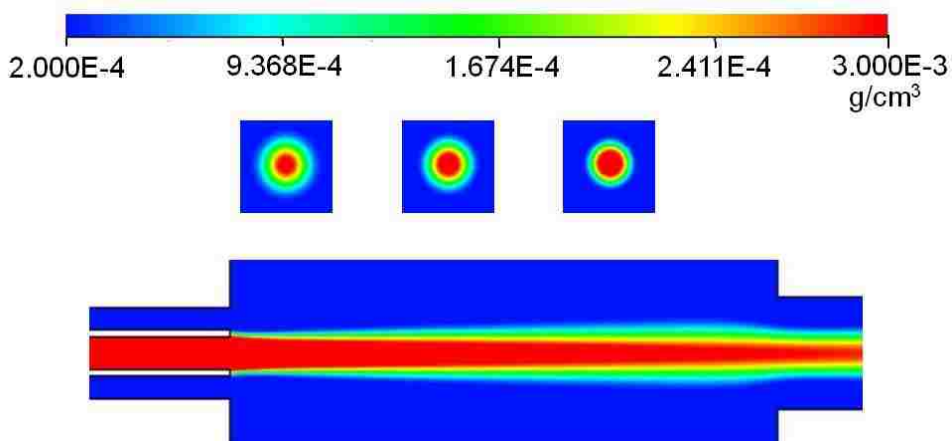

Figure 6.5: SHAMRC density contours of the initial conditions in the vertical plane.

6.4 Numerical Results

Figure 6.6 shows results from the SHAMRC calculation of the air-droplet instability from the 0 to 225 μs. The numerical images represent particles that are in a vertical

plane comprising the instability center. Particles are plotted for the 5 planes on either side of the requested plane, in this case from -0.05 to 0.05 cm. It is possible to plot a single plane of particles, however, in the experimental imagery, the laser sheet has a finite thickness, and illuminates particles that fall within or very near to the thickness of the laser sheet. The particles are colored by particle radius. The numerical images are similar to the experimental images introduced in the first section for the air-droplet initial conditions. The cylinder is compressed by the passing shock and displays very little visible structure. The curvature of the instability near the top and bottom of the shock tube is also observed. The numerical instability appears slightly smaller than what is observed in experiments due to the uniform distribution of particles diameters at 1 micron. A particle distribution over a range of diameters would generate a instability that is wider due to the differences in the acceleration by drag of particles with differing diameters. Figure 6.7 displays vertical slices at -2.0, 0.0, and 2.0 cm. This figure shows the uniformity of the multi-phase instability throughout the mid-section of the column.

Figure 6.8 shows results for the SHAMRC calculation of the SF_6-droplet instability from the 0 to 175 μs. These images differ more from the experimental results than the air-droplet instability. Most notably absent is the lack of a well defined secondary structure that appears downstream of the bridge connecting the vortex cores at later times. In the numerical images, this column appears much thicker near the top of the instability and disappears near the bottom of the instability. This is caused by the differences in the structures that are formed in the horizontal plane. Another feature is the curvature at the bottom of the shock tube. At 75 μs there is a distinct curve, which disappears as the instability develops. The multiphase instability also generates this backward curve, however it stays fairly constant as the instability moves downstream. A similar type of behavior is observed in the experimental images for both types of instabilities. This curve is also visible at the top of the column and appears to form into a vortex at later times.

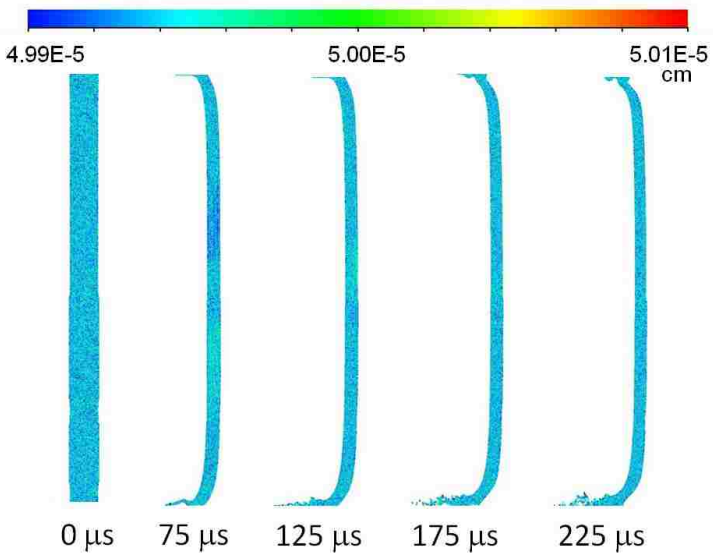

Figure 6.6: SHAMRC images in the vertical plane of the air-droplet instability at M=1.67 for early times.

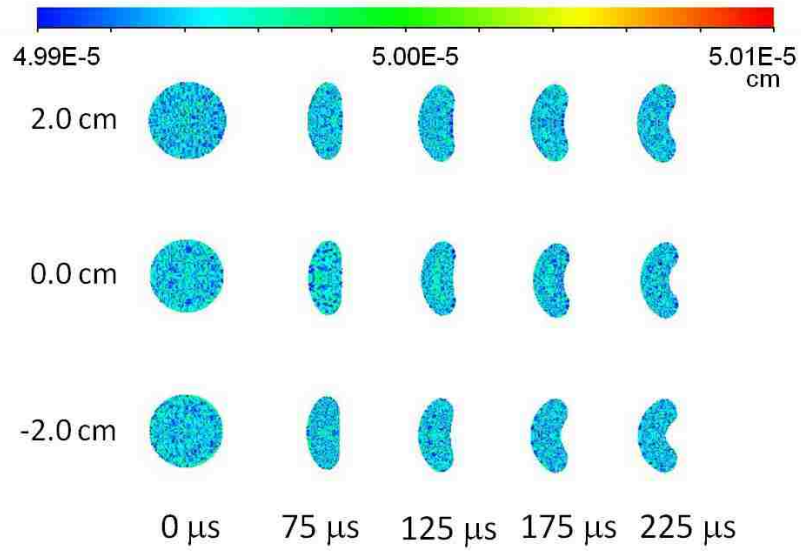

Figure 6.7: SHAMRC images in the horizontal plane of the air-droplet instability at M=1.67 for early times.

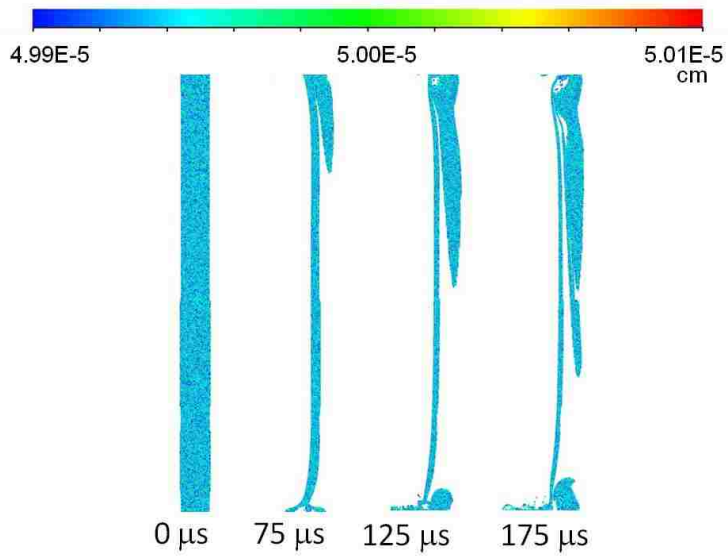

Figure 6.8: SHAMRC images in the vertical plane of the SF_6-droplet instability at M=1.67 for early times.

Figure 6.9 shows particle images from horizontal planes at -2.0, 0.0, and 2.0 cm. These images correlate with the vertical images from Figure 6.8 and illustrate how the instability differs are various heights in the column. Two counter-rotating vorticies are formed at all heights, however, the vorticies form more quickly near the top of the column. The vorticies that form in the lower part of the column are farther apart due to smaller vorticity deposition due to smaller density gradients. These structures are not visible in the vertical planes until they near the centerline.

Figure 6.10 shows density contours along the centerline of the instability in the vertical plane. This image shows how the core of the high density gas narrows as it falls through the shock tube. As only the center plane is shown, there are no visible structures downstream of the bridge as observed in the experiments. However, instabilities that form near the top and bottom of the column are visible. These instabilities are barely visible in the early time experimental images, but lead to the formation of large secondary structures that are clearly visible in images from

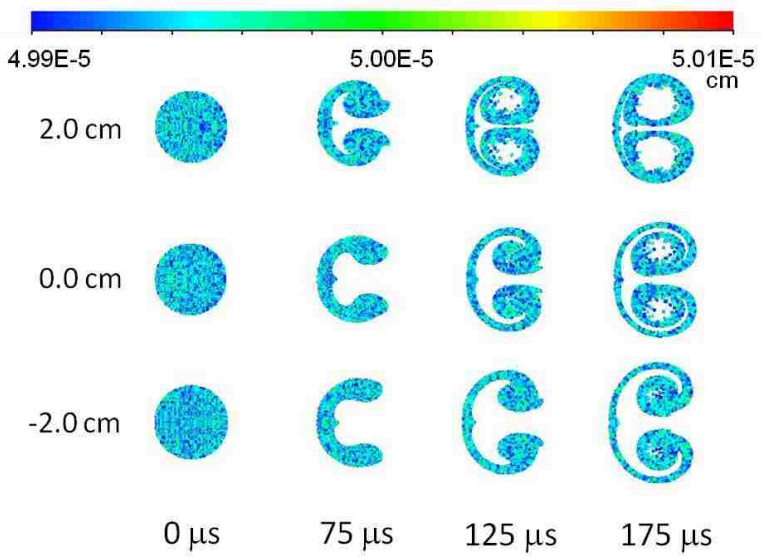

Figure 6.9: SHAMRC images in the horizontal plane of the SF_6-droplet instability at M=1.67 for early times.

farther downstream. These instabilities are formed by the interaction of the shock wave with the initial condition holes in the shock tube. As the shock wave passes over the holes in the shock tube, the shock wave expands into the voids. This causes a local reduction in pressure, resulting in a lower shock strength. When the locally weaker shock accelerates the gas column, it lags behind the center of the column, creating the bend that is visible in both experimental and numerical images.

Figure 6.11 shows horizontal slices at -2.0, 0.0, and 2.0 cm for the same times as Figure 6.10. These images display how the instability evolution changes as a function of column height and downstream position. Near the top of the gas column, the core of high density gas is nearly the width of the inner initial condition tube, while towards the bottom the core narrows to a much smaller diameter. This results in a locally higher density gradient near the top of the cylinder and a larger amount of vorticity deposited. Due to the higher vorticity, the instability develops faster. The overall diameter of the cylinder is fairly constant along the height, although it

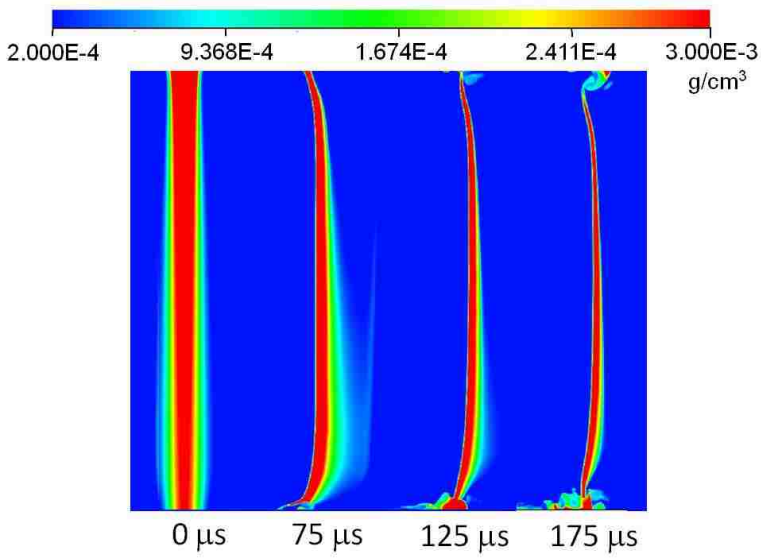

Figure 6.10: SHAMRC images in the vertical plane of the SF_6-droplet instability at M=1.67 for early times.

does widen slightly near the bottom. As a result the instability that forms has a larger perturbation height near the bottom of the shock tube.

To examine the effects of the holes at the top and bottom of the shock tube on the instability, the first step of the SHAMRC calculation with the SF_6 initial conditions was run with a mesh that terminated at -3.81 and 3.81 cm in the z-direction. This effectively removed the holes from the calculation and is a setup which cannot be repeated experimentally. Figure 6.12 shows density contours in the vertical plane from this calculation. The top of the column remains nearly straight, with a very small instability visible at 175 μs. At the bottom of the shock tube, the column bends in the opposite direction as observed in Figure 6.10 and Figure 6.6 for the multi-phase instability. This bend is caused by the variation in the density near the bottom of the column, a feature that is not present in the multi-phase case. When the holes are included in the calculation, this variation in density cancels out the deceleration caused by the locally lower shock pressure. The result is a column that

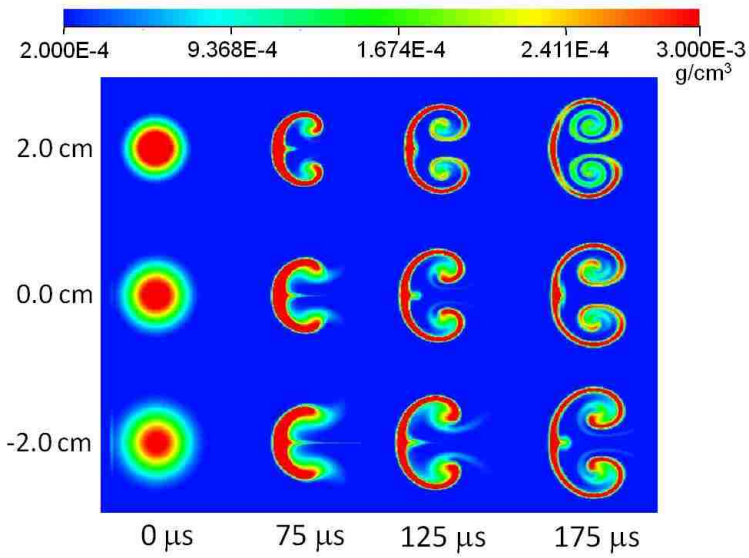

Figure 6.11: SHAMRC density contours in the horizontal plane of the SF_6-droplet instability at M=1.67 for early times.

appears to have a both a backward and forward bend at later times. In the late time experimental images of traditional RMI, shown in Figure 6.4, there appears to be material ahead of the instability, confirming these results.

Figure 6.13 shows late time images of particles in the vertical plane from the SHAMRC calculations of the air-droplet (left) and SF_6-droplet (right) instabilities. The images were obtained 19.05 cm downstream of the gas cylinder and can be compared directly to Figure 6.4. Both are good matches to their experimental counterparts. The multi-phase instability exhibits very little structure in this plane apart from the curvature of the cylinder near the top and bottom of the shock tube. This bend is more pronounced at these late times. The most prominent feature of the traditional Richtmyer-Meshkov instability in this plane is the two vorticies formed during the interaction between the passing shock wave and the initial condition holes in the shock tube walls. The early time images in Figures 6.8 and 6.10 show the formation of these structures at early times.

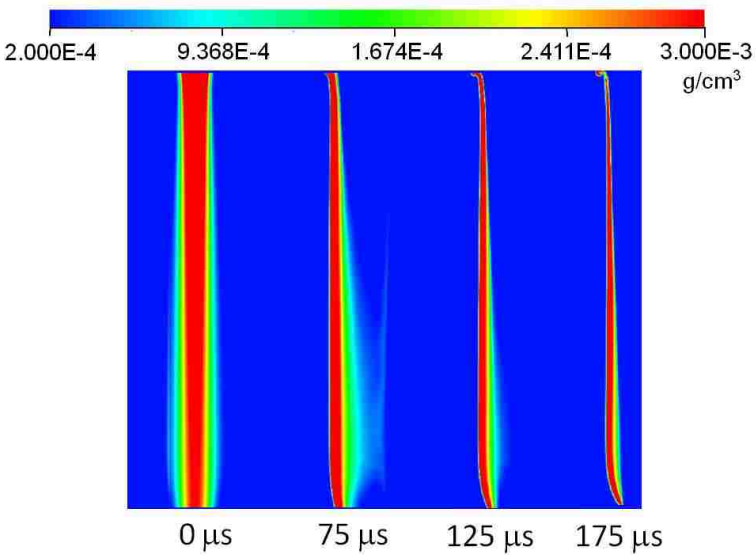

Figure 6.12: SHAMRC images in the vertical plane of the SF_6-droplet instability formed with no holes in the shock tube.

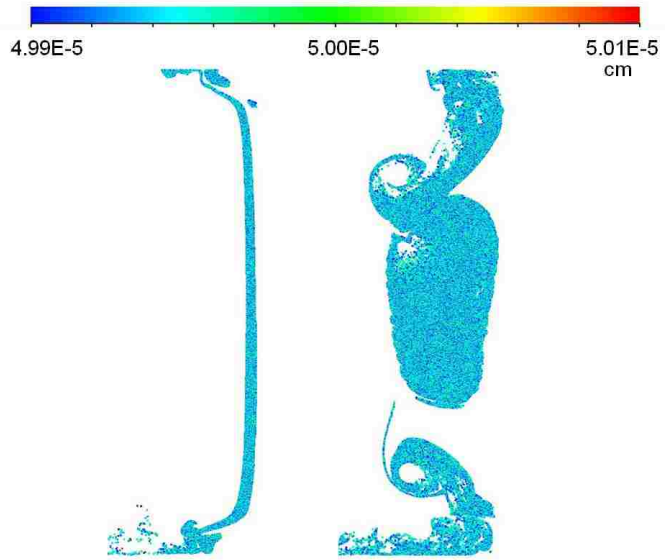

Figure 6.13: SHAMRC images in the vertical plane of the air-droplet instabilities at M=1.67 for late times.

Chapter 7

Richtmyer-Meshkov Instability Formed by an Oblique Shock

7.1 Overview

The previous chapter presented experimental and numerical results for a planar shock wave accelerating either a column of sulfur-hexafluoride (SF_6) or air seeded with glycol droplets. In this chapter, experimental and numerical results are presented for the case where there is an angle of incidence between the initial condition column and the plane of the shock wave. This angle of incidence makes the instability fully 3D, and in this case, cannot be recreated with 2D simulations. The experimental and numerical results will be compared to observations from the previous chapter to examine the behavior of the instability after such an acceleration.

7.2 Experimental Results

To create a non-planar interaction between the shock wave and the gas column, the shock tube was tilted to an angle of 15 degrees from the horizontal. The shock wave was formed by the release of high pressure gases from the driver section and as such traveled in a plane perpendicular to the walls of the shock tube. The gas column was formed identically to the initial conditions used in the previous chapter with the exception that the test section for these experiments had offset holes on top and bottom to allow the passage of the vertical column through the inclined test section. Imaging was again performed in the vertical cross-section to examine how the instability evolves in the third dimension.

Figure 7.1 shows vertical slices of the initial gas column and instability that is created for the air-droplet initial conditions accelerated by a M=1.67 shock. The images are compiled from three experiments due to the limitation of two laser pulses per experiment. The frame height and width are 7.62 cm and the images span a time of 200 μs after shock acceleration. To acquire these images, the camera is tilted at an angle of 15 degrees, causing this initial conditions to appear rotated with respect to the bottom of the image. These results appear very similar to those presented for the multi-phase instability in Chapter 6. There is a curvature at the top and bottom of the gas column due to the interaction of the shock wave and holes in the test section. A feature that is noticeably different is the angle that the column makes with respect to the horizontal after acceleration by the shock wave. Initially, the column is inclined at an angle of 15 degrees. After acceleration, this angle is smaller (approximately 10 degrees) and remains fairly constant in the next two images.

The deposition of vorticity by the passing shock wave will cause the column to rotate in a clock-wise direction, however, the density gradient for the multi-phase instability is relatively small when compared to traditional RMI, as was demonstrated

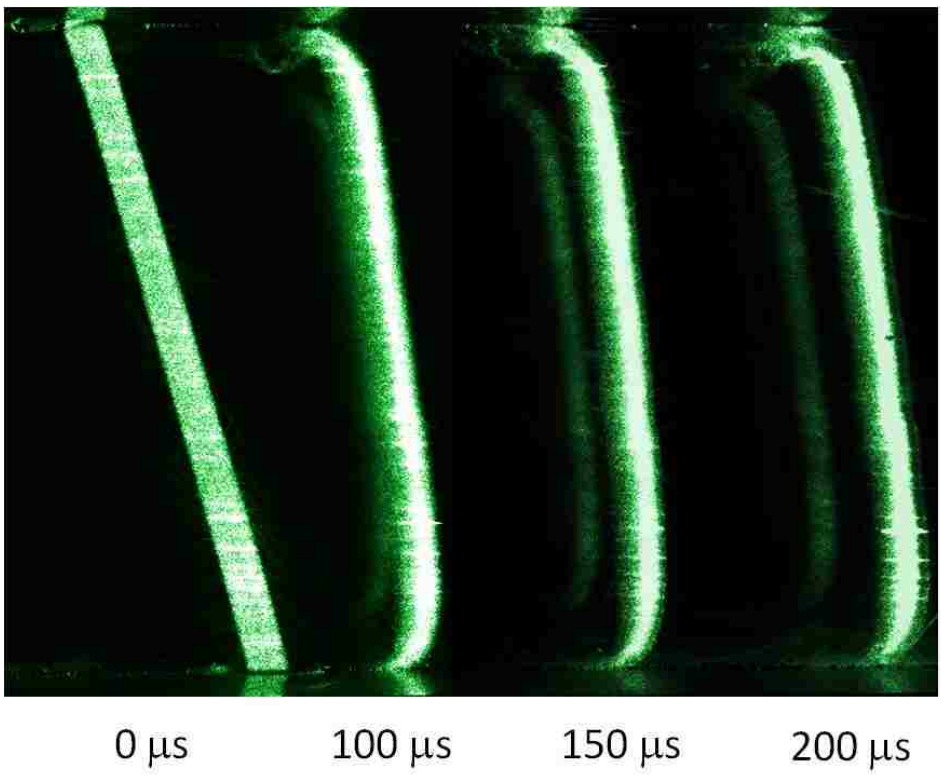

Figure 7.1: Experimental images in the vertical plane of the air-fog instability at M=1.67 for early times.

in Chapter 4. This results in a smaller amount of vorticity generated and is likely not sufficient to account for the initial rotation. This observation is confirmed by observing that the relative angle of the column at late times, as the change in this angle represents the rotational rate of the instability. Instead, the change in angle is likely caused by compression as the shock wave passes through the initial conditions. This will be explored in greater detail in the next section.

Figure 7.2 shows vertical slices of the initial conditions and the instability that is created when a M=1.67 shock wave accelerates a column of SF_6 seeded with droplets. These images show the same type of initial rotation as the air-droplet instability, however, there also appears to be a small amount of additional rotation

of the column between 100 and 200 μs. Also of interest is the waviness of the bridge connecting the vortex pair. This is a phenomenon not observed in the planar shock interaction and appears to be unique to this oblique interaction. Additionally, the size of the secondary instability that is created near the top and bottom of the shock tube is increased. At 200 μs, a dark region near the bottom of the shock tube indicates the presence of a vortex.

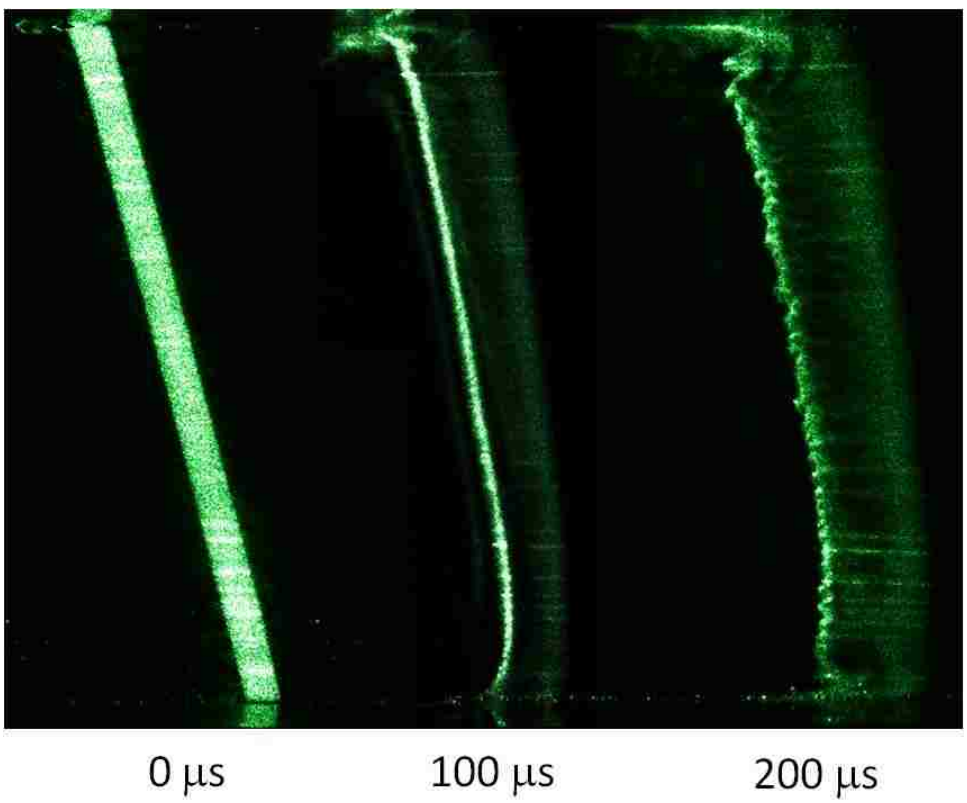

Figure 7.2: Experimental images in the vertical plane of the SF_6-fog instability at M=1.67 for early times.

Figure 7.3 shows vertical slices of both instabilities at a distance of 19.05 cm downstream of the initial conditions and are taken approximately 600 μs after the initial acceleration. The multi-phase instability, shown on the left, demonstrates a larger curvature near the top of the shock tube than what is observed at the bottom.

This is a feature not seen in the case of acceleration by a planar shock. The traditional RMI, shown on the right, has a large kink on the downstream edge approximately one quarter of the shock tube height from the top of the instability. This structure was also not present when accelerated by a planar shock.

Figure 7.3: Experimental images in the vertical plane of the air-fog (left) and SF_6-fog (right) instabilities at M=1.67, 19.05 cm downstream.

7.3 Numerical Setup

A 3D SHAMRC calculation was used to model the experimental results. The calculations were run identically to the 3D calculations from the previous chapter. To simulate the angle of the shock tube, the gas column and the holes in the shock tube were rotated counter-clockwise by an angle of 15 degrees. Due to the rotation, the distance that the initial conditions travel through the shock tube is increased. To accurately capture the evolution of the column as it passes through the shock tube, an additional FLUENT calculation was run. This calculation was identical to the calculation used to generate the gas column initial conditions in Chapter 6, with the exception that the distance between the top and bottom wall of the shock tube was increased to 7.89 cm instead of 7.62 cm. Figure 7.4 shows the initial conditions as generated in SHAMRC.

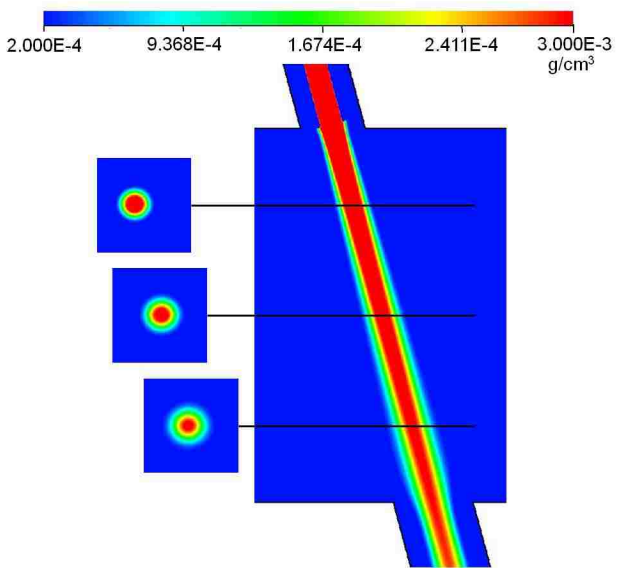

Figure 7.4: SHAMRC density contours of the initial conditions in the vertical plane.

7.4 Numerical Results

Figure 7.5 shows results from the SHAMRC calculation of the air-droplet instability from the 0 to 200 μs. These images are identical to the experimental results presented in the previous section. The SHAMRC results capture both the initial rotation due to the passing shock and the relatively constant angle of the instability in the vertical plane thereafter. The calculation also captures the plume of particles that is generated by the shock passing over the holes in the top and bottom of the shock tube. Due to the angle of the holes, this plume is enhanced on the upper surface and suppressed on the lower surface. This is effect is identical to what is seen in experiments. Figure 7.6 shows horizontal slices at -2.0, 0.0, and 2.0 cm. The images are arranged so that their position in the image is relative to their horizontal displacement in the vertical column. Displaying the images in this manner clearly illustrates the rotation of the cylinder as it evolves. The horizontal images are similar in shape to those presented in Chapters 4 and 6, displaying little growth due to the relatively low Atwood number.

Figure 7.7 shows results from the SHAMRC calculation of the SF_6-droplet instability from the 0 to 200 μs. These images are similar to the images presented in Chapter 6. The numerical images show more particles in the centerline plane downstream of the bridge than the non-inclined counterpart. As with the air-droplet column, the instability that is formed near the top of the shock tube is enhanced, while the instability at the bottom is suppressed. Figure 7.8 shows slices in the horizontal plane for -2.0, 0.0, and 2.0 cm. The images are staggered to indicate their relative position in the vertical plane. The oblique shock interaction creates vorticies that are closer together than what is generated by the planar shock. This is also reflected in the vertical slices by the more pronounced downstream column, which is formed when the vorticies meet near the centerline downstream of the bridge.

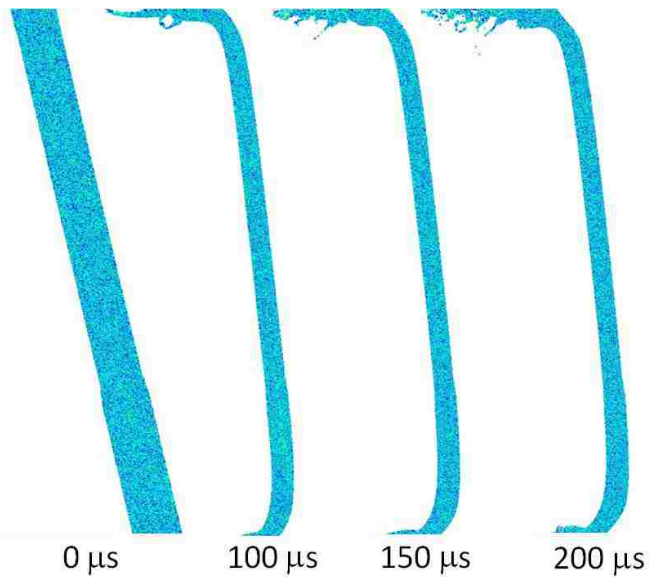

Figure 7.5: SHAMRC images in the vertical plane of the air-droplet instability at M=1.67 for early times.

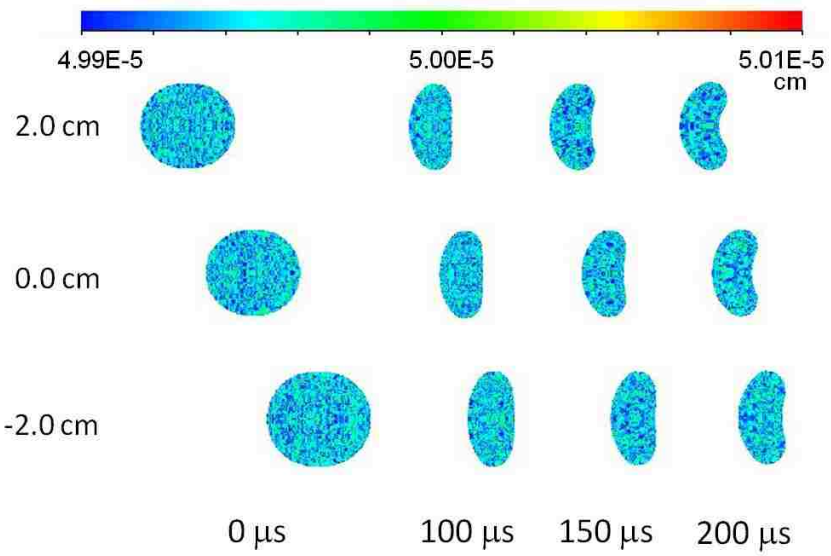

Figure 7.6: SHAMRC images in the horizontal plane of the air-droplet instability at M=1.67 for early times.

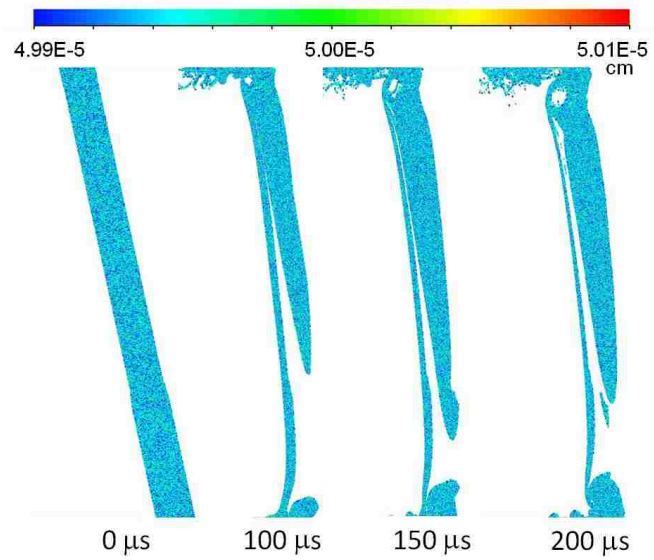

Figure 7.7: SHAMRC images in the vertical plane of the SF_6-droplet instability at M=1.67 for early times.

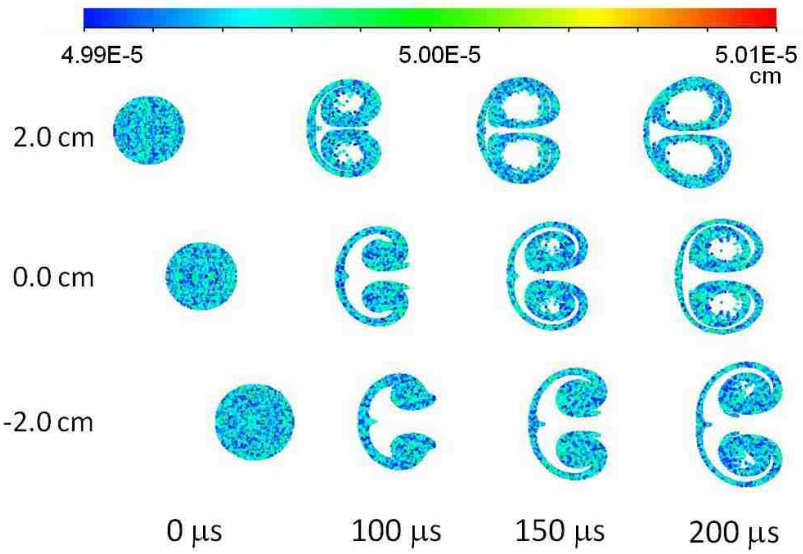

Figure 7.8: SHAMRC images in the horizontal plane of the SF_6-droplet instability at M=1.67 for early times.

Figure 7.9 shows density contours from the vertical plane along the instability centerline. From these images, the rapid development of the instability near the top of the shock tube is clear. This figure also illustrates the initial rotation of the gas column. It does not appear, however, that there is any significant rotation of the center of the column after the initial acceleration. There does appear to be more rotation near the bottom and top of the shock tube than was observed for acceleration by the planar shock wave. Figure 7.10 shows density contours in the horizontal plane for the SF_6-droplet instability. The images are again staggered to indicate their relative position in the vertical plane. The instability behaves similarly to what is observed when accelerated by the planar shock wave. The instability grows more rapidly near the top, where the core density is highest, and has the largest perturbation height near the bottom, where the initial diameter is the largest.

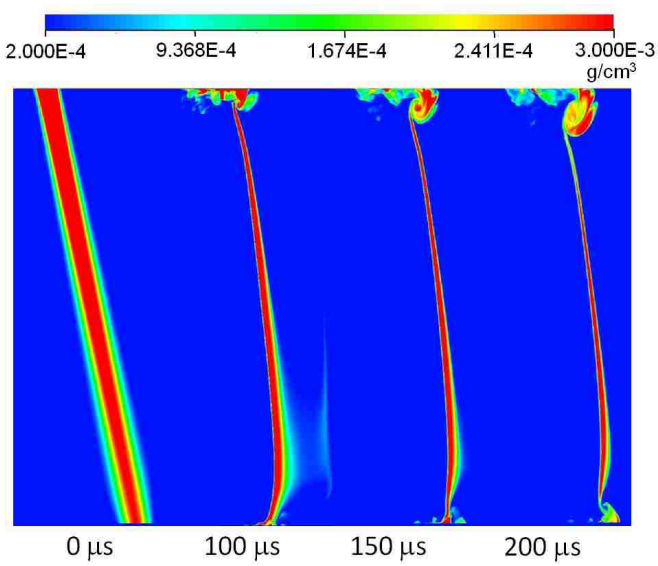

Figure 7.9: SHAMRC density contours in the vertical plane of the SF_6-droplet instability at M=1.67 for early times.

Figure 7.11 shows density contours in both the vertical and horizontal planes during the shock acceleration of the initial conditions. This image shows how the

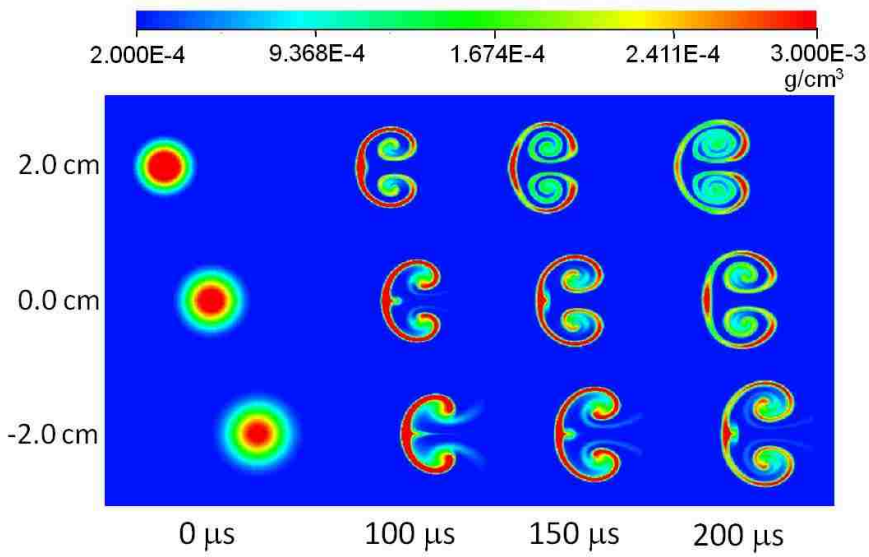

Figure 7.10: SHAMRC images in the horizontal plane of the SF_6-droplet instability at M=1.67 for early times.

passing shock compresses and rotates the gas column due to the angle of incidence between the two. The shock has passed through the top half of the column, which has a distinctly different angle than the unaccelerated bottom. A vertical line is shown on the image for reference. There is a distinct differences between this line, and the angle that the shock makes as it passes through the column. As the shock enter the column it slows down due to the higher density gas. This deceleration causes the shock wave to appear rotated with respect to the horizontal. The compression of the gas column occurs perpendicular to this shock and causes the apparent initial rotation of the initial conditions.

Figure 7.12 shows late time images in the vertical plane from the SHAMRC calculations of the air-droplet (left) and SF_6-droplet (right) instabilities. The images were obtained 19.05 cm downstream of the initial conditions and can be compared directly to Figure 7.3. These images are both good matches to the instability that is observed in experiments and are similar in morphology to what is observed for

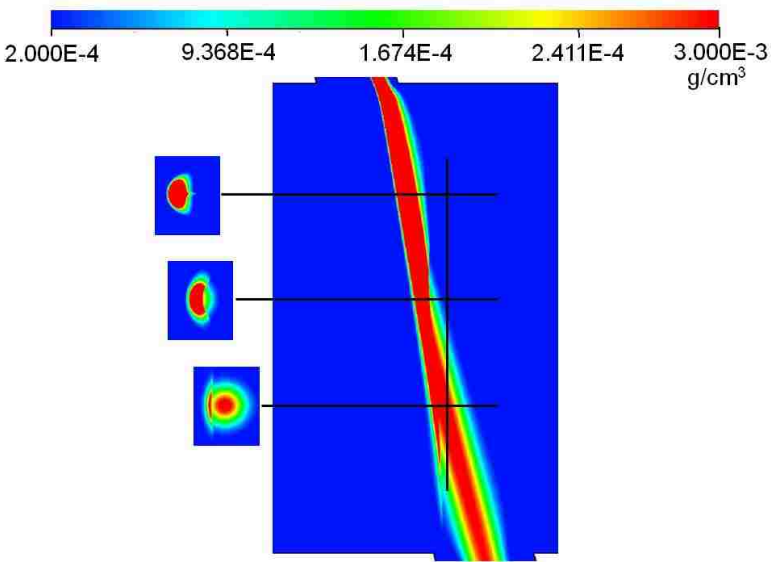

Figure 7.11: SHAMRC density contours of the SF_6-droplet instability showing the shock acceleration of the initial conditions.

acceleration by a planar shock. Of note is the increased curvature of the instability near the top of the shock tube for the multi-phase instability and the kink that is observed near the top for the SF_6-droplet gas column.

Initially, it was believed that there would be an apparent rotation of the instability due to the angle between the shock wave and the initial condition column, however, the numerical and experimental results presented here do not demonstrate a measurable rotation. It may be that the angle between the shock and the gas column is not large enough to produce a rotation that can be observed with these experiments. In the horizontal plane, the interaction between the shock and the cylinder forms an instability that grows rapidly due to the shape of the initial conditions. The rotation in the vertical plane may be easier to observe in an instability that is generated from small amplitude perturbations in the horizontal plane. Alternatively, it may be the case that the vorticity deposited in the horizontal plane stabilizes the gas column, leading to small local instabilities rather than a large scale rotation. In either case,

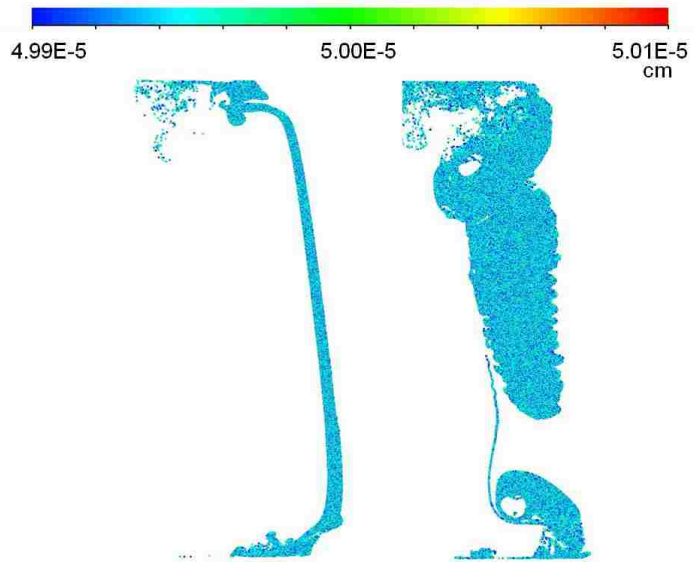

Figure 7.12: SHAMRC images in the vertical plane of the air-droplet instabilities at M=1.67 for late times.

more experimental and numerical investigations are be required to fully understand this phenomenon.

Chapter 8

Conclusions

This dissertation presented experimental and numerical results for single and multiphase fluid instabilities generated by shock acceleration of a column of gas seeded with glycol droplets. The experimental work was performed at the University of New Mexico tiltable shock tube facility, and the computational analysis was performed using the Eulerian hydrodynamics code SHAMRC. Experiments were conducted in two shock tube configurations, horizontal and at a tilt angle of 15 degrees. The experimental images were obtained in two visualization planes (horizontal and vertical) using a high speed camera and laser illumination.

Two cases were examined. The first was the traditional Richtmyer-Meshkov Instability (RMI), where the passing shock wave accelerated a column of sulfur hexafluoride (SF_6) seeded with glycol droplets. The experimental results were used as validation of the SHAMRC models and to understand interaction between the fluid and droplet phases. It was found that the droplets do not exactly follow the fluid flow and must be explicitly modeled to generate numerical results that match the experimental images. Two parameter studies were performed numerically to examine the effects of Atwood number and Mach number on the instability formation and

growth. The streamwise perturbation width growth rate was compiled for Atwood numbers ranging from 0.1 to 0.5 and Mach numbers ranging from 1.2 to 2.5. This quantitative comparison showed the differences in the perturbation widths at various Atwood and Mach numbers and that these results could be collapsed to a single curve by using a non-dimensional scaling involving these two parameters.

The second case considered was a multi-phase analogue to RMI where air is seeded with glycol droplets. In this case, there was no density gradient between the gas column and the surrounding air. It was shown experimentally that this scenario produces an instability that is similar to RMI in morphology despite the absence of a fluid-fluid density interface. This instability was treated numerically in two ways. The first method was to determine an average density for the initial conditions by spreading the mass of the particles out over the volume that they occupied. This method modeled the instability as traditional RMI with a very low Atwood number. The second method was to model the droplets as discrete particles. Both methods produced instabilities that were similar in morphology to those observed in experiments. However, only by modeling the initial conditions as discrete particles was is possible to recreate all of the features observed, namely a tail of trailing particles. As the motion of the particles is directly affected by their size, SHAMRC calculations were run with varying particles diameters. It was shown that increasing the particle diameter has the effect of increasing the perturbation height of the instability while reducing the growth rate of the perturbation width. It was also shown that if the particles are not uniformly sized, the instability forms a tail of trailing particles due to differences in drag forces, as was observed experimentally.

Finally, an experimental and numerical investigation of the three-dimensional effects of traditional and multi-phase RMI was performed. Experiments were run with the shock tube in a horizontal configuration and at an angle of 15 degrees. The experiments run with the shock tube in the horizontal position confirmed the assumption

that both types of instability can be treated as two-dimensional, especially near the center of the shock tube. However, near the top and bottom of the shock tube the column lags behind, creating a small curvature. The results from 3D numerical simulations agreed well with these experimental observations and were used to confirm that this curvature is primarily caused by interaction of the passing shock wave and the holes in the shock tube used for generation of the initial conditions. Additionally, for traditional RMI instabilities, there are vorticies that develop at late times due to this interaction. Tilting the shock tube changes the angle of interaction between the planar shock wave and the initial condition column. Experimental and numerical results for the tilted shock tube configuration also demonstrated good agreement. Upon acceleration by the shock wave the instability that formed was rotated from its original angle, although no additional measurable rotation was observed.

SHAMRC proved to be a useful tool in exploring these types of fluid instabilities. It provided insight into the experimental results and helped to better understand the phenomena that were observed. In particular, SHAMRC was very useful in exploring the effects of the composition of the initial conditions, varying the Atwood and Mach numbers, and particle sizes on instability formation and growth. In general, numerical tools can be extremely useful in interpreting experimental results and, when properly validated, can be used to explore wide ranging parameter spaces not readily accessible in experimental work.

References

[1] P. Vorobieff, M. Anderson, J. Conroy, R. White, and C. R. Truman. Vortex formation in a shock-accelerated gas induced by particle seeding. *Physical Review Letters*, 106:184503, 2011.

[2] R. D. Richtmyer. Taylor instability in shock acceleration of compressible fluids. *Communications in Pure and Applied Mathematics*, 13(13):297–319, 1960.

[3] E. E. Meshkov. Instability of the interface of two gases accelerated by a shock-wave. *Izv. AN SSSR, Mekh. Zhidk. Gaza*, 4(5):151–157, 1969.

[4] S. Ukai. Richtmyer-Meshkov instability with reshock and particle interactions. Masters Thesis, Georgia Institute of Technology, Atlanta, Georgia, August 2010.

[5] P. Vorobieff and S. Kumar. Experimental studies of Richtmyer-Meshkov instability. *Recent Research Developments in Fluid Dynamics*, 5:33–55, 2004.

[6] M. Brouillette. The Richtmyer-Meshkov instability. *Annual Review of Fluid Mechanics*, 34:445–468, 2002.

[7] S. Nakai and H. Takabe. Principles of inertial confinement fusion: Physics of implosion and the concept of inertial fusion energy. *Reports of Progress in Physics*, 59(9):1071–1131, 1996.

[8] L. A. Marschall. *The Supernova Story*. Plenum Press, New York, 1988.

[9] R. A. Chevalier, J. M. Blondin, and R. T. Emmering. Hydrodynamic instabilities in supernova remnants: Self-similar driver waves. *The Astrophysical Journal*, 392:118–130, November 1991.

[10] J. Kane, R. P. Drake, and B. A. Remington. An evaluation of the Richtmyer-Meshkov instability in supernova remnant formation. *The Astrophysical Journal*, 511:335–340, January 1999.

[11] D. Arnett. The role of mixing in astrophysics. *The Astrophysical Journal Supplement Series*, 127(2):213–217, April 2000.

[12] I. Glassman. *Combustion*. Academic Press, San Diego, 3rd edition, 1996.

[13] A. M. Khokhlov, E. S. Oran, and G. O. Thomas. Numerical simulation of deflagration-to-detonation transition: The role of shock-flame interactions in turbulent flames. *Combustion and Flame*, 117:323–339, 1999.

[14] J. Yang, T. Kubota, and E. E. Zukoski. Applications of shock-induced mixing to supersonic combustion. *AIAA Journal*, 31(5):854–862, May 1993.

[15] G. Rudinger and L. M. Somers. Behaviour of small regions of different gases carried in accelerated gas flows. *Journal of Fluid Mechanics*, 7(2):161–176, 1960.

[16] J. F. Haas and B. Sturtevant. Interaction of weak shock waves with cylindrical and spherical gas inhomogeneities. *Journal of Fluid Mechanics*, 181:41–76, 1987.

[17] J. M. Picone and J. P. Boris. Vorticity generation by shock propagation through bubbles in gas. *Journal of Fluid Mechanics*, 189:23–51, 1988.

[18] J. W. Jacobs. The dynamics of shock accelerated light and heavy gas cylinders. *Physics of Fluids A*, 5(9):2239–2247, 1993.

[19] P. M. Rightley, P. Vorobieff, and R. F. Benjamin. Evolution of a shock-accelerated thin fluid layer. *Physics of Fluids*, 9(6):1770–1782, 1997.

[20] J. W. Jacobs, D. G. Jenkins, D. L. Klein, and R. F. Benjamin. Nonlinear growth of the shock-accelerated instability of a thin fluid layer. *Journal of Fluid Mechanics*, 295:23–42, 1995.

[21] P. Vorobieff, P.M. Rightley, and R. F. Benjamin. Power-law spectra of incipient gas-curtain turbulence. *Physical Review Letters*, 81(11):2240–2243, September 1998.

[22] K. Prestridge, P. Vorobieff, P. M. Rightley, and R. F. Benjamin. Validation of an instability growth model using particle image velocimetry measurements. *Physical Review Letters*, 84:4353–4356, May 2000.

[23] C. A. Zoldi. *A Numerical and Experimental Study of a Shock-Accelerated Heavy Gas Cylinder*. Doctoral Dissertation, State University of New York at Stony Brook, May 2002.

[24] P. G. Saffman. On the stability of laminar flow in dusty gas. *Journal of Fluid Mechanics*, 13:120–128, 1961.

[25] J. Crepeau, S. Hikida, and C. E. Needham. Second Order Hydrodynamic Automatic Mesh Refinement Code (SHAMRC): Volume I, Methodology. Technical report, Applied Research Associates, Inc., May 2001.

[26] Leon A. Wittwer. A source code library manager, May 1995.

[27] J. Crepeau, H. Happ, S. Hikida, and C. E. Needham. Second Order Hydrodynamic Automatic Mesh Refinement Code (SHAMRC): Volume II, User's Manual. Technical report, Applied Research Associates, Inc., May 2001.

[28] Frank M. White. *Viscous Fluid Flow*. McGraw Hill, New York, third edition, 2006.

[29] R. T. Carter et. al. Estimating the drag coefficients of the meteorites for all mach number regimes. In *Proceedings of the 40th Lunar and Planetary Science Conference*. Lunar and Planetary Science Conference, 2009.

[30] ANSYS Inc. ANSYS FLUENT Theory Guide. http://www.ansys.com, November 2010.

[31] ANSYS Inc. ANSYS FLUENT Users Guide. http://www.ansys.com, November 2010.

[32] C. Tomkins, K. Prestridge, P. Rightley, P. Vorobieff, and R. Benjamin. An experimental investigation of mixing mechanisms in shock-accelerated flow. *Journal of Fluid Mechanics*, 611:131–150, 2008.

[33] J. D. Anderson Jr. *Modern Compressible Flow*. McGraw-Hill, New York, 2nd edition, 1990.

[34] G. C. Orlicz, B. J. Balakumar, C. D. Tomkins, and K. P. Prestridge. A mach number study of the Richtmyer-Meshkov instability in a varicose, heavy-gas curtain. *Physics of Fluids*, 21:064102, 2009.